

Department of Mechanical Engineering
Center for Building Materials

**Contact-Free Non-Destructive Inspection
by Broadband Ultrasound**

Janez Rus

Vollständiger Abdruck der von der Fakultät für Maschinenwesen der Technischen Universität
München zur Erlangung des akademischen Grades eines

Doktor-Ingenieurs (Dr.-Ing.)

genehmigten Dissertation.

Vorsitzender: Prof. Dr. ir. Daniel J. Rixen

Prüfer der Dissertation: 1. Prof. Dr.-Ing. habil. Christian U. Große
2. Prof. Dr. rer. nat. habil. Marc Kreutzbruck

Die Dissertation wurde am 05.01.2021 bei der Technischen Universität München eingereicht
und durch die Fakultät für Maschinenwesen am 24.02.2021 angenommen.

Acknowledgements

First of all, I would like to thank my supervisor Prof. Dr. Christian U. Grosse for suggesting me such an interesting, stimulating and industry-relevant topic, which is so prospective for new findings and innovations, and for granting me such a great deal of freedom regarding the direction and structure of my research. I very much appreciated all his feedbacks, opinions and advices. I am grateful that he recognized the potential of the absolutely extraordinary possibilities that were provided to me by the external, independent financing, which was free of any constraints concerning research topic and structure.

At this point I would like to write some words about Dr. Otto and Karla Likar who were in a certain way like parents to me by providing me the financial support for my PhD studies (extracted from the writing of Dr. Otto Likar personally).

Dr. Otto Likar was born on January 12, 1915. He graduated in civil engineering at University of Ljubljana in 1938. In the years between 1939 and 1942, during the war, he did his PhD studies at the Technical University of Munich under supervision of Prof. Günter Worch (“Baustatik und Stahlbau”). In the post-war conditions, he worked in the construction company Wayss u. Freytag until 1958, when he established his own office for statics in civil engineering. His office of 26 employees was involved in various construction projects mostly in the city of Munich: schools, hospitals, Max Planck Institute for Psychological Research, residential and industrial buildings, sport halls and administrative building for the Olympic Games and subway infrastructure of Munich. He revised the statics of more than 150 bridges for road traffic and was involved as an expert for their maintenance. In 2015, Dr. Otto Likar died in the age of 90 in the same year as his wife, Karla.

In 1993, they founded *Dr.-Ing. Otto and Karla Likar foundation*, which almost every year supports a small number of students of University of Ljubljana, who would like to continue their studies at the Technical University of Munich. I would like to thank to prof. Dr. Miha Boltežar, prof. Dr. Janko Slavič and other members of the committee, who, by choosing appropriate and qualified candidates, help the foundation serving its purpose expressed by the Likar spouses.

As it was a wish of Dr. Otto Likar, I would like to express my gratitude to “Regierung von Oberbayern” and Technical University of Munich to enable the establishment of the Foundation.

Further thanks go to my working colleagues, who were always open for a discussion on my research topic. Special thanks to Rudolph Kraus and Isabelle Stüwe for all their comments and suggestions, which improved my writing style.

I am grateful to the external partners for the enriching cooperation, which was motivated by our shared curiosity on the outcomes of our studies. Their expertise and material resources make my PhD project possible in the present scope. Special thanks to:

- Dr. Klaas Bente and Dr. Mate Gaal from German Federal Institute for Materials Research and Testing (“Bundesanstalt für Materialforschung und -prüfung”) for hosting me on a scientific visit, where the combined use of our experimental equipment deliver us some interesting results,
- Dr. Hubert Mooshofer (Siemens CT) for a shared supervision of a student work and for the experimental equipment,
- Dr. Balthasar Fischer (Xarion Laser Acoustics) for providing the experimental equipment and for a really fruitful scientific visit,
- Alex Gustschin (Chair of Biomedical Physics, Munich School of Bioengineering) for all his contributions linked with the radiography methods,
- Huang Ming (Imperial College London) for his scientific visit in our research group and his modelling related to my research topic.



Dr. Otto Likar, Dipl.-Ing., and Karla Likar Foundation

Information on the Presented PhD Thesis

The presented PhD thesis has the form of a publication-based promotion (cumulative thesis). In accordance with the § 6 Abs. 2 *Rechtliche Grundlagen Promotionsordnung der TUM*, it includes the following sections:

- introduction
- summary of each publication
- cross-thematic overview and discussion
- full-text publications in Appendix or bibliographic references if copyright

The following original research articles being objects of review processes have been published on the work of the presented PhD thesis up to the time of its final submission:

- **Article #1** Rus, J., Grosse, C. U. (2020). Local Ultrasonic Resonance Spectroscopy: A Demonstration on Plate Inspection. *Journal of Nondestructive Evaluation*, 39(31), doi: 10.1007/s10921-020-00674-5.
- **Article #2** Rus, J., Gustschin, A., Mooshofer, H., Grager, J.-C., Bente, K., Gaal, M., Pfeiffer, F., Grosse, C. U. (2020). Qualitative Comparison of Non-Destructive Methods for Inspection of Carbon Fiber-Reinforced Polymer Laminates. *Journal of Composite Materials*, 57(27), 4325-4337, doi: 10.1177/0021998320931162.
- **Article #3** Rus, J., Grosse, C. U. (2021). Thickness Measurement via Local Ultrasonic Resonance Spectroscopy. *Ultrasonics*, 109, 106261, doi: 10.1016/j.ultras.2020.106261.

The following original research articles were at the time of the final submission of the presented PhD thesis in the review process:

- Kulla, D., Huang, M., Rus, J., Grosse, C. U.. Numerical and Experimental Acoustic Field Characterization of Air-Coupled Ultrasound Transducers.
- Bente, K., Rus, J., Mooshofer, H., Gaal, M., Grosse, C.U.. Microsecond Pulses Enable Simultaneous Measurement of Thickness and Speed of Sound in Solids by Air-Coupled Ultrasound.

The outcomes of the research of the presented PhD thesis have also been presented in the form of the following conference contributions:

- Rus, J., Fischer, B., Grosse, C. U. (2019a). Photoacoustic Inspection of CFRP Using an Optical Microphone. *Proc. SPIE, Optical Measurement Systems for Industrial Inspection XI*, 1105622, doi: 10.1117/12.2525021.
- Rus, J., Kulla, D., Grager, J. C., Grosse, C. U. (2019b). Air-Coupled Ultrasonic Inspection of Fiber-Reinforced Plates Using an Optical Microphone. *Proc. of German Acoustical Society, DAGA Rostock*, 763-766.
- Rus, J., Fischer, B., Grosse, C. U. (2019). Experimental Comparison of the Emitter and Receiver Alternatives in Air-Coupled Ultrasonic testing of CFRP plates. *15th International Symposium on Nondestructive Characterization of Materials*.

The following two theses has been supervised in the framework of the presented PhD Thesis.

- Dzafic, S. (2020). Experimental Comparison of Air-Coupled Ultrasonic Testing Methods. *Master's thesis, Chair of Non-Destructive Testing, Technical University of Munich*.
- Kulla, D. (2019). Investigation of Focused Transducers for Air-Coupled Ultrasound Testing. *Bachelor's thesis, Chair of Non-Destructive Testing, Technical University of Munich*.

Abstract

There is a general unjustified perception that ultrasonic inspection methods are problematic to be stand-off and broadband at the same time, due to the technical limitations. However, research in this topic is particularly stimulating and interesting for industrial applications. Firstly, obtaining the information over a distance, without physical contact to the inspected object, has practical advantages linked with applicability and robustness. Certain specimens are incompatible with the couplant or the probe itself, which can, on the other hand, crucially influence the measured properties. Detachment of the probe and the specimen simplifies the kinematics of the scan process, which can thus easier be automated. Secondly, broadband inspection methods expand the information pool and additional parameters can be extracted at different frequency ranges of the spectrum obtained by a single experiment.

Research presented in this work was initiated by innovative ultrasound contact-free generation and detection techniques that have been designed to meet the conditions of high bandwidth: a laser pulse and a thermoacoustic emitter in the combination with an optical microphone.

After addressing the main challenges on this topic, we review existing contact-free generation and detection possibilities of broadband ultrasound and describe non-destructive testing methods utilizing broadband analysis of ultrasound. We suggest a presentation of broadband scan results in colors. From a single two-dimensional scan image, the information about the amplitude, equivalent monochromatic frequency, and the presence of other frequency components of the ultrasound can be discerned by colors and their shades.

Starting point of our research was formed by a broad experimental comparison of our innovative techniques to well-established inspection methods, which were all applied on the same specimen (a carbon fiber-reinforced polymer laminate with induced impact damage): air-coupled ultrasound testing (using piezoelectric transducers, broadband optical microphones, cellular polypropylene transducers, and a thermoacoustic emitter), laser-induced ultrasound testing, ultrasonic immersion testing, phased array ultrasonic testing, optically excited lock-in thermography, and X-ray radiography (projectional absorption and dark-field, tomosynthesis, and microcomputed tomography).

Subsequently, we introduced a new broadband approach to material inspection, termed local ultrasonic resonance spectroscopy (LURS), which is based on local mechanical impulse response analysis. The mechanical response, which is captured near the excitation point, depends predominantly on the local properties of the specimen, for short excitation pulses. Amplitude values and peak frequencies of local resonances, lying in the ultrasonic frequency range, contain information on the geometric, material and condition properties. The features of the specimen are visualized while performing a scan.

We described an application of LURS for inspection of carbon fiber-reinforced polymer plate, which included aluminum inclusions, delaminations and flat-bottom hole. Local resonances of delaminations and flat-bottom hole were detected in the frequency range up to 110 kHz, while the aluminum inclusions influenced the thickness resonance of the plate.

Furthermore, we demonstrated by the same setup, using laser-pulses and an optical microphone, that plate thickness and reliefs of both plate surfaces (plate curvature) can be obtained from thickness resonance and time of arrival analysis without the physical contact to the specimen.

Keywords:

- Non-destructive testing
- Broadband ultrasonic inspection
- Contact-free inspection
- Air-coupled ultrasound
- Photoacoustics
- Thermoacoustics
- Local ultrasonic resonance spectroscopy
- Local resonance
- Thickness resonance
- Carbon fiber-reinforced polymer

Table of Content

| | |
|--|-------------|
| Acknowledgements | II |
| Information on the Presented PhD Thesis | IV |
| Abstract | VI |
| Table of Content | VIII |
| Table of Figures | X |
| Table of Abbreviations | XII |
| 1 Introduction | 1 |
| 1.1 Advantages of Air-Coupled Ultrasound Methods | 1 |
| 1.2 Limitations of Air-Coupled Ultrasound Methods..... | 1 |
| 1.2.1 Transmittance of a Plate or a Gap | 4 |
| 1.3 Applications of Narrowband Air-Coupled Ultrasound for Plate Inspection | 7 |
| 1.4 Objectives | 7 |
| 2 Contact-Free Generation of Broadband Ultrasound | 9 |
| 2.1 Capacitive Transducer | 9 |
| 2.2 Thermoacoustic Emitter..... | 10 |
| 2.3 Plasma-Based Emitter..... | 11 |
| 2.4 Laser-Induced Ultrasound | 12 |
| 3 Contact-Free and Broadband Detection of Ultrasound | 13 |
| 3.1 Optical Microphone | 13 |
| 3.2 Laser Beam Probe..... | 16 |
| 4 Definition of S-scans | 17 |
| 5 Acoustic Spectroscopy in Non-Destructive Testing | 19 |
| 5.1 Local Defect Resonance | 19 |
| 5.2 Impact-Echo..... | 19 |
| 5.3 Local Acoustic Resonance Spectroscopy | 20 |
| 5.4 Local Ultrasonic Resonance Spectroscopy..... | 20 |
| 5.4.1 Laser Pulse and Eta450 Optical Microphone | 21 |
| 5.4.2 Thermoacoustic Emitter and Eta450 Optical Microphone..... | 24 |
| 5.4.3 Piezoelectric Transducers and Eta450 Optical Microphone | 26 |
| 6 Ultrasound in Colors | 28 |

| | | |
|-----------|--|-----------|
| 7 | Outline of Article #1 | 30 |
| 7.1 | Authors' Contributions for Article #1 | 30 |
| 8 | Outline of Article #2 | 31 |
| 8.1 | Authors' Contributions for Article #2 | 32 |
| 9 | Outline of Article #3 | 33 |
| 9.1 | Authors' Contributions for Article #3 | 34 |
| 10 | Cross-Thematic Discussion | 35 |
| 11 | References | 37 |
| | Appendix | 44 |
| | Article #1: Local Ultrasonic Resonance Spectroscopy: A Demonstration on Plate Inspection | 44 |
| | Article #2: Qualitative Comparison of Non-Destructive Methods for Inspection of Carbon Fiber-Reinforced Polymer Laminates | 57 |
| | Article #3: Thickness Measurement via Local Ultrasonic Resonance Spectroscopy | 71 |

Table of Figures

Figure 1.1: Ratio of the transmitted pressure amplitude for the CFRP plate with water and air as surrounding medium in dependence on the plate thickness and frequency of the transmitted US. The acoustic impedance of the surrounding medium influences the acoustic finesse and consequently the slope of the curve. Small change in the plate thickness influences the transmission ratio significantly if the testing frequency is close to the thickness resonance (TR) frequency of the plate. 6

Figure 2.1: Photo and scheme of a TAE. A short high-power electrical pulse is applied on a thin indium tin oxide film. A short US pulse is generated by the fast heating of air in the immediate vicinity of the film. Radial shape of a glass substrate induces a focusing effect. 10

Figure 2.2: Time signal (a) as captured by a LV illuminating a thin foil, which is set in the focus of a TAE, together with its amplitude spectrum (b). 11

Figure 3.1: Etalon of the optical microphone consists of two mirrors with coupling to a single-mode optical fiber. US, which crosses the Fabry-Perot etalon, is measured by the alteration of the refractive index of air, which is a function of the pressure development in time. 13

Figure 3.2: Time signal (a) as captured by an Eta450 optical microphone, which is set in the focus of a TAE, together with its amplitude spectrum (b). 15

Figure 4.1: Data matrix of the 2-dimensional scan in the time (a) and in the frequency (b) domain can be visualized by slicing it planes of different orientations. B-scan and S-scan (B-scan in frequency domain) are marked in blue. C-scans obtained from data matrix in time and frequency domains are marked in red. The signal amplitude shown in grayscale is symbolic. 17

Figure 5.1: B-scan of a CFRP plate including an impact damage of full length (a) and zoomed to the first part of the wave train (b) obtained by a laser pulse and an optical microphone. S-scans (B-scans in frequency domain) of low (c) and high (d) frequency range. The impact damage extends from 19 mm to 45 mm scanning position y . For details about the experimental setup, please refer to Article #2 (in Appendix). 22

Figure 5.2: C-scans of an impact damage at various frequencies obtained by a single broadband scan using a laser pulse and an optical microphone. In the frequency range up to 500 kHz, chaotically distributed LDRs cause variation of US amplitude (a-e) at the impact damage. High frequency components (800 kHz and above) are highly dissipated in the damaged area (f, g). For details about the experimental setup, please refer to Article #2 (in Appendix). 23

Figure 5.3: B-scan (a) and S-scan (B-scan in frequency domain) (b) of a CFRP plate including an impact damage obtained by a TAE and an optical microphone. The impact damage extends from 19 mm to 45 mm scanning position y . For details about the experimental setup, please refer to Article #2 (in Appendix). 24

Figure 5.4: C-scans of an impact damage at various frequencies obtained by a single broadband scan using a TAE and an optical microphone. Chaotically distributed LDRs cause variation of US amplitude at the location of the impact damage. For details about the experimental setup, please refer to Article #2 (in Appendix)..... 25

Figure 5.5: C-scans of an impact damage as obtained by an optical microphone and narrowband piezoelectric transducers of 200 kHz (a) and 400 kHz (b) nominal frequency used as US sources. The specimen is the same as in the previous figures of this section. For additional details, please refer to (Dzafic 2020)..... 26

Figure 6.1: Scan results obtained by the broadband US shown in colors. At the impact damage only low-frequency (red) US components are detected, while the damage-free plate area transmits broadband (white) US and variation of intensity reveals the fiber orientation of the layer close to the detector (a). The aluminum inclusions cause slightly visible shift to purple frequency components at scanning positions x below 8 mm, while the tree delaminations are visible in red color (b). Flat-bottom hole transmits more of the US, which is visible as bright yellow circle (b). For details about the experimental setup, please refer to Article #1 and Article #2 (both in Appendix)..... 29

Figure 10.1: Schematic presentation of the inspection methods addressed by the articles, which constitute the presented work. Articles #1 (in Appendix) and Article #3 demonstrate the application of LURS for inspection of material (inclusions, damages) and geometrical properties (plate relief and thickness) of the specimen, while Article #2 (in Appendix) forms a thematic basement made by a broad experimental comparison of CFRP inspection methods. 35

Table of Abbreviations

| | |
|------|---|
| ACU | air-coupled ultrasound |
| CFRP | carbon fiber-reinforced polymer |
| LARS | local acoustic resonance spectroscopy |
| LDR | local defect resonance |
| LR | local resonance |
| LURS | local ultrasonic resonance spectroscopy |
| LV | laser vibrometer |
| NDT | non-destructive testing |
| SNR | signal-to-noise ratio |
| TAE | thermoacoustic emitter |
| TR | thickness resonance |
| US | ultrasonic/ultrasound |

1 Introduction

Fundamental objective of non-destructive testing (NDT) methods is to access the information about the specimen, while preserving its initial properties (Grosse 2013). Since the key challenge is to access the internal properties of the specimen, the information needs to be spatially transferred between the inspected location and the probe device. Performance of inspection methods is conditioned by information transmission efficiency in a given medium.

A broad majority of conventional US (ultrasonic/ultrasound) methods for internal inspection of solid specimens presuppose physical contact of the probe device to the specimen and/or a liquid couplant in order to achieve the acoustic impedance matching over the US transmission path. However, there are certain methods, which expand this categorization and have already found their industrial applications. So called air-coupled ultrasound (ACU) testing methods use air as a coupling medium. Their explicit advantages stimulate the intensive ongoing development, which is however constrained by some physical limitations.

Typically, a specimen is placed between an US transmitter and an US receiver. The features of the specimen are characterized by observing the obtained the signal when the US is transmitted through the specimen (through-transmission setup).

1.1 Advantages of Air-Coupled Ultrasound Methods

Absence of a liquid couplant has a clear advantage of simplification of an inspection process. This is especially relevant for the repetitive industrial applications that have to be fast, robust, and easy to apply. ACU methods have a potential for optimization of operational costs and resources. Due to the gap between the specimen and the US transducers, they are kinematically less complicated to be automated.

While using air as a coupling medium, repeatability of the inspection can be improved. We do not have problems with variation of coupling properties, which can be the case for contact US methods, caused by the shortage of a liquid couplant or by the deficient contact of the probe with the specimen surface.

ACU methods extend the possibilities for the inspection of fragile, corrosive, hot, and other materials that should be avoided to be in contact with liquid couplants e.g. foams, certain ceramics, uncured plastics, or metals during heat treatment.

1.2 Limitations of Air-Coupled Ultrasound Methods

The fundamental limitation of ACU testing methods is explained by the theory of plane sound waves at perpendicular incidence on a plane boundary (Krautkrämer and Krautkrämer 1990).

Ratios of the reflected p_R and the transmitted wave pressure amplitude p_T to the incident wave pressure amplitude p_E can be expressed as:

$$\frac{p_R}{p_E} = \frac{Z_2 - Z_1}{Z_2 + Z_1} \quad \frac{p_T}{p_E} = \frac{2Z_2}{Z_2 + Z_1}, \quad 1.1$$

where Z_1 is acoustic impedance (material density multiplied by the sound velocity in the material) of the material on the incident and reflection side and Z_2 acoustic impedance of the material on the transmission side. In agreement with the conservation of momentum the following relation is true for Equation 1.1:

$$p_E + p_R = p_T. \quad 1.2$$

From Equation 1.1 it follows that the amplitude of the reflected wave can have a reversed sign to the amplitude of the incident wave. This signifies the phase shift for the reflection at the boundary from a material with higher to a material with lower acoustic impedance (Z_2 lower than Z_1). At the transmission from the material with lower to material with higher acoustic impedance (Z_2 higher than Z_1), we have an increase of the pressure amplitude of the transmitted wave in relation to the incident wave. However, this does not break the energy conservation law since the sound intensity (power per unit area) is proportional to the square of the pressure amplitude and inversely proportional to the acoustic impedance of the media, in which it propagates:

$$I = \frac{p^2}{2Z}. \quad 1.3$$

By Equation 1.3, Equations 1.1 can be transformed to the ratios of the reflected I_R and transmitted intensity I_T to the incident intensity I_E :

$$\frac{I_R}{I_E} = \frac{(Z_2 - Z_1)^2}{(Z_2 + Z_1)^2} \quad \frac{I_T}{I_E} = \frac{4Z_1Z_2}{(Z_2 + Z_1)^2}. \quad 1.4$$

Equations 1.4 illustrate the energy conservation law

$$I_E = I_T + I_R \quad 1.5$$

more explicitly.

Air has 4 to 5 orders of magnitude lower acoustic impedance (approximately 410 kg/m²s at room temperature) than water (approximately 1.5×10⁶ kg/m²s) and solids (approximately 45·10⁶ kg/m²s for steel). Acoustic impedance of carbon fiber reinforced polymers depends on the texture fiber orientation and the material properties of the fibers and matrix. Typical value for the carbon fiber-reinforced polymer (CFRP) used in this study is 4.4·10⁶ kg/m²s perpendicularly to the fiber orientation.

In the Table 1 the transmission and reflection ratios for air-to-CFRP and CFRP-to-air transition are labeled. They are calculated from the equations for pressure amplitude (Equations 1.1) and the equations for sound intensity (Equations 1.4).

Table 1: Transmission and reflection ratios of pressure amplitude and sound intensities for air-to-CFRP and CFRP-to-air transition of sound waves.

| | Air-to-CFRP transition | CFRP-to-air transition |
|---|-------------------------------|-------------------------------|
| Reflection ratio of pressure amplitude | 0.9998 (-0.0016 dB) | -0.9998 (-0.0016 dB)* |
| Transmission ratio of pressure amplitude | 1.9998 (6 dB) | $1.87 \cdot 10^{-4}$ (-75 dB) |
| Total Air-CFRP-Air transmission ratio of pressure amplitude | $3.7 \cdot 10^{-4}$ (-69 dB) | |
| Reflection ratio of sound intensities | 0.9996 (-0.0033 dB) | 0.9996 (-0.0033 dB) |
| Transmission ratio of sound intensities | $3.7 \cdot 10^{-4}$ (-69 dB) | $3.7 \cdot 10^{-4}$ (-69 dB) |
| Total Air-CFRP-Air transmission ratio of sound intensities | $1.4 \cdot 10^{-7}$ (-137 dB) | |

*Absolute value used for dB unit.

At each solid-to-air interface great majority of US is reflected. The pressure amplitude of the reflected sound waves is just for factor $2 \cdot 10^{-4}$ smaller from the pressure amplitude of the incident sound waves for the air-to-CFRP interface. Due to the higher acoustic impedance of CFRP, the pressure amplitude is higher inside of CFRP for air-to-CFRP transmission (6 dB increase). After transmission of sound back to air, the amplitude is reduced by 75 dB, what results in total transmission (neglecting the in-plate reflections) ratio of -69 dB.

Transmission ratio of sound intensities is for both transitions the same. By their multiplication, the total air-CFRP-air transmission ratio of sound intensities amounts to -137 dB. That is the square value of total air-CFRP-air transmission ratio of pressure amplitude.

Since steel has acoustic impedance approximately ten times higher than typical values for CFRP, the total air-steel-air transmission ratio of pressure amplitude is -89 dB (-177 dB for intensity). Steel is more rigorous material for ACU inspection.

If water is used as a coupling medium instead of air, the level of transmitted sound is increased significantly. Sound pressure amplitude at water-CFRP-water transmission is reduced only by 2.4 dB (4.8 dB for intensity). 75% of the incident amplitude is transmitted (58% of intensity). This is 2000 times more than for the sound pressure amplitude at air-CFRP-air interface ($4 \cdot 10^6$ times more of sound intensity). This is why conventional US inspection methods are so closely related to coupling techniques based on liquids.

Physics of acoustic waves constrains the abilities of ACU testing methods. It is extremely hard to access the information-carrying US waves. In order to overcome the high losses at air-

to-solid and solid-to-air transition, the intensity of the emitted US is increased to the technical limits of the ACU transmitter. At the same time we need to use sensitive sensors with low self-noise.

For the power increase of emitted US, other characteristics of ACU transducers are sacrificed. Most of the ACU transducers are designed highly resonant. They are narrowband. Bandwidths of more than 10% of the nominal resonance frequency are rather exceptional. This is due to the undamped piezoelectric ceramic (or composite), which is the most common material used, and layer with specific matching acoustic impedance, which improve transmission efficiency from the piezoelectric material to air. Furthermore, ACU transducers have lower characteristic testing frequencies (typically from 50 kHz to 500 kHz) than contact and liquid-coupled transducers (typically several MHz for similar applications). This causes a significant increase in resolution and detection sensitivity. It is hardly possible to characterize the inspected features in axial testing direction. Conventional ACU methods are limited to detection of larger features (above mm range). Finally, power increase is achieved by increasing the aperture of the ACU transducers. Although focusing configuration can decrease the diameter of the soundfield to several mm on the specimen surface, spatial resolution of ACU methods often remains worse than by methods using liquid couplants.

However, increase in the power of the emitted US and detector's sensitivity, is not sufficient for effective ACU inspection, since detection of the US reflected from the specimen surface or with a direct path through air is increased at the same time. It is necessary to discern the US, which transmits the solid specimen, since it alone carries the information about the inspected region in the interior of the solid specimen.

Typically, ACU testing is limited to the inspection of plate-like specimens in through-transmission setup. The specimen is thus at the same time a shelter to prevent disturbing of the information-carrying US by the US transmitted through air, which has up to 2700 times (69 dB) higher amplitude. However, there has been some research of single-side configurations using pitch-catch technique (Delrue et al. 2010) and guided waves (Solodov et al. 2010). The inspection can be altered by the surface damage located on the side close to the US emitter and receiver, while it is challenging to access the information about the features located deeper in the specimen or on the opposite side of the plate (Dzafic 2020).

1.2.1 Transmittance of a Plate or a Gap

The theoretical approach above considers single material interface or two independent material interfaces. Mechanics of two interfaces that lay close to each other (e.g. in the case of a plate or a gap) differs due to the superposition of internal reflections between the two interfaces that interfere and influence the total transmission and reflection ratio (Krautkrämer and Krautkrämer 1990). For the case of narrowband long-length US of frequency f and plate (similarly for gap) of thickness d , the ratio of the transmitted amplitude to the incident amplitude can be expressed as

$$\frac{p_T}{p_E} = \frac{1}{\sqrt{1 + \frac{1}{4} \left(\frac{Z_M}{Z_P} - \frac{Z_P}{Z_M} \right)^2 \sin^2 \left(\frac{2\pi d}{\lambda} \right)}}, \quad 1.6$$

where Z_P is acoustic impedance of plate (gap), Z_M the acoustic impedance of surrounding medium on both sides of the plate and λ wavelength of pressure waves in the plate (gap). We assume parallel material boundaries, perpendicular incidence of the wave train and neglect the losses in the surrounding medium, in the plate and at the material boundaries.

Since the acoustic impedance of the acoustic medium on both sides of the plate is the same, the ratio of the transmitted intensity to the incident intensity is a square value of pressure ratio (Equation 1.6):

$$\frac{I_T}{I_E} = \frac{1}{1 + \frac{1}{4} \left(\frac{Z_M}{Z_P} - \frac{Z_P}{Z_M} \right)^2 \sin^2 \left(\frac{2\pi d}{\lambda} \right)}. \quad 1.7$$

Equation 1.7 has a form of an Airy function, which is also used in connection with optical Fabry-Perot interferometers (Meschede 2017). We can extract the finesse coefficient

$$F = \frac{1}{4} \left(\frac{Z_M}{Z_P} - \frac{Z_P}{Z_M} \right)^2, \quad 1.8$$

which is dependent on the acoustic impedances of the plate and on the acoustic impedances of the surrounding medium. Equation 1.7 can be written in a form:

$$\frac{I_T}{I_E} = \frac{1}{1 + F \sin^2 \left(\frac{2\pi d}{\lambda} \right)}. \quad 1.9$$

While in optics finesse coefficient depends on the optical reflectivity, the finesse coefficient in Equation 1.9 depends on the reflectivity of the acoustic waves on both interfaces. For the equivalent for finesse coefficient in acoustics, optical length is exchanged by the plate thickness d , and wavelength of the interfering light by the wavelength of the US at corresponding frequency.

The acoustic finesse illustrates a further challenge of air-coupled plate inspection by narrowband US. In Figure 1.1 we show ratio of the transmitted pressure amplitude for the CFRP plate with water and air as surrounding medium. It is expressed in dependence on the factor between the plate thickness and frequency of the transmitted US. Thereby we use Equation 1.6 where wavelength is expressed by the US frequency and US velocity in the CFRP material (perpendicularly to the fiber orientation).

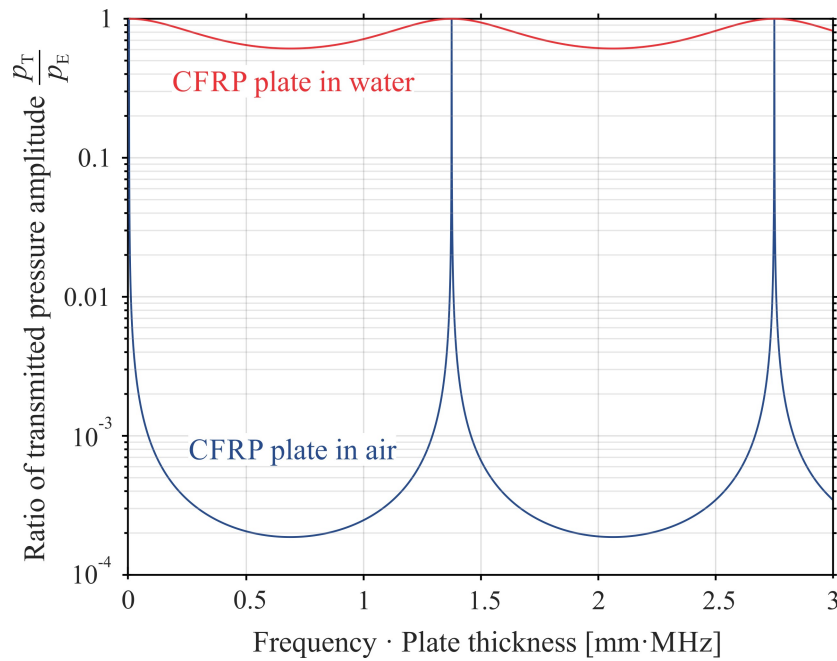


Figure 1.1: Ratio of the transmitted pressure amplitude for the CFRP plate with water and air as surrounding medium in dependence on the plate thickness and frequency of the transmitted US. The acoustic impedance of the surrounding medium influences the acoustic finesse and consequently the slope of the curve. Small change in the plate thickness influences the transmission ratio significantly if the testing frequency is close to the thickness resonance (TR) frequency of the plate.

If the acoustic impedance of the inspected plate differs greatly from the acoustic impedance of the surrounding medium, the finesse coefficient has a high value. It influences the slope of the curve in Figure 1.1, which is extremely high around the abscissa value, which meets the condition of wavelength matching the double thickness of the plate. At this characteristic frequency, the transmission ratio is in the theory equal to one. If the plate is excited by the broadband US, this frequency is typically pronounced if the in-plate reflections can be well detected (as experimentally demonstrated in Section 5.4). This frequency we designate as thickness resonance (TR) frequency.

Around TR frequency even a small variation in the plate thickness cause a pronounced change in transmittance, during narrowband ACU inspection of plates. This change can lead to the misinterpretation of the results and can disturb the characterization of the inspected feature. This disadvantage can be well avoided if broadband US transducers are used instead, as we demonstrated in Article #2 (in Appendix).

Another limitation of the ACU methods is connected with the high dissipation of high-frequency US components in air (Bass et al. 1990). This problem can be solved similarly as the problem with low transmission levels at air-to-solid intersections. First possibility is to modulate to lower frequencies, however, for the cost of inspection sensitivity and resolution. Another possibility is to increase the US emission power (Section 2) or US sensor sensitivity (Section 3).

1.3 Applications of Narrowband Air-Coupled Ultrasound for Plate Inspection

Piezoelectric narrowband transducers and receivers have currently a prominent role in the industrial ACU inspection (Blomme et al. 2002; Rus et al. 2019b). They are the most often applied on large specimens (often plates), where large-scale features are inspected – usually delaminations, lateral cracks, impact damages and other mechanical defects that significantly influence the propagation of the US in the specimen.

ACU inspection is of high interest for the sectors such as aeronautic, automotive, and other lightweight industries which necessitate high security standards, for condition monitoring during production and lifetime of the product. On the other hand the ACU inspection can be used also for in-situ process control in energy, material processing, production, and other quality control applications.

Often inspected materials are CFRP (Grager et al. 2018; Grosse 2016; Sause et al. 2016), glass fiber reinforced polymers, foams, wood, and also metal sheets.

1.4 Objectives

In this work we limit on broadband *and* contact-free inspection methods. This is a strong constrain due to the physical nature of the problem. As described in Section 1.2, without physical contact to the specimen or without liquid couplant, it is extremely challenging to reach sufficient intensity of the US in the solid specimen – even more in broadband frequency range. It is hard to distinguish the signal from the noise if it is distributed over the broad frequency range.

Energy of a US pulse is defined by its length and amplitude. Due to the reasons provided in Section 1.2, the contact-free US inspection demand high energy pulse, which can be achieved only by increasing the pulse amplitude, if we want to remain broadband. This has technical limitations.

However, benefits of broadband US stimulate extensive research in this field. There are several possibilities that allow generation of broadband (i.e. short-enough) US pulse of sufficient energy (Section 2). On the receiver size there are some contact-free sensors existing that are sensitive in broadband frequency range (Section 3).

We evaluate feasibility of these US sources and receivers for NDT applications. Experimentally we focus on laser pulse and thermoacoustic emitter (TAE) as broadband US sources and broadband optical microphone as US sensor.

Since laser pulse generates US on the specimen surface in our applications, the broader term “contact-free” is more suitable than “ACU” to designate the inspection methods we address.

Objective of the presented work is to demonstrate the advantages of contact-free non-destructive inspection by broadband US and to evaluate its limitations. The starting point of

the methodical approach is a review of possibilities for broadband and contact-free generation and detection of US (Section 2 and 3). Performance of the considered innovative inspection alternatives is compared with a broad range of state-of-the-art methods in Article #2 (in Appendix).

From this broad thematic foundation we develop more specialized study of broadband local mechanical behavior of the specimen. We describe a new approach to inspection of local features by observing the natural mechanical response of the localized region of the solid specimen in US frequency range. An experimental demonstration was possible due to the measurement setup, which allowed effective broadband generation and detection of US. From local resonances (LR) or local defect resonances (LDR), if the feature is categorized as defect, the local mechanical properties of the specimen and the features (defects) can be characterized. We designate this approach as local ultrasonic resonance spectroscopy (LURS) and report about it in Article #1 (in Appendix) and Article #3.

From our results, it is possible to anticipate the direction of future development in contact-free US inspection. The provided conclusions are advantageous for a decision about a suitable solution for a specific industrial inspection task with requirements exceeding the capabilities of conventional methods.

By broadband US, another dimension is open, which allow more detailed characterization of the inspected features by extracting information-carrying parameters from the captured signal.

2 Contact-Free Generation of Broadband Ultrasound

Generation of high-energy broadband US pulses is technically challenging. The goal is to emit short pulses with highest-possible pressure peak amplitude. Especially the sufficient amplitude level is a condition for effective contact-free US inspection due to the problems connected with the low transmission levels at air-to-solid interfaces and US dissipation in air.

Piezoelectric transducers are frequently used as a US source for contact inspection methods and methods, which use liquid couplants. However they are not suitable as a broadband and air-coupled source. The fundamental reason for this is that the active piezoelectric material (ceramic, composite), which generates the US, is solid. Acoustic impedance leap between the air and the piezoelectric material is high, what cause inefficient transmission of US to air, what can be for narrowband US partly improved by a matching layer. Typically, large bandwidth and high emission power are excluding parameters, which depend on the geometry of the piezoelectric material and damping unit.

Cellular polypropylene transducers have an advantage of lower acoustic impedance of the active material, which increase the efficiency of US generation in air (Gaal et al. 2014; Gaal et al. 2016a; Gaal et al. 2019a; Gaal et al. 2013; Vössing et al. 2018). They have a tendency of being more broadband than piezoelectric transducers (e.g. 20% of the characteristic frequency), but, however, still cannot be classified as broadband. For further information about their inspection performance, please refer to Article #2 (in Appendix).

2.1 Capacitive Transducer

Capacitive (or capacitance) transducers are persuasive alternative to piezoelectric transducers to generate broadband frequency US in air (Gan et al. 2001; Kupnik et al. 2011). They are composed of a thin membrane and a fixed backplate with an undulating shape, what forms air or vacuum gaps in between (Ladabaum et al. 1998; Na et al. 2016). This forms a capacitor, which vibrates and emits US, as voltage is applied. The inverse effect can be used for US detection. Capacitive micromachined US transducers have special potential for practical applications due to their cost-efficient fabrication on silicon substrate (Haller and Khuri-Yakub 1994). Multi-element array configuration is often used for contact US transducers, while this configuration causes crosstalk issues for current ACU applications (Na et al. 2017). Capacitive transducers are efficient for sound generation and detection in air, since the impedance mismatching effect of transducer's active material to air is avoided. There are certain applications of capacitive transducers, which are broadband enough to detect TR of a plate in through-transmission setup (Schindel and Hutchins 1995; Wright and Hutchins 1999).

2.2 Thermoacoustic Emitter

Thermoacoustic Emitter (TAE) generates US directly in air by a short increase of its internal energy through heat (Lange and John 1915; Wentz 1922). It is thus a well suitable alternative for broadband generation of US in air. TAE consists of spherical glass substrate with a thin indium tin oxide film (e.g. 200 nm) (Daschewski et al. 2013). The cathode is connected to the film at the center of the glass substrate and anode at its outermost edge as shown in Figure 2.1. During the excitation a short high-power electrical pulse (e.g. 18 kW peak power) is sent through the film. Fast expansion of air in immediate vicinity of the film causes a short pressure wave, which propagates in a form of a focused soundfield. Induced US pulses have a typical length of several μs .

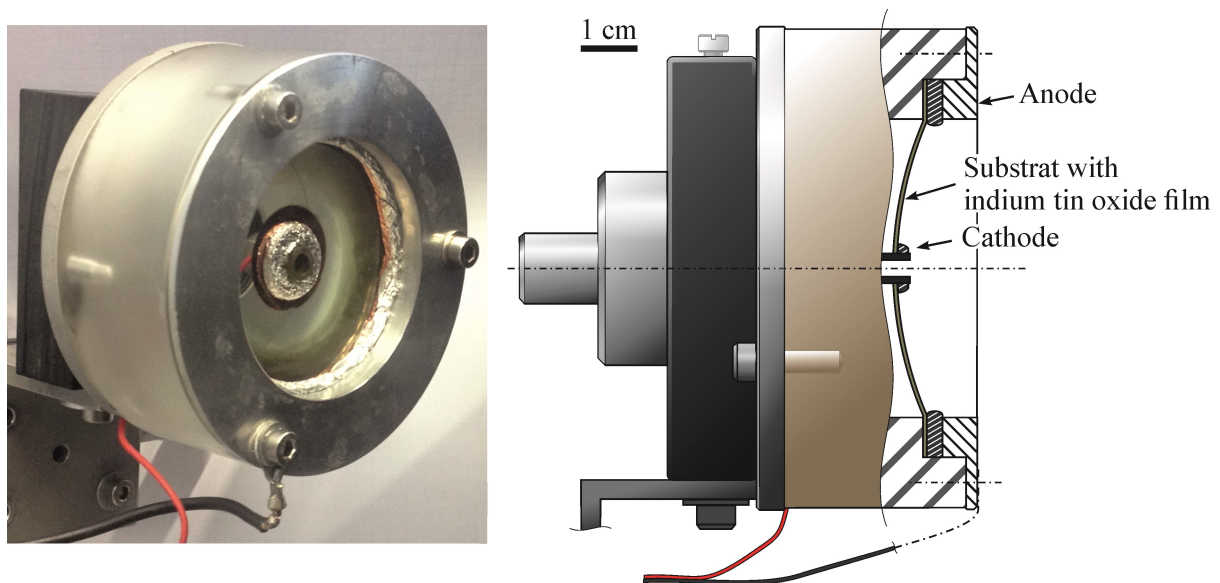


Figure 2.1: Photo and scheme of a TAE. A short high-power electrical pulse is applied on a thin indium tin oxide film. A short US pulse is generated by the fast heating of air in the immediate vicinity of the film. Radial shape of a glass substrate induces a focusing effect.

It is technically challenging to characterize the US pulse emitted by the TAE. There are no appropriate sensors with known frequency characteristics that would be able to capture the US in air in the required frequency range. An approximation to the pressure history of the pulse can be measured by a laser vibrometer (LV) illuminating a thin foil, which is placed in the focus of the TAE. However, the obtained signal is still influenced by the mechanics of the foil and the LV's measurement error. In Figure 2.2 we show a signal obtained by this setup, averaged 256 times. A TAE with 30.7Ω internal resistance and was excited by 600 ns pulse with the peak amplitude of 501 V. Transmitter and receiver were positioned in the way that the amplitude of the obtained signal was maximized.

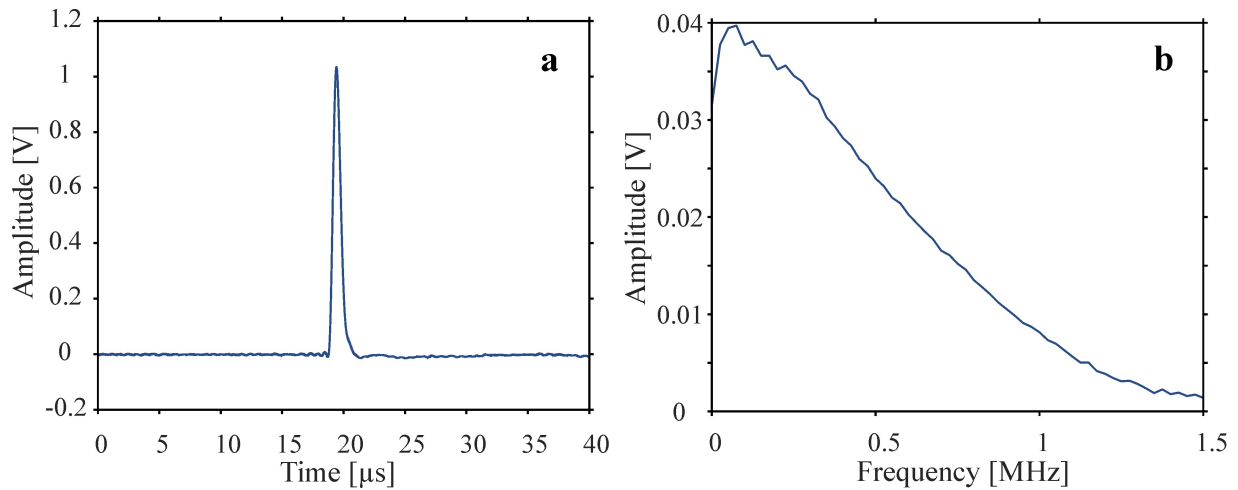


Figure 2.2: Time signal (a) as captured by a LV illuminating a thin foil, which is set in the focus of a TAE, together with its amplitude spectrum (b).

Pulse duration (full width at half-maximum) is 800 ns, what is more than the pulse length of the excitation voltage. However, there is no stronger ringing present after the first pulse. The amplitudes of the frequency components are well distributed. They fall below the half of the peak amplitude (-6 dB) value for the frequencies above 600 kHz.

The main challenge of US generation with TAE is connected with maximizing the peak pressure value. It was high enough to be detected by an Eta450 optical microphone (Section 3.1) after transmission through a CFRP plate. More about application of the TAE in combination with the Eta450 optical microphone for inspection of impact damage can be read in Article #2 (in Appendix). TAE and a cellular polypropylene receiver have also been implemented for CFRP inspection (Gaal et al. 2016b). The possibilities for single-side inspection using LV (directed on the specimen surface) are described as well.

2.3 Plasma-Based Emitter

Plasma-based emitters are in their working principle similar to the TAE, which are adapted that they can resist increased peak of the excitation voltage that does not only heat up the resistor and consequently an air layer, but also cause plasma discharge in air. The resulting acoustic wave is thus consequence of mainly thermoacoustic effect and a consequence of movements of ions (Gaal et al. 2019b; Kotschate et al. 2018). They are currently in an early stage of development and face some problems with the controllability of the discharge events.

Improved repeatability and higher intensities of the emitted US has been reported for laser-induced sparks in place of electronic spark source (Qin and Attenborough 2004). A short laser pulse (ns range) of high peak power is focused to a small spot. Increasing the energy of the pulse, the short-lasting plasma state of air is reached. Fast thermal extension and ionization of air gases forms a shock wave.

2.4 Laser-Induced Ultrasound

While laser breakdown in air (Section 2.3) have not been often applied for inspection purposes, a laser beam is a frequently used source of US, when being directed to the specimen surface (Diot et al. 2013; Park et al. 2014; Podymova and Karabutov 2014; Rus et al. 2019a; Sun and Zhou 2014; Wright et al. 1996). Laser beam is far most effective way of broadband, contact-free generation of US. First reason for this is that it is by laser technology possible to generate comparatively short pulses of high peak power. Secondly, it is possible to generate US directly in the specimen without the physical contact. Two solid-to-air interfaces are thus omitted (transmitter-to-air and air-to-specimen).

Thermoelastic and ablative regimes of laser-based US generation are practically applicable for US inspection (Bell 1881; Davies et al. 1993; Dewhurst et al. 1982; Hutchins 1986; Scruby and Drain 1990). For lower intensities, thin layer of the specimen surface illuminated by the laser beam is heated. The US wave is generated due to the fast thermal expansion and contraction. For the laser pulse intensities above the ablation threshold, a layer of the surface material is ablated. According to the law of conservation of momentum, the force pulse acts in the direction to the specimen if the matter (often in a form of plasma) is driven away from the surface. This regime, which generates US waves of higher intensity than thermoelastic regime, generally still counts as non-destructive US source if the quantity of the ablated material can be neglected. The third regime, in which US is generated by the momentum of light, is too weak for practical macro-scale industrial applications (Požar et al. 2018).

Material inspection by laser-induced US have been performed in combination with LV in through-transmission (Diot et al. 2013) and single side configuration (Park et al. 2014; Sun and Zhou 2014). Typically they observed influence of the inspected feature on the propagation of the US waves.

Laser induced US have been used also in the combination with air-coupled transducer (Rus et al. 2019a; Wright et al. 1996). Signals, on which the in-plate reflections are visible, were processed in time and/or frequency domain in order to obtain C-scans to visualize internal damage. Laser induced US in combination with a liquid-coupled piezoelectric sensor was used to characterize porosity in the samples (Podymova and Karabutov 2014).

3 Contact-Free and Broadband Detection of Ultrasound

Due to the same reasons, why piezoelectric transducers are less suitable for broadband ACU generation (Section 2), they are also less appropriate for broadband ACU detection. Cellular polypropylene transducers are not much better. On the other hand, capacitance transducer can be used also as US detectors with significantly broader frequency characteristics (Section 2.1).

3.1 Optical Microphone

In contrary to conventional microphones based on membrane or piezoelectric material, optical microphone does not have any moving parts (Fischer 2016; Preisser et al. 2016). They measure US directly in air, when it propagates through a miniature Fabry-Perot etalon. Consequently they exhibit the following advantages that make them especially suitable for broadband ACU detection. Firstly, the solid-to-air interface is avoided, what improves the efficiency of sound detection in air. Secondly, they have less expressed natural resonance frequency behavior and they are sensitive to comparatively broader frequency range. Finally, the small size of the etalon is advantageous for improving the spatial resolution, while performing an inspection. Optical microphones has been developed and commercialized by the company Xarion Laser Acoustics, Vienna.

Etalon of the optical microphone can be described as consisting of two semi-transparent mirrors (Figure 3.1).

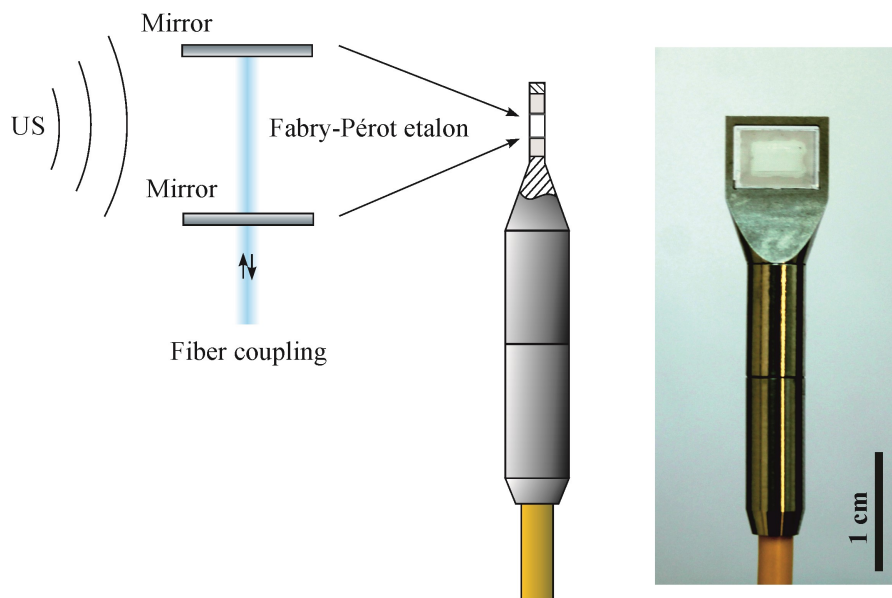


Figure 3.1: Etalon of the optical microphone consists of two mirrors with coupling to a single-mode optical fiber. US, which crosses the Fabry-Perot etalon, is measured by the alteration of the refractive index of air, which is a function of the pressure development in time.

The laser light of $1.55 \mu\text{m}$ wavelength transmitted through an optical fiber enters the etalon. The intensity of the reflected light back to the same optical fiber and the transmitted light is

for the ideal Fabry-Perot resonator defined by the Airy function, corresponding Equation 1.9. In both cases we consider wave phenomena on two parallel reflective surfaces: mechanic wave in the plate or electromagnetic wave in the optical etalon. Finesse coefficient is in the case of an optical etalon defined as

$$F = \frac{4R}{(1-R)^2}, \quad 3.1$$

where R is the mirror reflectivity (Fischer 2016; Meschede 2017; Preisser et al. 2016). Acoustic wavelength is exchanged with optical wavelength in Equation 1.9 and plate thickness with the optical length, defined as the product between the physical length between the two mirrors and the refractive index of the medium between them – air. Since refractive index depends on the pressure level, the US passing the etalon influences the intensity of the laser light, coupled back to the same single-mode optical fiber. The sensitivity of the optical microphone can be optimized by tuning the peak laser wavelength to the high-gradient regions of the Airy function. Sensitivity of the optical microphone is increased for higher finesse levels.

Optical microphone has not been properly calibrated for the whole frequency range in air due to the lack of the appropriate reference sensor that would be broadband enough. Alternatively the optical microphone could be potentially calibrated by a broadband US source that can be theoretically described (e.g. laser-induced breakdown in air).

Approximate impression about the bandwidth of the optical microphone can be obtained by comparing the obtained signal with the signal obtained by LV, which is directed on a thin foil to allow detection of US in air. For this experiment we used a TAE, which have a significantly better broadband characteristic than other ACU sources. After the experiment with the LV and the thin foil described in Section 2.2, we exchanged the US receiver by placing the optical microphone Eta450 in the focus of the same TAE. The position and orientation of the optical microphone were adjusted in order to receive maximal amplitude values. The obtained signal (Figure 3.2) can be compared with the signal of the measurement with the LV and the thin foil in Figure 2.2.

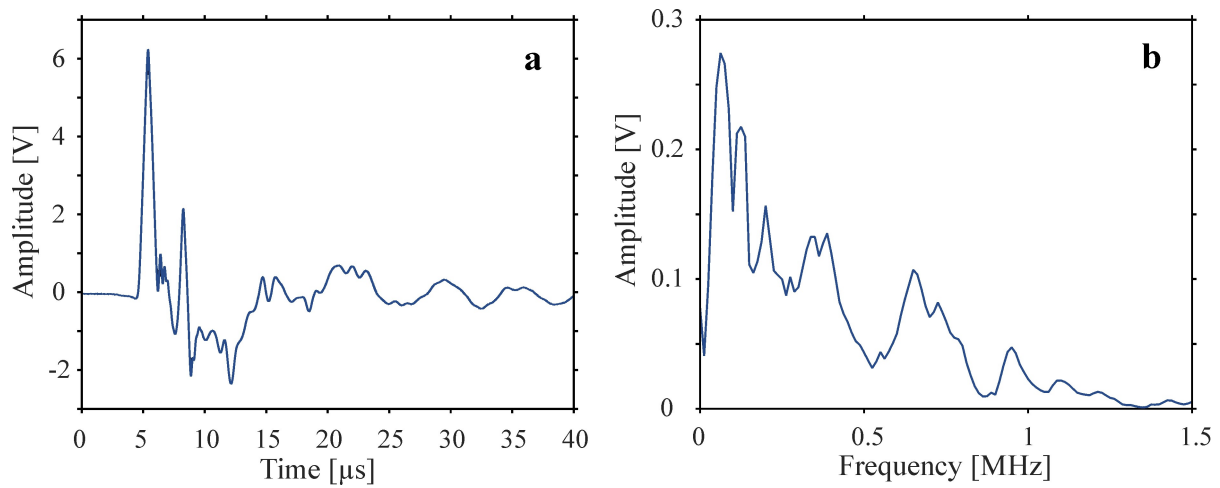


Figure 3.2: Time signal (a) as captured by an Eta450 optical microphone, which is set in the focus of a TAE, together with its amplitude spectrum (b).

Strong ringing appears in the signal if the receiver consisting of LV and thin foil is exchanged by the optical microphone. One explanation is that these strong oscillations after the first break of the signal are a consequence of the US source (TAE) and somehow cannot be detected by the LV and the thin foil. Second explanation is that they are linked with the US receiver (Eta450 optical microphone). The geometry of the etalon of the optical microphone can have certain influence on the captured signal. The reflections inside of the etalon can alter the signal since the focused US soundfield of the TAE is not homogenous and has multidirectional propagation properties. Furthermore, there is a long-lasting oscillation present with the period of 6.7 μ s (150 kHz). This peak is less pronounced in the amplitude spectrum (Figure 3.2 (b)) due to the other frequency components, which are more strongly attenuated but have higher amplitude directly after the first break of the signal. The amplitude spectrum is less monotonous for the signal obtained by the optical microphone (Figure 3.2b) than if the US, emitted by the same source, is measured by a LV and a thin foil (Figure 2.2b).

The maximum peak amplitude is higher when using Eta450 optical microphone in both, frequency and time domain. Since signal-to-noise ratio (SNR) is lower for the signal obtained by the optical microphone, it is advantageous for plate inspection in combination with TAE, in comparison with LV, which is directed on the thin foil in air and not on the specimen directly.

Optical microphone has already been used for some NDT applications. Laser pulse directed on the specimen surface has been used as US source for impact damage inspection included in biocomposites (Fischer et al. 2019) and CFRP (Rus et al. 2019a). Although piezoelectric or cellular polypropylene transmitters does not match to the optical microphone in their bandwidth, some research has been made using this combination for inspection of monolithic (Rus et al. 2019b) and sandwich CFRP structures (Grager et al. 2018). Broad comparison of methods using optical microphone as US receiver to other NDT methods, has been made in Article #2 (in Appendix).

3.2 Laser Beam Probe

Optical measurements systems using a laser beam as a probe are well suitable for broadband US detection since they have no movable sensing parts that inevitable have their natural behavior. There are methods existing to measure surface displacement or velocity that are sensitive and fast enough to measure motions in the US range. Especially interesting for technical applications are LVs based on Doppler effect and on various measuring techniques implying light interference (Castellini et al. 2006; Lutzmann et al. 2016). Main challenges are related to the sensed surface, which must have sufficient reflectivity at the corresponding wavelength.

LVs have been frequently combined with the laser US excitation (Diot et al. 2013; Park et al. 2014; Sun and Zhou 2014). Typically, specimens are scanned by excitation and sensing beam arranged either on the same side of the specimen (Park et al. 2014; Sun and Zhou 2014), or in through transmission setup (Diot et al. 2013). Change in the wave propagation properties is an indicator for inspected features.

4 Definition of S-scans

Majority of the ACU methods are the most reliable for the inspection of plate-like object. Due to this geometry of the specimen, the 2-dimensional scans are the most relevant to visualize the inspected features. Preserving all the information, the obtained data thus have a form of a 3-dimensional matrix with the following axes: scanning position x , scanning position y , and time (Figure 4.1a). The amplitude value of the captured signal is registered for all the scanning grid positions for all the time instances.

The captured signal can be converted to the frequency domain individually for all the scanning positions. The obtained data matrix has the following axes: scanning position x , scanning position y , and frequency (Figure 4.1b). The amplitude value of the frequency components is registered for all of the scanning grid positions.

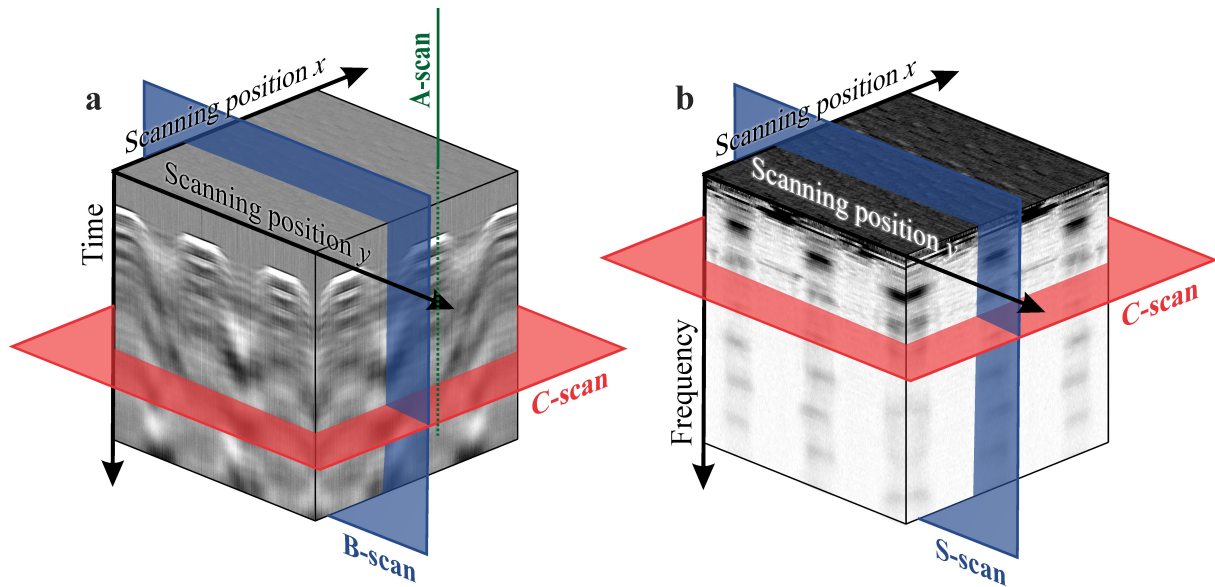


Figure 4.1: Data matrix of the 2-dimensional scan in the time (a) and in the frequency (b) domain can be visualized by slicing it planes of different orientations. B-scan and S-scan (B-scan in frequency domain) are marked in blue. C-scans obtained from data matrix in time and frequency domains are marked in red. The signal amplitude shown in grayscale is symbolic.

Inspecting the 2-dimensional region in broadband frequency range, entire 3-dimensional data matrix in time and frequency domains is analyzed by slicing it into various cross-sectional images. Not only B-scans (in Figure 4.1a marked with blue), but also B-scans in frequency domain gain their importance, if the considered signals are broadband. For the latter, there are in current standards (EN ISO 5577:2017) no names, even though it is frequently used in the fast-developing field of broadband US inspection. We suggest the name S-scans or spectrum-scans (in Figure 4.1b marked with blue), as we have already described in Article #1 (in Appendix).

We would like to emphasize, that when presenting the data in C-scans (in Figure 4.1 marked with red), it is important to signify, which amplitude is coded in the gray- or colorscale, what is not well defined in standards. If it is obtained from time domain, it is important do label the

time instant of this amplitude, or if the peak-to-peak/maximum/minimum amplitude inside of certain interval considered. If the amplitude is taken from frequency domain, the corresponding frequency (interval) needs to be defined. As described in Article #1 (in Appendix) and in Section 5.4, different time intervals and frequencies carry different information about the inspected features.

In contrary, D-scans (time-of-flight) and F-scans (feature-scans – often showing the peak frequency in certain frequency range) are better defined and more representative since they deliver the true physical value, and not a relative one as it is generally the case for the amplitude for uncelebrated US detectors

We favor linear grayscale over a colorscale, since it has only two degrees of freedom (minimum and maximum level) and is therefore more objective for presentation of a single parameter – amplitude. Furthermore, we want to avoid confusion, when the scan results of a broadband US are shown in “real” colorful 3-dimensional scale, on which we can discern the US amplitude, the frequency of its monochromatic equivalent, and the presence of other frequencies components (Section 6).

5 Acoustic Spectroscopy in Non-Destructive Testing

Spectral analysis is a standard part of processing the obtained signal. There are rather technical reasons why acoustic/US spectroscopy is not even more widespread in the field of NDT. There is a tendency of switching to higher US frequencies in order to improve inspection resolution and detection sensitivity. It is technically challenging to excite broadband US in higher frequency range that would have sufficient intensity to overcome the attenuation in the propagation volume and to be detected by the broadband sensor (Section 2 and 3). More frequently resonant transducers are used instead – especially for ACU applications. If the transducers are in physical contact to the specimen (Harmon et al. 2002) or immersed in water (Cousins and Markham 1977), the acoustic spectroscopy is easier to be applied due to the matching of acoustic impedances (Section 1.2). However, the transducers applied on the specimen's surface, or surrounding medium of higher density influence the mechanical behavior of the specimen and the natural frequencies that carry additional information about the inspected features are harder to be accessed.

However, there are still certain contact-free and broadband NDT methods that focus on the spectral analysis of the US, which we review in the following subsections.

5.1 Local Defect Resonance

Solodov and Kreutzbruck conducted an extensive study on local defect resonances (LDR). They excited the specimen in a frequency sweep mode by a broadband piezoelectric transducer fixed on the specimen surface (Hettler et al. 2016; Rittmann et al. 2019; Segers et al. 2018; Solodov et al. 2013) or by air-coupled piezoelectric loudspeaker (Solodov et al. 2017; Solodov et al. 2016). They analyzed natural vibrations of flat-bottom holes, delaminations, undulations, and adhesive disbands, which are typically the most pronounced in the frequency range up to several hundred kHz – but mostly below 100 kHz or in the audible frequency range (depending on the damage form, shape, size and material). While the US excitation was fixed, the locations of the damages and the vibration patterns were obtained by LV scanning the specimen surface. Applications using robot-guided transducers (1 kHz to 100 kHz) and an acoustic camera were demonstrated as well (Bernhardt et al. 2020).

5.2 Impact-Echo

In the field of civil engineering, impact-echo is an often used term for a NDT method related to the subject of broadband acoustic/US inspection (ASTM standard C 1383 - 98a). Mostly, it designates the method where the concrete structure is excited at a point of interest by an impact (often with a specific hammer) and the acoustic response (echo) is captured by a contact receiver (Gibson and Popovics John 2005; Sansalone and Streett 1997). The information about the interior of the inspected concrete structure (wall thickness, internal

delaminations, etc.) can be obtained by the analysis of the received signal in frequency and time domain.

The term *impact-echo* is not suitable for the method of our research. Firstly, US is not excited by a mechanical impact to the specimen. Impact with an equivalent spectral power distribution of the laser or TAE US source, could be only obtained by a rigid and small ball/hammer, which would incident the specimen surface with velocities that are technically hardly feasible (Požar et al. 2017). Secondly, the methods, which we research in this work, do not deal with real echo but rather with LR of feature or defect. A physical contact to the specimen is thus not favorable since it can influence the natural oscillations of the specimen.

5.3 Local Acoustic Resonance Spectroscopy

Local acoustic resonance spectroscopy (LARS) is a more sophisticated method based on well-known principle of a coin-tapping test (Cawley and Adams 1988). It is based on the effect that internal features (e.g. delaminations, voids or larger cracks) influence acoustic response of the specimen excited by an impact (Grosse et al. 2018; Jatzlau and Grosse 2018; Jatzlau et al. 2016; Jüngert et al. 2014). Interpretation of the obtained acoustic waves is improved by using a contact-free microphone in order to avoid subjective interpretation of a human listener. Furthermore, the repeatability of the acoustic excitation is improved by exchanging a coin with a hammer, which records the force history during the impact. The method can be automated and internal features can be visualized by performing a scan. LARS can be used for inspection of larger specimens to determine the critical areas, which can be in the next step inspected by more precise and more rigorous NDT methods. Applications of LARS for inspection CFRP plates and GFRP wind rotor blades were demonstrated (Grosse et al. 2018; Jatzlau and Grosse 2018; Jatzlau et al. 2016; Jüngert et al. 2014). Disadvantages are connected with the interpretation of the results (specially for complex geometry) and inspection resolution, which is low because LARS is limited to (near) audible frequency range, if mechanical impact is used as an acoustic source.

5.4 Local Ultrasonic Resonance Spectroscopy

Acoustic attenuation increases for higher frequencies. Increasing the excitation frequency, the response of the specimen depends more and more on local mechanic properties. The inspection resolution of LARS can thus be improved by switching to higher acoustic frequency range. With the term local ultrasonic resonance spectroscopy (LURS) (*ultrasonic* instead of *acoustic*), we emphasize that the spectral analysis of the LR is predominantly in US frequency range. This is technically feasible by using broadband emitters (e.g. laser pulse – Section 2.4) and receivers (e.g. optical microphones – Section 3.1), which must be mechanically detached from the specimen to ensure its free vibration.

LURS can be defined as a method, where the specimen is excited locally by a short mechanical pulse, and its mechanical response is captured at a position nearby. The spectrum

of the mechanical response is influenced by local geometric, material and condition properties. The parameters, which carry the information about the addressed properties (e.g. amplitude or frequency of certain LR), are extracted and the inspected features of the specimen are visualized while performing a scan.

In Article #1 (in Appendix), we demonstrate LURS for inspection of CFRP plate including delaminations, flat-bottom hole and aluminum inclusions. In Article #3, we measure plate thickness and reliefs of both plate surfaces by LURS.

Furthermore, we applied LURS on a specimen, which included an impact damage. The specimen used in all experiments of this section is described in (Rus et al. 2019a) and in Article #2 (in Appendix). In broadband frequency range we compare the inspection results while using three different US sources: laser pulse, TAE and piezoelectric transducer. The same US receiver was used in through-transmission setup – Eta450 optical microphone. As shown at the beginning of Section 4, the 3-dimensional data matrix is shown by different cross-sectional images: B-scans, S-scans and C-scans at different frequencies.

5.4.1 Laser Pulse and Eta450 Optical Microphone

In Figure 5.1 and Figure 5.2, we elaborate the results of the same scan as described in (Rus et al. 2019a) and in Figure 2i in Article #2 (in Appendix). Additional details about the experiment are described there.

In Figure 5.1 we present B-scan and S-scan at 37 mm scanning position x . Since the signal is broadband, B-scans are shown in exploded view (Figure 5.1a) and in the short time interval (Figure 5.1b). Its frequency spectrum is shown in the frequency range up to 0.4 MHz (Figure 5.1c) and up to 3 MHz (Figure 5.1d). The amplitude coded in grayscale is expressed relatively to the maximum value of each B- or S-scan.

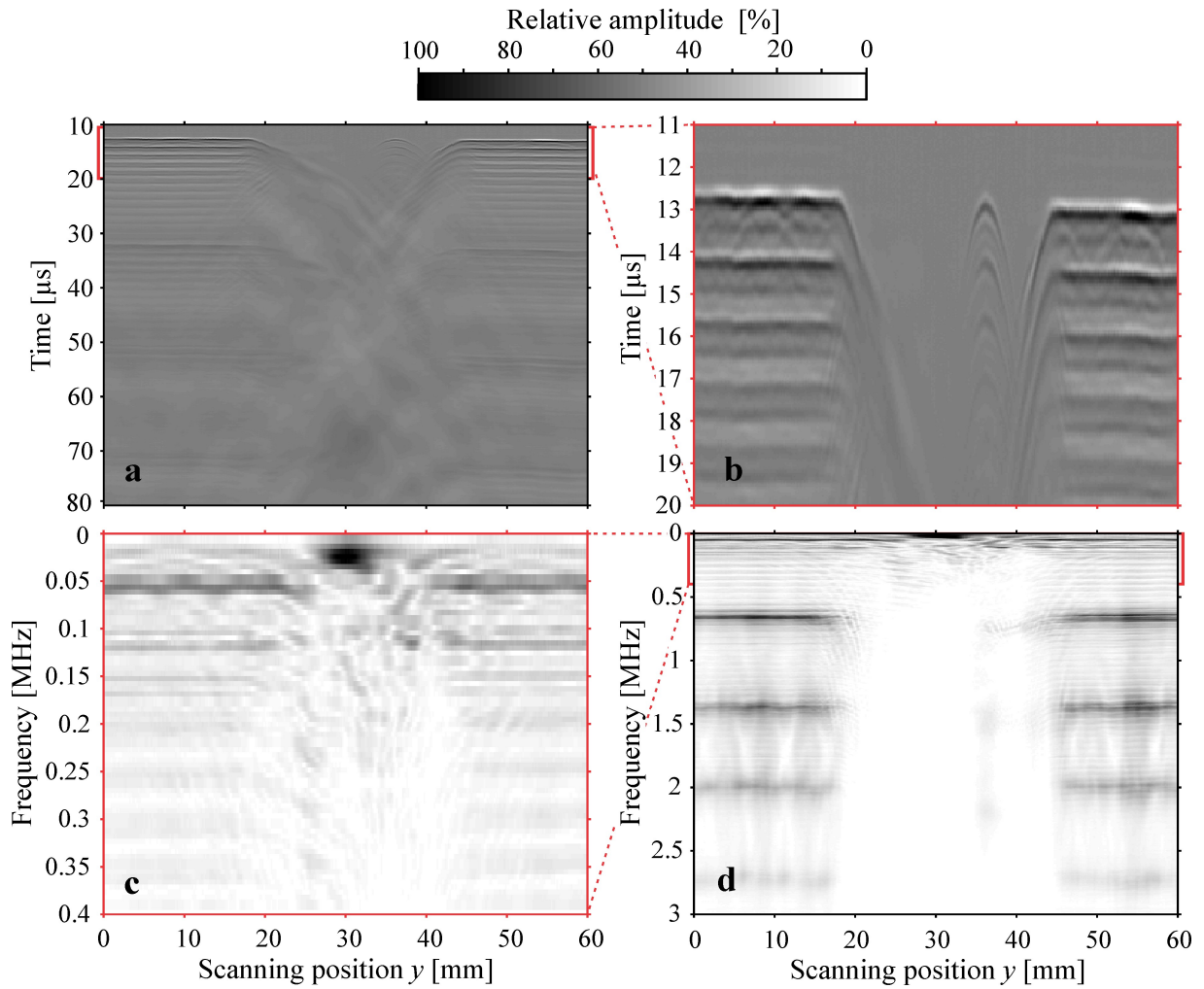


Figure 5.1: B-scan of a CFRP plate including an impact damage of full length (a) and zoomed to the first part of the wave train (b) obtained by a laser pulse and an optical microphone. S-scans (B-scans in frequency domain) of low (c) and high (d) frequency range. The impact damage extends from 19 mm to 45 mm scanning position y . For details about the experimental setup, please refer to Article #2 (in Appendix).

The impact damage can be the most precisely indicated by the absence of high-frequency components (above 500 kHz) in the captured US. 19 μs after the first break, the in-air reflection between the plate and optical microphone is visible in Figure 5.1a. The low frequency oscillations detected between 19 mm and 45 mm scanning position x , where the impact damage is located, arrive with a time delay to the first break at undamaged plate area. The in-plate reflections are well visible at undamaged plate area and have an approximate period of 1.5 μs (Figure 5.1b).

In the lower frequency range (up to 500 kHz), there are augmentations of the transmitted US observable (Figure 5.1c), which are chaotically distributed over the damaged area. The peak at 24 kHz at 30 mm scanning position x is especially prominent. The frequency range between 1.5 kHz and 2.5 kHz carry the information about the geometry of fiber bundles of the layer close to the US detector. TR frequency peak is at approximately 650 kHz.

Figure 5.2 shows C-scans at chosen US frequencies (indicated above each scan) of the same scan as in Figure 5.1. The amplitude coded in grayscale is expressed relatively to the maximum value of each C-scan.

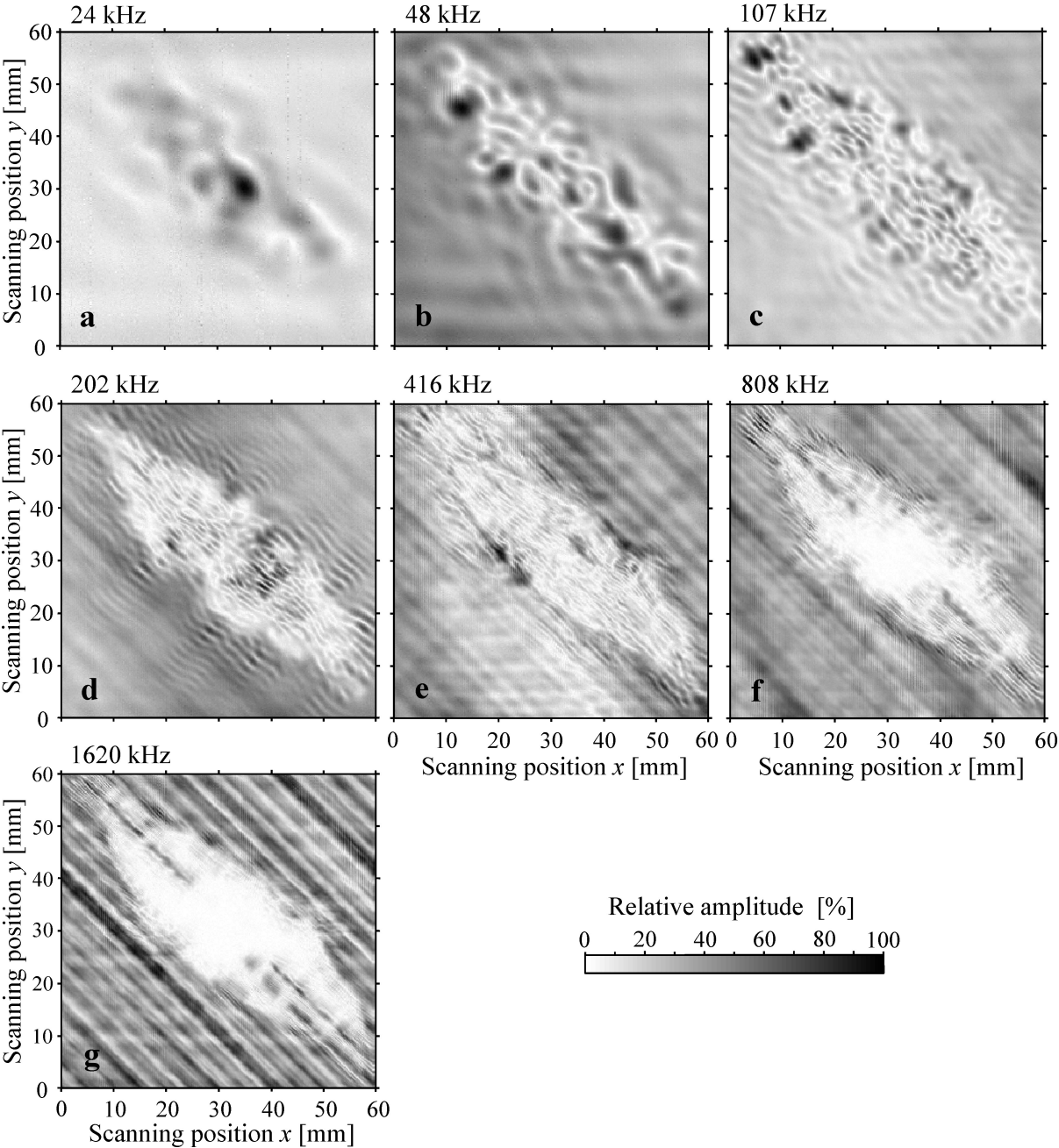


Figure 5.2: C-scans of an impact damage at various frequencies obtained by a single broadband scan using a laser pulse and an optical microphone. In the frequency range up to 500 kHz, chaotically distributed LDRs cause variation of US amplitude (a-e) at the impact damage. High frequency components (800 kHz and above) are highly dissipated in the damaged area (f, g). For details about the experimental setup, please refer to Article #2 (in Appendix).

The specimen was excited by a local pulse at each of the scanning position. As detected by an optical microphone located on the other side of the CFRP plate, there are some continuous increases of detected US amplitude present in the low frequency range (up to 500 kHz). They are chaotically distributed in the area where the CFRP plate was damaged by the impact. This variation of amplitude has higher spatial frequency if higher US frequency is considered.

This phenomenon can be explained by mechanical interference, TR, and delamination clapping in the chaotic shape of the impact damage. Certain regions of the impact damage respond at certain frequencies with their LDR, observable as local increases of the detected US in Figure 5.2a e.g. at (30 mm, 30 mm) (scanning position x , scanning position y), in Figure 5.2b at (13 mm, 45 mm), in Figure 5.2c at (13 mm, 38 mm), in Figure 5.2d at (40 mm, 25 mm), and in Figure 5.2e at (20 mm, 30 mm).

In the frequency range above 500 kHz, more of US is attenuated in the area of the impact damage (Figure 5.2f). The surface of the damage can be well estimated in the frequency range above 1.5 MHz since almost no US of this frequency range is transmitted through the plate where at least one internal delamination is present (Figure 5.2g).

5.4.2 Thermoacoustic Emitter and Eta450 Optical Microphone

For the results shown in Figure 5.3 and Figure 5.4, we exchanged the laser US excitation system with a TAE, which was capable of 2- μ s long US pulse excitation. US receiver (Eta450 optical microphone) and the specimen remained the same. The experimental setup is described in Article #2 (in Appendix).

In Figure 5.3, we present B-scan and S-scan at the same position of the scan as in Figure 5.1 (37 mm scanning position x), applied on the same specimen. The amplitude coded in grayscale is expressed relatively to the maximum value of B- or S-scan.

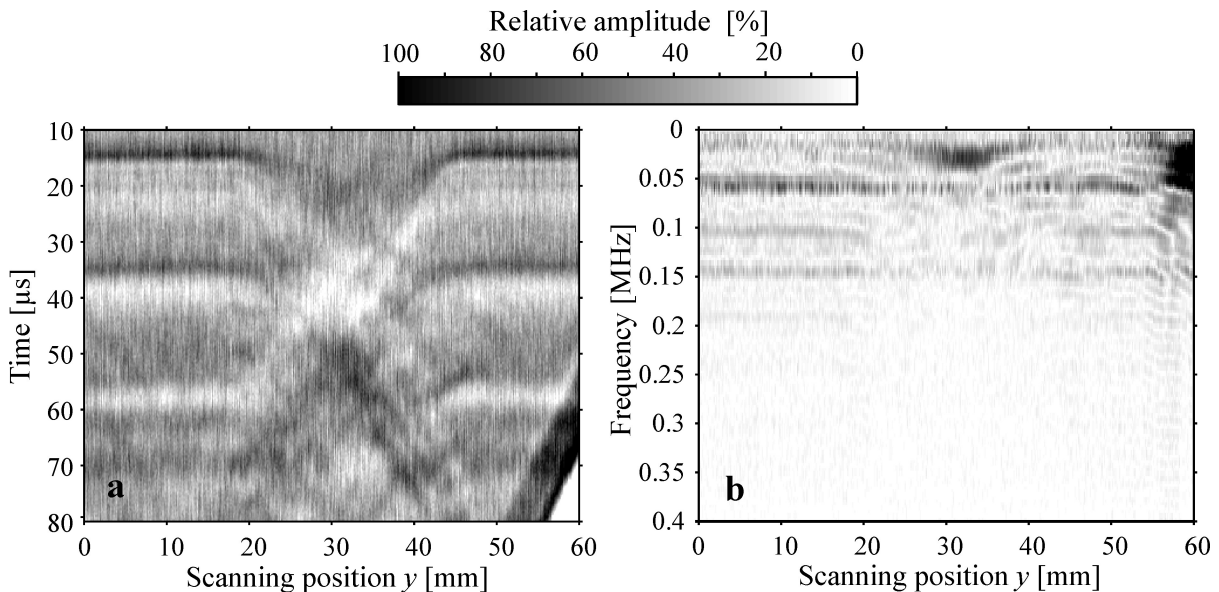


Figure 5.3: B-scan (a) and S-scan (B-scan in frequency domain) (b) of a CFRP plate including an impact damage obtained by a TAE and an optical microphone. The impact damage extends from 19 mm to 45 mm scanning position y . For details about the experimental setup, please refer to Article #2 (in Appendix).

Comparing to Figure 5.1, where laser pulse is used instead of TAE to generate US in the specimen, the scan results in Figure 5.3 has much lower SNR. Their general shape is otherwise similar – including the low-frequency oscillation present between 19 mm and 45 mm scanning position x where the impact damage is present. In-plate reflections are less

pronounced, but still visible from 15 μs to 22 μs in Figure 5.3a. Reflection between the specimen and the optical microphone arrives 22 μs after the first break of the signal.

S-scan in Figure 5.3b is similar to the S-scan in Figure 5.1c. LDR of the impact damage at 24 kHz is visible at both, as well as peak at approximately 0.6 kHz, which lays close to the TR frequency of the plate. The frequency spectrum depends also on the frequency characteristic of the experimental setup. It was demonstrated by the reference measurement, where optical microphone was set directly in the soundfield of the TAE, without the specimen (Figure 3.2).

Figure 5.4 shows C-scans at the first four US frequencies (indicated above each scan) that match to those of Figure 5.2. The data sets of Figure 5.4 and Figure 5.3 were obtained by the same scan.

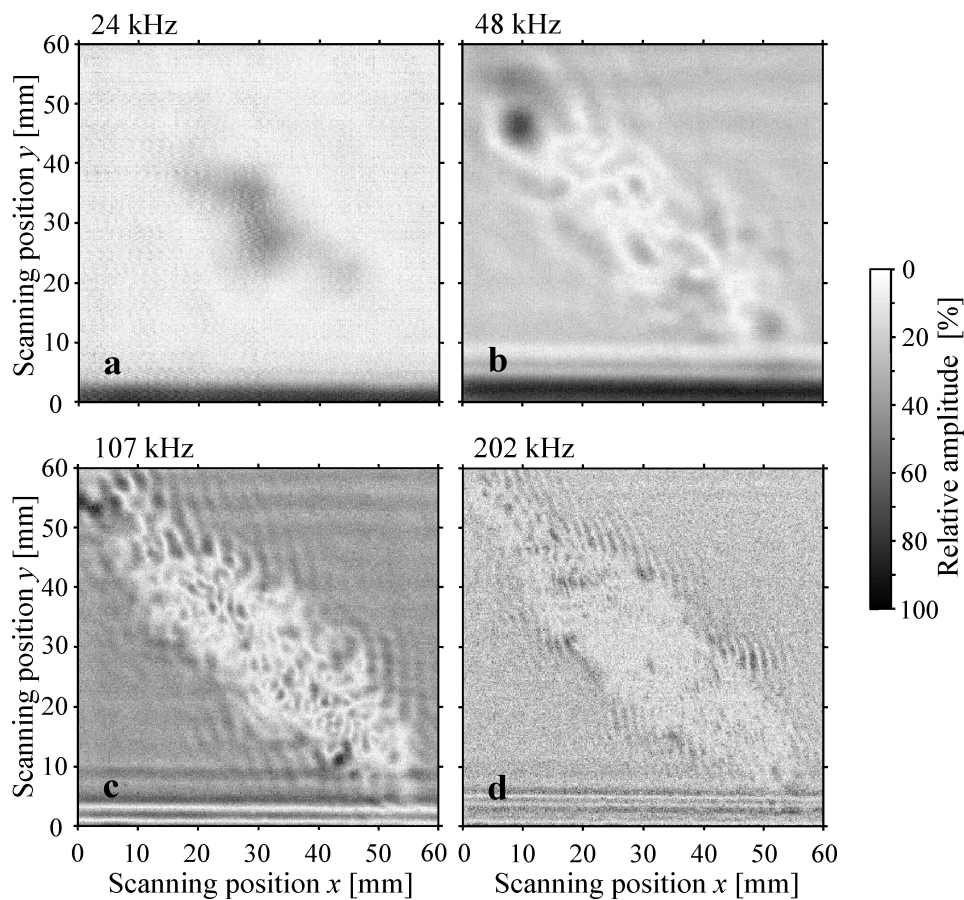


Figure 5.4: C-scans of an impact damage at various frequencies obtained by a single broadband scan using a TAE and an optical microphone. Chaotically distributed LDRs cause variation of US amplitude at the location of the impact damage. For details about the experimental setup, please refer to Article #2 (in Appendix).

The specimen was excited by the TAE at each of the scanning position. As detected by an optical microphone located on the other side of the CFRP plate, the continuous increases of detected US amplitude are located at similar positions than if the US is excited by a laser pulse (Figure 5.2). This shows that they depend on the specimen and impact damage properties rather than on the properties of the US source. Their location strongly depends on

the considered US frequency. They appear in Figure 5.4a at (30 mm, 30 mm) (scanning position x , scanning position y) and in Figure 5.4b at (10 mm, 45 mm).

The variation of amplitude at the impact damage location has higher spatial frequency if higher US frequency is considered (Figure 5.4), which is also the case in Figure 5.2.

5.4.3 Piezoelectric Transducers and Eta450 Optical Microphone

Broadband US setups using laser pulse and TAE were compared to the experiment with two conventional narrowband piezoelectric transducers.

Transducer AirTech 200 from Hillger NDT had 200 kHz nominal frequency and bandwidth of 21 kHz (-6 dB). The diameter of its oscillator was 11.1 mm, its near-field length 18 mm, and the diameter of its soundfield in focus 3 mm (-6 dB). Transducer Sonoair CF 400 from Sonotec had nominal frequency of 400 kHz and bandwidth of 25 kHz (-6 dB). The diameter of its oscillator was 20 mm, its near-field length 5 cm, and the diameter of its soundfield in focus 4 mm (-6 dB), as specified by the manufacturer. These parameters were additionally studied by (Kulla 2019).

The impact specimen was set in the focus of each transducer. The Eta450 optical microphone was used as a US receiver in through-transmission setup. Detector-to-specimen distance was approximately 4 mm in both cases. Scan resolution was 0.25 mm². US was excited by eight rectangular pulses of 400 V for CF 400 and 200 V for AirTech. For additional details about the experimental setup, please refer to (Dzafic 2020; Rus et al. 2020; Rus et al. 2019b).

The resulting C-scans are shown in Figure 5.5. Since they have been obtained on the same specimen, they can be compared to Figure 5.2 and Figure 5.4 at the corresponding frequencies.

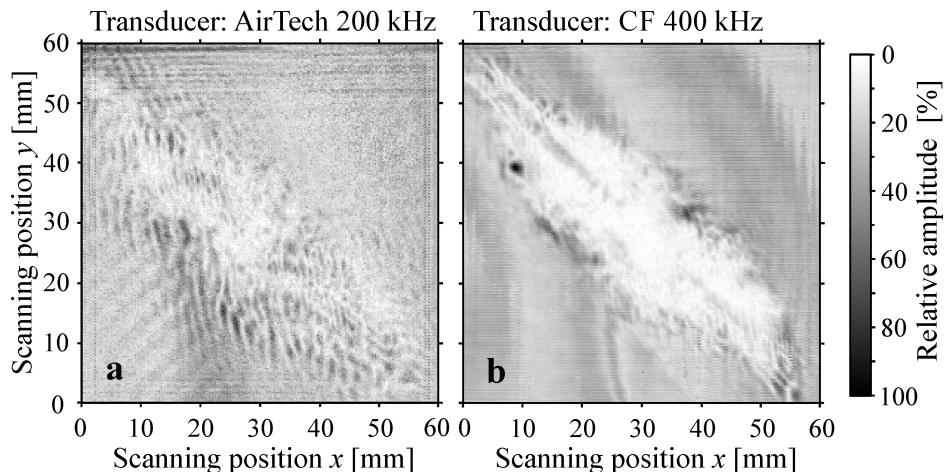


Figure 5.5: C-scans of an impact damage as obtained by an optical microphone and narrowband piezoelectric transducers of 200 kHz (a) and 400 kHz (b) nominal frequency used as US sources. The specimen is the same as in the previous figures of this section. For additional details, please refer to (Dzafic 2020).

We can compare C-scans, which show the U amplitude of the same frequency range. In Figure 5.2d, Figure 5.4d, and Figure 5.5a one can observe the similar spatial variation of

amplitude at the impact damage location, which refer to the US of 200 kHz. The same applies for the US of 400 kHz in Figure 5.2e and Figure 5.5b.

Broadband methods using laser pulse or TAE can be used as a reference to determine a specific frequency, which optimally indicates the defect and can be on the other hand well transmitted through the specimen. This frequency can be afterwards used in a conventional ACU setup utilizing more cost-efficient narrowband piezoelectric transducers.

6 Ultrasound in Colors

A human eye is able to perceive within certain accuracy and limitations the light spectrum in the visible frequency range. Three different sensing cells are sensitive at different frequency ranges (Smith and Guild 1931). We can perceive the colors that can be described by three color appearance parameters: e.g. by (middle/average/monochromatic equivalent) frequency (wavelength, hue), amplitude (brightness, lightness, value) and presence of other frequency components (colorfulness, chroma, saturation). A human eye is not able to uniquely detect the spectrum of the incident light. By the given light spectrum, it is possible to determine the color perceived by a standard observer, while the light of various different spectrums can appear to a standard observer as the same color.

However, this ability of a human eye is advantageous for the presentation of broadband signals obtained by a 2-dimensional scan. The use of broadband US sources and detectors opens a new dimension in US inspection. Using light as an analogy, monochromatic US becomes colored and the inspected object can be analyzed by showing results in “real” colorful scale values. For each scanning position, three parameters can be derived from the displayed color: US amplitude, frequency of the equivalent monochromatic US, and the presence of other frequency components of the US, as shown in the 2-dimensional colorbar in Figure 6.1. It was built by shifting the monochromatic frequency of constant amplitude over the sensitivity distribution of CIE 1931 standard observer (Smith and Guild 1931). The resulted rainbow colors are shown in the vertical dimension of the colorbar. In one horizontal dimension we decreased the amplitude of the monochromatic component, and in the another horizontal dimension we increased the white noise. Please note that a noise of different spectrum distribution could bring us to the same result. As written above, human eye is not able to fully distinguish the frequency spectrum of the incident light. However, colors offer an intuitive and coherent way of presenting broadband 2-dimensional scan results.

In Figure 6.1a we show the results of the same scan as described in Section 5.4.1, (Rus et al. 2019a), and Figure 2i in Article #2 (in Appendix). We integrally present the signal in the broadband frequency range by the colorful US. In this way, it is possible to present more information for each of the scanning locations than by a single monochromatic C-scan. The frequency range of the rainbow colors is set in the frequency range between 0 MHz and 1.2 MHz, which made the impact damage the most visible. Amplitude was shown in logarithmic scale relatively to the maximal value of the scan.

In a similar way we present the results of a second scan, which is described in Article #1 (in Appendix). The frequency range of the rainbow is set in the frequency range between 0 MHz and 0.59 MHz and the amplitude is shown in logarithmic scale relatively to the maximal value.

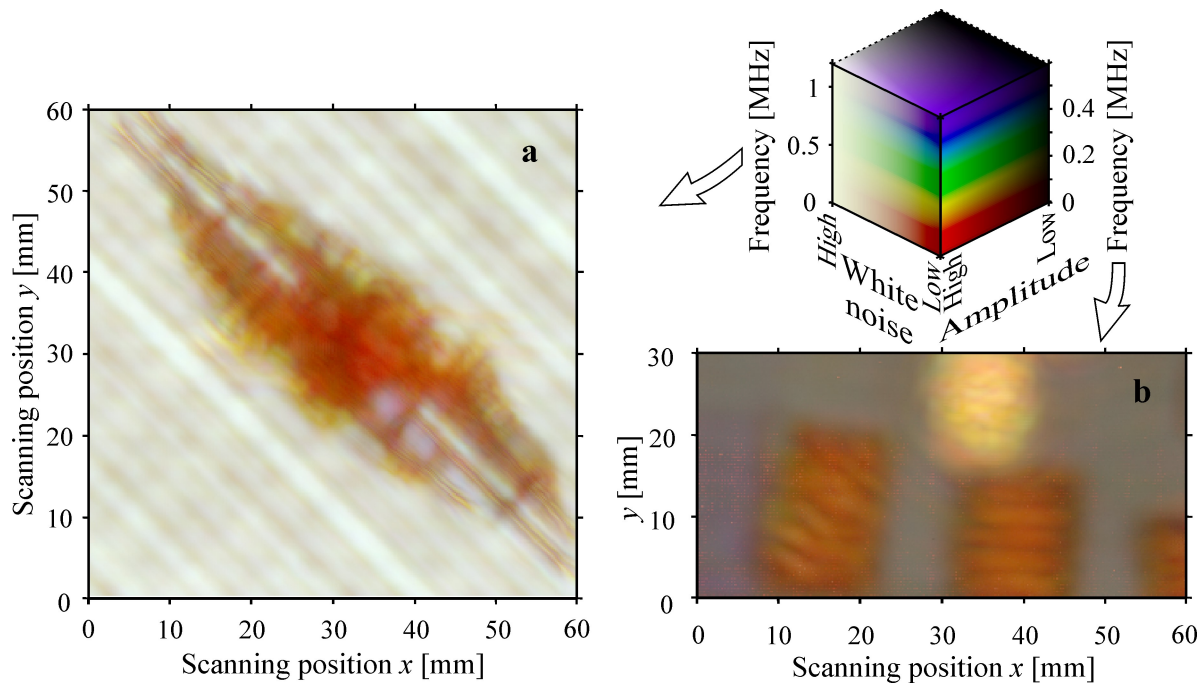


Figure 6.1: Scan results obtained by the broadband US shown in colors. At the impact damage only low-frequency (red) US components are detected, while the damage-free plate area transmits broadband (white) US and variation of intensity reveals the fiber orientation of the layer close to the detector (a). The aluminum inclusions cause slightly visible shift to purple frequency components at scanning positions x below 8 mm, while the tree delaminations are visible in red color (b). Flat-bottom hole transmits more of the US, which is visible as bright yellow circle (b). For details about the experimental setup, please refer to Article #1 and Article #2 (both in Appendix).

Results of a broadband US scan can be interpreted more straightforward, if shown in colors. At the location of the impact damage, the low frequency components prevail in the detected US spectrum, which is visible in strong red color chaotically mixed with orange and yellow (Figure 6.1a). The center of the impact damage is strictly red. The yellow and light green components at the boundary of the damage demonstrate that US of higher frequency components can be detected there (its full spectrum is shown in S-scans in Figure 5.1). Undamaged plate transmits broadband US, which is visible in white color in Figure 6.1a. The shape and orientation of the fiber bundles on the plate side close to the optical microphone is visible by variation of the white color intensity (grey stripes).

LDR of delaminations lay in the lower frequency range comparing to the US transmitted through the plate without delaminations. This is visible by red-orange squares in Figure 6.1b. The shape if the natural oscillation of the delamination is visible as yellow and dark-red stripes. Flat-bottom hole transmits high intensity of the broadband US, which is visible as a bright yellow circle in Figure 6.1b. Relatively to these high amplitude components, the rest of the delamination-free plate appears grey. This indicates the broadband US, which is detected there. At scanning positions x below 8 mm, the individual fiber layers were replaced by the aluminum foils. Since pressure wave velocity is higher in aluminum (approximately 6300 m/s) than in CFRP (2700 m/s perpendicularly to the fiber orientation), the aluminum inclusions cause shift to higher frequencies. This is visible in white-purple color in Figure 6.1b. Please refer to Article #1 (in Appendix) for more information about this effect.

7 Outline of Article #1

Article #1, *Local Ultrasonic Resonance Spectroscopy: A Demonstration on Plate Inspection*, (published in the *Journal of Nondestructive Evaluation*) is contained in its full form in Appendix and cited as (Rus and Grosse 2020).

Key points of Article #1:

- US was induced in a CFRP plate by laser pulses for all the scanning positions.
- Innovative broadband contact-free US detector was used to capture the US in through-transmission setup.
- LDR of flat-bottom hole and delaminations were detected at specific US frequencies.
- The features of the specimen were visualized by observing amplitude and peak frequency of LDR and TR.

Article #1 is the first of two original research papers, in which we introduced a new approach to US signal analysis, which we designated LURS. It extends already established LARS to higher frequencies.

It was initiated by a novel method for US generation and detection, which made it possible to effectively excite and capture US in a broadband frequency range (several kHz to several MHz) without physical contact to the specimen, assuring free local vibrations of the specimen. Furthermore, this method allowed us to perform a scan with high repeatability and to record the local mechanical response in US frequency range for all the scanning positions in through-transmission setup.

We experimentally demonstrated on a CFRP plate specimen that it is possible to characterize the local properties of the specimen with an approach, similar to vibration and modal analysis, now extended to the US frequency range. LDR of delaminations and a flat-bottom hole were detected in the frequency range below 110 kHz. The shift of the TR frequency of the plate and its higher-order resonance frequencies carry the information about the aluminum inclusions. This can find numerous applications in industrial inspection and quality control.

7.1 Authors' Contributions for Article #1

Both authors conceived of the idea about the experiment. J.R. carried out the experiments in cooperation with XARION Laser Acoustics (listed in the acknowledgements) and performed the data evaluation. The result were discussed and interpreted by both authors. J.R. wrote the final manuscript in consultation with C.U.G..

8 Outline of Article #2

Article #2: *Qualitative Comparison of Non-Destructive Methods for Inspection of Carbon Fiber-Reinforced Polymer Laminates*, (published in the *Journal of Composite Materials*) is contained in its full form in Appendix and cited as (Rus et al. 2020).

Key points of Article #2:

- Cellular polypropylene transducers provide a contrast improvement over piezoelectric transducers.
- Laser-induced US is a better indicator for delaminations than μ CT and comparable with immersion testing.
- TAE and optical microphones offer the potential for broadband ACU inspection.
- The porosity and presence of microcracks can be effectively detected by X-ray dark-field radiography.
- Optimal inspection methods were recommended, which depend on the certain testing constraints.

In Article #2, we qualitatively and concisely compare altogether thirteen inspection methods in order to survey the ongoing development and evaluate the advantage of novel test methods. They were applied on a specific specimen – a CFRP laminate with induced impact damage. We use this specimen as a reference for characterization of innovative and already established NDT methods: cellular polypropylene as an alternative to piezoelectric transducers, couplant-free broadband contact-free US emitters (laser pulse, TAE) and receivers (optical microphone), US immersion testing, phased array US testing, optically excited lock-in thermography, and X-ray radiography (projectional absorption and dark-field, tomosynthesis, and microcomputed tomography).

From our experimental results, it is possible to anticipate the direction of future research in this field. The provided conclusions are advantageous also for the readers, who are searching for a suitable solution for a specific industrial inspection task with requirements exceeding the capabilities of conventional methods. Complementary use of radiographic and US methods is discussed.

8.1 Authors' Contributions for Article #2

The project was initiated and coordinated by J.R.. The experiments and the data evaluation were carried out by J.R., A.G., H.M., J.G., and K.B.. The result were discussed and interpreted by all the authors. J.R. wrote the manuscript with the contribution and critical feedback of A.G., H.M., J.G., K.B., M.G., and C.U.G.. The project was supervised by M.G., F.P., and C.U.G..

9 Outline of Article #3

The bibliographic data of Article #3, *Thickness Measurement via Local Ultrasonic Resonance Spectroscopy* (published in *Ultrasonics*), are listed in Appendix and cited as (Rus and Grosse 2021).

Key points of Article #3:

- Mechanical responses of a plate excited by laser pulses were effectively detected in the US frequency range by a contact-free optical microphone.
- TR frequency and time of arrival are independent parameters if US is generated on the specimen surface and detected in air.
- Reliefs of both plate surfaces were visualized together with the plate thickness by extracting the TR frequency and the time of arrival for all the scanning positions.
- The measured relief of the plate surface illuminated by the laser is influenced by changes in the plate material, while the measured surface relief on the opposite side of the plate remains unaffected.

The present manuscript is the second of two original research papers, which we published to introduce LURS. Article #1 is focused on inspection of local material properties, while article #3 deals with the inspection of geometrical properties of the specimen i.e. plate thickness. We decided to publish them separately due to the diverging objectives of the two LURS experiments.

In Article #3, we describe the measurement of the plate thickness with a LURS spectroscopy setup, which allowed us to record the local mechanical response in US frequency range for all scanning positions without physical contact to the specimen. US excited by a laser pulse on the specimen surface, is detected in a broadband frequency range (several kHz to several MHz) in air on the opposite side of a plate with variable thickness. This makes it possible to identify the pressure and (mode-converted) shear waves using an air-coupled sensor.

Plate curvature (reliefs of both plate surfaces) can be measured together with the plate thickness, if the arrival time of US wave train is considered together with the TR frequency. The measured relief of the plate surface illuminated by the laser is thereby altered by moderate changes in the plate material, while the measured relief on the opposite side of the plate remains unaffected. This is demonstrated for the first time by Article #3 and can find numerous industrial applications. In conclusion we address possible implementations of this principle for the inspection of objects with complex geometry by advanced US tomography.

9.1 Authors' Contributions for Article #3

Both authors conceived of the idea about the experiment. J.R. carried out the experiments in cooperation with XARION Laser Acoustics (listed in the acknowledgements) and performed the data evaluation. The result were discussed and interpreted by both authors. J.R. wrote the final manuscript in consultation with C.U.G..

10 Cross-Thematic Discussion

The strategy of the scientific communication provided by the three articles included in this work was to introduce a new approach to broadband US analysis, on a basement formed by an experimental comparison of various inspection methods as indicated by the graphic in Figure 10.1. Article #2 (in Appendix) provides a broad overview of the innovative alternative methods (black text in the blue square) setting them side-by-side with already established conventional inspection methods (white text on the dark background). Thus we review the state-of-the-art possibilities for CFRP impact damage inspection, which we extend with some novel implementations.

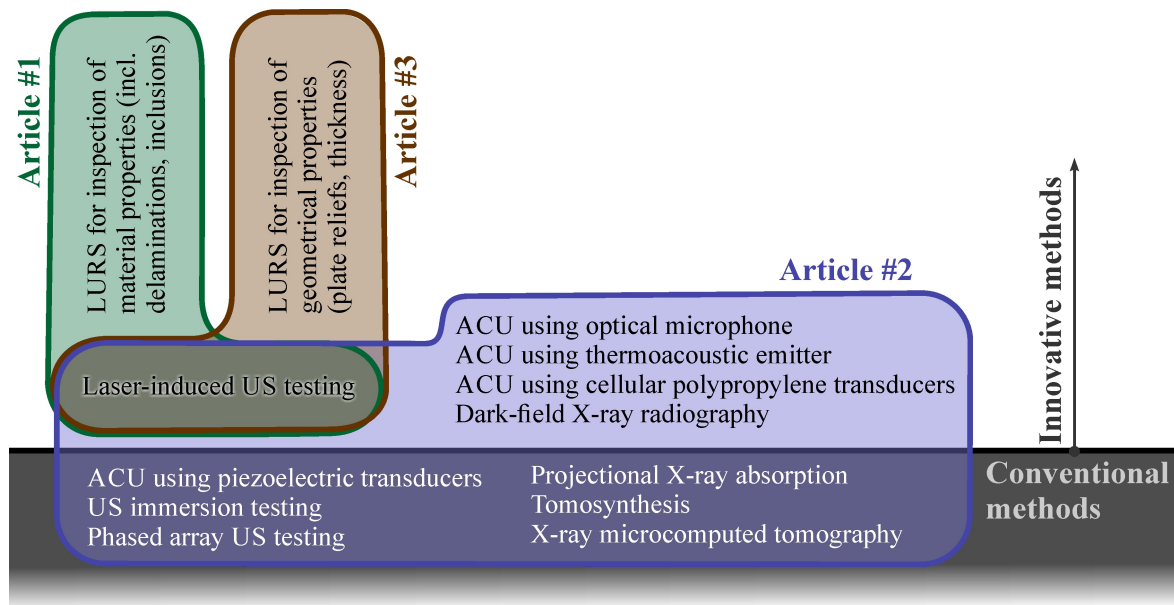


Figure 10.1: Schematic presentation of the inspection methods addressed by the articles, which constitute the presented work. Articles #1 (in Appendix) and Article #3 demonstrate the application of LURS for inspection of material (inclusions, damages) and geometrical properties (plate relief and thickness) of the specimen, while Article #2 (in Appendix) forms a thematic basement made by a broad experimental comparison of CFRP inspection methods.

By LURS it is possible to extract the mechanical properties of the specimen: about the specimen material or geometry. Each of the articles #1 and #3 cover one of these two aspects. In Article #1 (in Appendix), we describe that from the spectrum of the local mechanical response, it is possible to detect LDR of delaminations and flat-bottom hole. The aluminum inclusions in the CFRP plate are detected by the shift of the TR frequency at constant plate thickness.

On the other hand, in Article #3, we focus on the specimen, whose material is kept constant and we vary the plate thickness. By the analysis of TR and time of arrival, it is possible to measure the reliefs of both plate surfaces (plate curvature) together with the plate thickness in the scanned region.

As illustrated in Figure 10.1, laser induced US, used to demonstrate LURS and included in the comparison of inspection methods, is a common topic of all three articles.

In the introduction of Article #1 (in Appendix), we give an overview of the previous experiments that used the broadband US spectrum for specimen characterization – including ACU, laser US, LARS and LDR. In Article #2 (in Appendix), we review the literature, which dealt with the comparison of US, radiographic, optical and thermographic methods. In Article #3, we describe the previous realizations that applied US spectrum analysis for determining the plate thickness without physical contact to the specimen. Additional literature research is also included in Section 5.

Outlook

Last paragraph of the conclusion of each of the three articles is dedicated to the goals of the future work. We studied the specimens with the plate geometry only. The possibilities and limitations of LURS applied on the specimens of more complex geometry are to be researched in the future. This method carries the potential for all the specimens that can be mechanically excited by a broadband source (laser pulse, TAE) and is conditioned by how efficiently the local natural oscillations can be detected. Addressing the localized properties that affect the mechanical response spectrum in higher frequency range, LURS represent the bridge between vibration (modal) analysis and US inspection.

Additional studies are to be made how the location of the US detector relatively to the US source affects the signal. Since US is can be excited by the laser directly in the specimen, it is a promising method for single-side inspection implementations. The scan process should be optimized for the specimens of more complex geometries. We expect that after performing LURS at different locations and by changing specimen's orientation and inverse modeling operations applied on the obtained signal, it is possible to reconstruct detailed geometry and material properties. This method would have an advantage over X-ray computed tomography, since the mechanical waves/vibration is directly influenced by the features that have a crucial influence on the integral mechanical properties of the inspected object. On the other hand, some other features can be better detected by the X-ray computed tomography. The data obtained by the both methods could be fused, what might deliver some additional information otherwise inaccessible using only one imaging principle.

11 References

ASTM C1383-98a. *Standard Test Method for Measuring the P-Wave Speed and the Thickness of Concrete Plates Using the Impact-Echo Method*, West Conshohocken: ASTM International.

EN ISO 5577:2017. *Non-destructive testing - Ultrasonic testing - Vocabulary*.

Bass, H. E., Sutherland, L. C., Zuckerwar, A. J. (1990). Atmospheric absorption of sound: Update. *The Journal of the Acoustical Society of America*, 88(4), 2019-2021, doi: 10.1121/1.400176.

Bell, A. G. (1881). The Production of Sound by Radiant Energy. *Science*, os-2(49), 242-253, doi: 10.1126/science.os-2.49.242.

Bernhardt, Y., Solodov, D., Müller, D., Kreutzbruck, M. (2020). Listening for Airborne Sound of Damage: A New Mode of Diagnostic Imaging. *Frontiers in Built Environment*, 6(66), doi: 10.3389/fbuil.2020.00066.

Blomme, E., Bulcaen, D., Declercq, F. (2002). Air-coupled ultrasonic NDE: Experiments in the frequency range 750 kHz-2 MHz. *NDT & E International*, 35, 417-426, doi: 10.1016/S0963-8695(02)00012-9.

Castellini, P., Martarelli, M., Tomasini, E. P. (2006). Laser Doppler Vibrometry: Development of advanced solutions answering to technology's needs. *Mechanical Systems and Signal Processing*, 20(6), 1265-1285, doi: 10.1016/j.ymssp.2005.11.015.

Cawley, P., Adams, R. D. (1988). The mechanics of the coin-tap method of non-destructive testing. *Journal of Sound and Vibration*, 122(2), 299-316, doi: 10.1016/S0022-460X(88)80356-0.

Cousins, R. R., Markham, M. F. (1977). The use of ultrasonic spectroscopy in the location of delaminations in fibre-reinforced polymers. *Composites*, 8(3), 145-152, doi: 10.1016/0010-4361(77)90008-8.

Daschewski, M., Boehm, R., Prager, J., Kreutzbruck, M., Harrer, A. (2013). Physics of thermo-acoustic sound generation. *Journal of Applied Physics*, 114(11), 114903, doi: 10.1063/1.4821121.

Davies, S. J., Edwards, C., Taylor, G. S., Palmer, S. B. (1993). Laser-generated ultrasound: its properties, mechanisms and multifarious applications. *Journal of Physics D: Applied Physics*, 26(3), 329-348, doi: 10.1088/0022-3727/26/3/001.

Delrue, S., Van Den Abeele, K., Blomme, E., Deveugele, J., Lust, P., Matar, O. B. (2010). Two-dimensional simulation of the single-sided air-coupled ultrasonic pitch-catch technique for non-destructive testing. *Ultrasonics*, 50(2), 188-196, doi: 10.1016/j.ultras.2009.08.005.

- Dewhurst, R. J., Hutchins, D. A., Palmer, S. B., Scruby, C. B. (1982). Quantitative measurements of lasergenerated acoustic waveforms. *Journal of Applied Physics*, 53(4064), 4064-4071, doi: 10.1063/1.331270.
- Diot, G., Koudri-David, A., Walaszek, H., Guégan, S., Flifla, J. (2013). Non-destructive Testing of Porosity in Laser Welded Aluminium Alloy Plates: Laser Ultrasound and Frequency-Bandwidth Analysis. *Journal of Nondestructive Evaluation*, 32(4), 354-361, doi: 10.1007/s10921-013-0189-5.
- Dzafic, S. (2020). Experimental Comparison of Air-Coupled Ultrasonic Testing Methods. *Master's thesis, Chair of Non-Destructive Testing, Technical University of Munich.*
- Fischer, B. (2016). Optical microphone hears ultrasound. *Nature Photonics*, 10, 356-358, doi: 10.1038/nphoton.2016.95.
- Fischer, B., Sarasini, F., Tirillò, J., Touchard, F., Chocinski-Arnault, L., Mellier, D., Panzer, N., Sommerhuber, R., Russo, P., Papa, I., Lopresto, V., Ecault, R. (2019). Impact damage assessment in biocomposites by micro-CT and innovative air-coupled detection of laser-generated ultrasound. *Composite Structures*, 210, 922-931, doi: j.compstruct.2018.12.013.
- Gaal, M., Bartusch, J., Dohse, E., Kreutzbruck, M., Amos, J. (2014). Air-coupled ultrasonic testing of metal adhesively bonded joints using cellular polypropylene transducers. *AIP Conference Proceedings*, 1581(1), 471-478, doi: 10.1063/1.4864857.
- Gaal, M., Bartusch, J., Dohse, E., Schadow, F., Köppe, E. (2016a). Focusing of ferroelectret air-coupled ultrasound transducers. *AIP Conference Proceedings*, 1706(1), 080001, doi: 10.1063/1.4940533.
- Gaal, M., Bartusch, J., Schadow, F., Beck, U., Daschewski, M., Kreutzbruck, M. (2016b). Airborne ultrasonic systems for one-sided inspection using thermoacoustic transmitters. *IEEE International Ultrasonics Symposium*, doi: 10.1109/ULTSYM.2016.7728787.
- Gaal, M., Caldeira, R., Bartusch, J., Schadow, F., Vössing, K., Kupnik, M. (2019a). Air-coupled ultrasonic ferroelectret receiver with additional bias voltage. *IEEE Transactions on Ultrasonics, Ferroelectrics, and Frequency Control*, 1600-1605, doi: 10.1109/TUFFC.2019.2925666.
- Gaal, M., Döring, J., Bartusch, J., Lange, T., Hillger, W., Brekow, G., Kreutzbruck, M. (2013). Ferroelectret transducers for air-coupled ultrasonic testing of fiber-reinforced polymers. *AIP Conference Proceedings*, 1511(1), 1534-1540, doi: 10.1063/1.4789224.
- Gaal, M., Hufschläger, D., Bente, K. (2019b). Advances in air-coupled ultrasonic transducers for non-destructive testing. *International Congress on Ultrasonics*, 38, doi: 10.1121/2.0001072.

- Gan, T. H., Hutchins, D. A., Billson, D. R., Schindel, D. W. (2001). The use of broadband acoustic transducers and pulse-compression techniques for air-coupled ultrasonic imaging. *Ultrasonics*, 39(3), 181-194, doi: 10.1016/S0041-624X(00)00059-7.
- Gibson, A., Popovics John, S. (2005). Lamb Wave Basis for Impact-Echo Method Analysis. *Journal of Engineering Mechanics*, 131(4), 438-443, doi: 10.1061/(ASCE)0733-9399(2005)131:4(438).
- Grager, J. C., Kotschate, D., Gamper, J., Gaal, M., Pinkert, P., Mooshofer, H., Goldammer, M., Grosse, U. C. (2018). Advances in air-coupled ultrasonic testing combining an optical microphone with novel transmitter concepts. *12th ECNDT Gothenburg, Sweden*.
- Grosse, C. U. (2013). Evolution of NDT Methods for Structures and Materials: Some Successes and Failures. In O. Güneş and Y. Akkaya (eds.), *Nondestructive Testing of Materials and Structures*. Dordrecht: Springer.
- Grosse, C. U. (2016). Modules for an efficient and holistic application of NDT methods for fiber reinforced polymers. *17th European Conference on Composite Materials, Munich*.
- Grosse, C. U., Jüngert, A., Jatzlau, P. (2018). Local Acoustic Resonance Spectroscopy. In N. Ida and N. Meyendorf (eds.), *Handbook of Advanced Non-Destructive Evaluation*. Springer, doi: 10.1007/978-3-319-30050-4_21-1.
- Haller, M. I., Khuri-Yakub, B. T. (1994). A surface micromachined electrostatic ultrasonic air transducer. *Proc. of IEEE Ultrasonics Symposium*, 2, 1241-1244, doi: 10.1109/ULTSYM.1994.401810.
- Harmon, L. M., Gyekenyesi, A. L., Martin, R. E., Baaklini, G. Y. (2002). Investigations of delaminations with ultrasonic spectroscopy. *SPIE NDE For Health Monitoring and Diagnostics*, 4704, doi: 10.1117/12.470722.
- Hettler, J., Tabatabaeipour, M., Delrue, S., Van Den Abeele, K. (2016). Detection and Characterization of Local Defect Resonances Arising from Delaminations and Flat Bottom Holes. *Journal of Nondestructive Evaluation*, 36(1), doi: 10.1007/s10921-016-0380-6.
- Hutchins, D. A. (1986). Mechanisms of pulsed photoacoustic generation. *Canadian Journal of Physics*, 64(9), 1247-1264, doi: 10.1139/p86-217.
- Jatzlau, P., Grosse, C. U. (2018). Local Acoustic Resonance Spectroscopy: An Escalation Approach for Fast Non-Destructive Testing. *10th International Symposium on NDT in Aerospace*.
- Jatzlau, P., Müller, M., Grosse, C. U. (2016). Identification of Flawed CFRP Samples Using Local Acoustic Resonance Spectroscopy (LARS). *WCNDT, 19th World Conference on Non-Destructive Testing*.

Jüngert, A., Grosse, C., Krüger, M. (2014). Local Acoustic Resonance Spectroscopy (LARS) for Glass Fiber-Reinforced Polymer Applications. *Journal of Nondestructive Evaluation*, 33(1), 23-33, doi: 10.1007/s10921-013-0199-3.

Kotschate, D., Gaal, M., Kersten, H. (2018). Acoustic emission by self-organising effects of micro-hollow cathode discharges. *Applied Physics Letters*, 112(15), 154102, doi: 10.1063/1.5024459.

Krautkrämer, J., Krautkrämer, H. (1990). *Ultrasonic Testing of Materials*. Berlin Heidelberg: Springer, doi: 10.1007/978-3-662-10680-8.

Kulla, D. (2019). Investigation of Focused Transducers for Air-Coupled Ultrasound Testing. *Bachelor's thesis, Chair of Non-Destructive Testing, Technical University of Munich*.

Kupnik, M., Min-Chieh, H., Vaithilingam, S., Khuri-Yakub, B. T. (2011). CMUTs for air coupled ultrasound with improved bandwidth. *Proc. of IEEE International Ultrasonics Symposium*, 592-595, doi: 10.1109/ULTSYM.2011.0143.

Ladabaum, I., Xuecheng, J., Soh, H. T., Atalar, A., Khuri-Yakub, B. t. (1998). Surface micromachined capacitive ultrasonic transducers. *IEEE Transactions on Ultrasonics, Ferroelectrics, and Frequency Control*, 45(3), 678-690, doi: 10.1109/58.677612.

Lange, P. D., John, W. S. (1915). On thermophones. *Proceedings of the Royal Society A: Mathematical, Physical and Engineering Science*, 91, 239-241, doi: 10.1098/rspa.1915.0015.

Lutzmann, P., Göhler, B., Hill, C., van Putten, F. (2016). Laser vibration sensing at Fraunhofer IOSB: review and applications. *Optical Engineering*, 56(3), doi: 10.1117/1.OE.56.3.031215.

Meschede, D. (2017). *Optics, Light, and Lasers: The Practical Approach to Modern Aspects of Photonics and Laser Physics*. Weinheim: Wiley.

Na, S., Chen, A. I. H., Wong, L. L. P., Li, Z., Macecek, M., Yeow, J. T. W. (2016). Capacitive micromachined ultrasonic transducers based on annular cell geometry for air-coupled applications. *Ultrasonics*, 71, 152-160, doi: 10.1016/j.ultras.2016.06.008.

Na, S., Zheng, Z., Chen, A. I., Wong, L. L. P., Li, Z., Yeow, J. T. W. (2017). Design and Fabrication of a High-Power Air-Coupled Capacitive Micromachined Ultrasonic Transducer Array With Concentric Annular Cells. *IEEE Transactions on Electron Devices*, 64(11), 4636-4643, doi: 10.1109/TED.2017.2746006.

Park, B., An, Y.-K., Sohn, H. (2014). Visualization of hidden delamination and debonding in composites through noncontact laser ultrasonic scanning. *Composites Science and Technology*, 100, 10-18, doi: 10.1016/j.compscitech.2014.05.029.

Podymova, N. B., Karabutov, A. A. (2014). Broadband Laser-Ultrasonic Spectroscopy for Quantitative Characterization of Porosity Effect on Acoustic Attenuation and Phase Velocity

in CFRP Laminates. *Journal of Nondestructive Evaluation*, 33(1), 141-151, doi: 10.1007/s10921-013-0210-z.

Požar, T., Laloš, J., Babnik, A., Petkovšek, R., Bethune-Waddell, M., Chau, K. J., Lukasiwicz, G. V. B., Astrath, N. G. C. (2018). Isolated detection of elastic waves driven by the momentum of light. *Nature Communications*, 9(1), 3340, doi: 10.1038/s41467-018-05706-3.

Požar, T., Rus, J., Petkovšek, R. (2017). Optical Detection of Impact Contact Times with a Beam Deflection Probe. *Experimental Mechanics*, 57(8), 1225–1238, doi: 10.1007/s11340-017-0289-8.

Preisser, S., Rohringer, W., Liu, M., Kollmann, C., Zotter, S., Fischer, B., Drexler, W. (2016). All-optical highly sensitive akinetic sensor for ultrasound detection and photoacoustic imaging. *Biomedical optics express*, 7(10), 4171-4186, doi: 10.1364/BOE.7.004171.

Qin, Q., Attenborough, K. (2004). Characteristics and application of laser-generated acoustic shock waves in air. *Applied Acoustics*, 65(4), 325-340, doi: 10.1016/j.apacoust.2003.11.003.

Rittmann, J., Rahammer, M., Holtmann, N., Kreutzbruck, M. (2019). Impactschäden sicher finden Vorstellung eines Prototyps für die mobile Ultraschall-Thermografie. *DGZfP Jahrestagung*.

Rus, J., Fischer, B., Grosse, C. U. (2019a). Photoacoustic inspection of CFRP using an optical microphone. *Proc. SPIE, Optical Measurement Systems for Industrial Inspection XI*, 1105622, doi: 10.1117/12.2525021.

Rus, J., Grosse, C. U. (2020). Local Ultrasonic Resonance Spectroscopy: A Demonstration on Plate Inspection. *Journal of Nondestructive Evaluation*, 39(2), doi: 10.1007/s10921-020-00674-5.

Rus, J., Grosse, C. U. (2021). Thickness measurement via local ultrasonic resonance spectroscopy. *Ultrasonics*, 109, 106261, doi: 10.1016/j.ultras.2020.106261.

Rus, J., Gustschin, A., Mooshofer, H., Grager, J.-C., Bente, K., Gaal, M., Pfeiffer, F., Grosse, C. U. (2020). Qualitative comparison of non-destructive methods for inspection of carbon fiber-reinforced polymer laminates. *Journal of Composite Materials*, 57(27), 4325-4337, doi: 10.1177/0021998320931162.

Rus, J., Kulla, D., Grager, J. C., Grosse, C. U. (2019b). Air-Coupled Ultrasonic Inspection of Fiber-Reinforced Plates Using an Optical Microphone. *Proc. of German Acoustical Society, DAGA Rostock*, 763-766.

Sansalone, M., Streett, W. B. (1997). *Impact-echo: Non-destructive Evaluation of Concrete and Masonry*. Michigan: Bullbrier Press.

Sause, M. G. R., Stoessel, R., Oster, R., Soehnchen, R., Jahnke, P., Seemann, A., Goldammer, M., Grosse, C. U. (2016). MAIzfp – A Joint Research Effort on NDT of Fiber Reinforced Composites within the Leading-Edge Cluster MAI Carbon. *Prof. of 19th World Conference on Non-Destructive Testing*.

Schindel, D. W., Hutchins, D. A. (1995). Through-thickness characterization of solids by wideband air-coupled ultrasound. *Ultrasonics*, 33(1), 11-17, doi: 10.1016/0041-624X(95)00011-Q.

Scruby, C. B., Drain, L. E. (1990). *Laser ultrasonics: techniques and applications*. New York: Taylor & Francis.

Segers, J., Kersemans, M., Hedayatrasa, S., Calderon, J., Van Paepegem, W. (2018). Towards in-plane local defect resonance for non-destructive testing of polymers and composites. *NDT & E International*, 98, 130-133, doi: 10.1016/j.ndteint.2018.05.007.

Smith, T., Guild, J. (1931). The C.I.E. colorimetric standards and their use. *Transactions of the Optical Society*, 33(3), 73-134, doi: 10.1088/1475-4878/33/3/301.

Solodov, I., Bai, J., Busse, G. (2013). Resonant ultrasound spectroscopy of defects: Case study of flat-bottomed holes. *Journal of Applied Physics*, 113(22), 223512, doi: 10.1063/1.4810926.

Solodov, I., Dillenz, A., Kreutzbruck, M. (2017). A new mode of acoustic NDT via resonant air-coupled emission. *Journal of Applied Physics*, 121(24), 245101, doi: 10.1063/1.4985286.

Solodov, I., Döring, D., Busse, G. (2010). Air-Coupled Lamb and Rayleigh Waves for Remote NDE of Defects and Material Elastic Properties. *Strojniski Vestnik*, 56(9), 557-564.

Solodov, I., Rahammer, M., Gulnizkij, N., Kreutzbruck, M. (2016). Noncontact Sonic NDE and Defect Imaging Via Local Defect Resonance. *Journal of Nondestructive Evaluation*, 35(3), 48, doi: 10.1007/s10921-016-0364-6.

Sun, G., Zhou, Z. (2014). Application of laser ultrasonic technique for non-contact detection of drilling-induced delamination in aeronautical composite components. *Optik*, 125(14), 3608-3611, doi: 10.1016/j.ijleo.2014.01.072.

Vössing, K. J., Gaal, M., Niederleithinger, E. (2018). Air-coupled ferroelectret ultrasonic transducers for nondestructive testing of wood-based materials. *Wood Science and Technology*, 52(6), 1527-1538, doi: 10.1007/s00226-018-1052-8.

Wente, E. C. (1922). The Thermophone. *Physical Review*, 19(4), 333-345, doi: 10.1103/PhysRev.19.333.

Wright, W. M. D., Hutchins, D. A. (1999). Air-coupled ultrasonic testing of metals using broadband pulses in through-transmission. *Ultrasonics*, 37(1), 19-22, doi: 10.1016/S0041-624X(98)00034-1.

Wright, W. M. D., Hutchins, D. A., Gachagan, A., Hayward, G. (1996). Polymer composite material characterisation using a laser/air-transducer system. *Ultrasonics*, 34(8), 825-833, doi: 10.1016/S0041-624X(96)00083-2.

Appendix

Article #1: Local Ultrasonic Resonance Spectroscopy: A Demonstration on Plate Inspection

Authors: Janez Rus, Christian U. Grosse

Title: Local Ultrasonic Resonance Spectroscopy: A Demonstration on Plate Inspection

First submission to the publisher: 22 October 2019

Journal: Journal of Nondestructive Evaluation

Publisher: Springer

Accepted: 10 March 2020

Available online: 19 March 2020

Issue date: June 2020

Volume: 39

Issue: 2

DOI: 10.1007/s10921-020-00674-5

Reprint Permission

Open Access. This article is licensed under a Creative Commons Attribution 4.0 International License, which permits use, sharing, adaptation, distribution and reproduction in any medium or format, as long as you give appropriate credit to the original author(s) and the source, provide a link to the Creative Commons license, and indicate if changes were made. The images or other third party material in this article are included in the article's Creative Commons license, unless indicated otherwise in a credit line to the material. If material is not included in the article's Creative Commons license and your intended use is not permitted by statutory regulation or exceeds the permitted use, you will need to obtain permission directly from the copyright holder.



Local Ultrasonic Resonance Spectroscopy: A Demonstration on Plate Inspection

J. Rus¹ · C. U. Grosse¹

Received: 22 October 2019 / Accepted: 10 March 2020
© The Author(s) 2020

Abstract

Local ultrasonic resonance spectroscopy (LURS) is a new approach to ultrasound signal analysis, which was necessitated by a novel inspection method capable of the contact-free, localized, broadband generation and detection of ultrasound. By performing a LURS scan, it is possible to detect local mechanical resonances of various features and of the specimen itself. They are highly sensitive to local mechanical properties. By observing different parameters in the frequency spectrum (e.g., resonance amplitude and resonance peak frequency), geometrical, material and condition properties can be visualized for all of the scanning positions. We demonstrate LURS for inspection of a carbon fiber reinforced polymer plate. Local defect resonances of delaminations and a flat-bottom hole were detected in the frequency range from 25 to 110 kHz. Analyzing the higher frequency range (0.3 MHz to 1.5 MHz) of the same scan, the shift of the thickness resonance frequency of the plate and its higher-order resonance frequencies carry the information about the aluminum inclusions. LURS shows an advantage in characterizing the localized features of the specimens via contact-free ultrasonic inspection.

Keywords Local ultrasonic resonance spectroscopy · Thickness resonance · Local resonance · Ultrasonic inspection

1 Introduction

There are two fundamental approaches to describe the elastodynamic state of a stationary body. On the one hand, motion of the whole body (part) can be considered by observing its non-periodic or (partially) periodic deformations, i.e., theory of vibration or modal analysis. On the other hand, we can study how the mechanical waves distribute in the body, i.e., wave motion theory. The wavelength of the motion can be defined as a decisive criterium. It can be determined from the periodicity of the motion, by knowing the material properties (or wave velocities) of the body. If the wavelength is in an order of magnitude of the size of the body (part) or longer, it is reasonable to use the theory of vibration; if the wavelength is significantly smaller from the size of the body (part), the motion can be better described by wave theory.

However, a certain duality is still present for the transition between these two criteria, and it is especially pronounced

for the motion of a broadband frequency. The experimental equipment used in our experiment allowed us to consider frequencies ranging from several kHz to the MHz range. A pressure wave velocity of 2700 m/s for the test specimen used in this study yielded wavelengths from the meter to the sub-millimeter range. The mechanical behavior in the 4.1 mm thick specimen plate thus encompasses both regimes. Down to 25 kHz, the natural oscillation of a feature is excited together with up to 3-MHz US waves, which have fully distinct thickness reflections. According to the described duality, the thickness reflections can also be interpreted as symmetric oscillations of the plate.

Resonant ultrasound spectroscopy (RUS) is an established method, in which the entire specimen (normally a cube) is excited with the ultrasound (US) in a broadband frequency range [1–3]. The integral material parameters of the specimen are obtained from the natural oscillation frequencies. Local ultrasonic resonance spectroscopy (LURS) uses the same principle, but applied locally.

In LURS, the specimen is excited locally, and its mechanical response is captured at a position nearby. Local resonances of US are acquired from the frequency spectrum of the captured signal. While performing a scan, it is possible to obtain material, geometrical, and other mechanical proper-

✉ J. Rus
janez.rus@tum.de

¹ Chair of Non-Destructive Testing, Centre for Building Materials, Technical University of Munich, Franz-Langinger-Straße 10, 81245 Munich, Germany

ties for each of the scanning-grid locations, or to detect their spatial change.

The term 'local' is relative to the object size, and the requisite criterium is having a size significantly larger than the inspected region. The goal of LURS is to excite only a localized region of the object (e.g., a feature or defect) to capture the natural mechanical behavior thereof. The local region of the object responds with its local resonances. For example, in the case of plates, we can detect the local thickness resonance (TR).

It is evident that even locally excited motion will spread through the entire specimen. However, high frequency components of motion are more strongly attenuated as the distance from the excitation point increases. Thus, for the higher frequencies of the motion considered, we can localize the region of interest, and thereby still use the theory of vibration to approach the problem.

LURS extends local acoustic resonance spectroscopy (LARS) to higher frequencies. In the latter method, the specimen is locally excited by mechanical impact [4–7]. The mechanical response is captured in the air in the audible frequency range by a microphone. Local changes in the material properties affect the amplitude of characteristic frequencies, which can be plotted for all the scanning positions.

LURS uses US excited and captured in broadband frequency range without physically contacting the specimen in order to achieve free local vibrations of the specimen. At the same time, this approach allows us to perform a scan having repeatable inspection properties for all of the scanning locations. A recently developed system comprising a photoacoustic US excitation and broadband optical microphone made this possible.

In comparison to air-coupled ultrasound (ACU) inspection methods, in which, due to the coupling problem, only narrowband transducers are conventionally used, LURS opens a new dimension. Using light as an analogy, monochromatic US becomes colored. By exciting white US, the inspected object can be observed in US colors if the receiver is likewise sensitive to the full frequency spectrum.

To preserve all of the information, data captured by LURS need to be organized in a 3-dimensional matrix. We refer to it as a *scan data matrix*. This matrix has the following axes: scanning position x , scanning position y , and time. The amplitude value of the captured signal for all the time instances is registered for all the scanning grid positions. Furthermore, the captured signal is converted to the frequency domain individually for all the scanning positions. We then obtain a scan data matrix in the frequency domain with the following axes: scanning position x , scanning position y , and frequency. The amplitude value of the frequency components is registered for all of the scanning grid positions. The present research did not study the signal phase or time of arrival, which also contains information about the specimen. In LURS, the entire

3-dimensional scan data matrix in the time and frequency domains is analyzed. This is achieved by slicing the matrix into various cross-sectional images: B-scans, C-scans and F-scans [8]. The recently developed experimental equipment allowed us to acquire the broadband US spectrum at each grid point in the scanned area. Thus, the presentation of the data in frequency domain B-scans gained a great deal of importance. In the growing field of broadband US inspection, it is advantageous to refer to these as S-scans (*spectrum scans*).

In the following, we will provide a brief review of the previous experiments that analyzed broadband US spectrum for specimen characterization. These range from the 1970s, when the first experiments were conducted using an immersion testing setup in which the broadband frequency range was more easily achieved through water coupling [9, 10], until the present. A review of the early applications of ultrasonic spectral analysis to nondestructive evaluation was provided by Fitting and Adler [11].

Ultrasonic spectroscopy is challenging when applied to ACU testing methods. However, there are some alternatives to piezoelectric transducers that have a frequency range broad enough for ultrasonic spectroscopy, e.g., electrostatic (or capacitance) transducers [12, 13]. By applying pulsed US excitation, the thickness resonance (TR) frequency of the specimen plates of different material or thickness was detected in a through-transmission setup using two electrostatic transducers.

Laser-induced ultrasound is an efficient alternative for generating broadband US since it allows generation of short shock waves by means of the thermal (an ablation regime is also feasible) expansion of the illuminated area directly in the specimen [14]. Spectral analysis of US captured via piezoelectric transducer [15, 16] and laser interferometer [17] was performed to obtain information about the specimen. In [15], the level of porosity in carbon fiber-reinforced polymer (CFRP) was measured by observing the resonance peak of attenuation (amplitude and bandwidth) in the frequency domain using water as a couplant medium. The porosity in a laser welding aluminum joint was detected in [17], by observing B-scans of different frequency-bandwidths. In [16] laser-generated US was captured by a piezoelectric transducer. The CFRP including flat-bottom hole and delamination was studied on C-scans and Lamb wave tomography images. A similar experimental setup as the one used in our experiment has already been applied to the inspection of impact damage in biocomposites [18]. The only parameter being analyzed on the US signal captured by the optical microphone was amplitude in the time domain.

An extensive study on local defect resonances (LDR) was conducted by Solodov and Kreuzbruck [19–21]. They analyzed the natural oscillations of flat-bottom holes, delaminations, undulations, and adhesive disbonds. The defects were excited by tunable contact and contact-free (piezoelec-

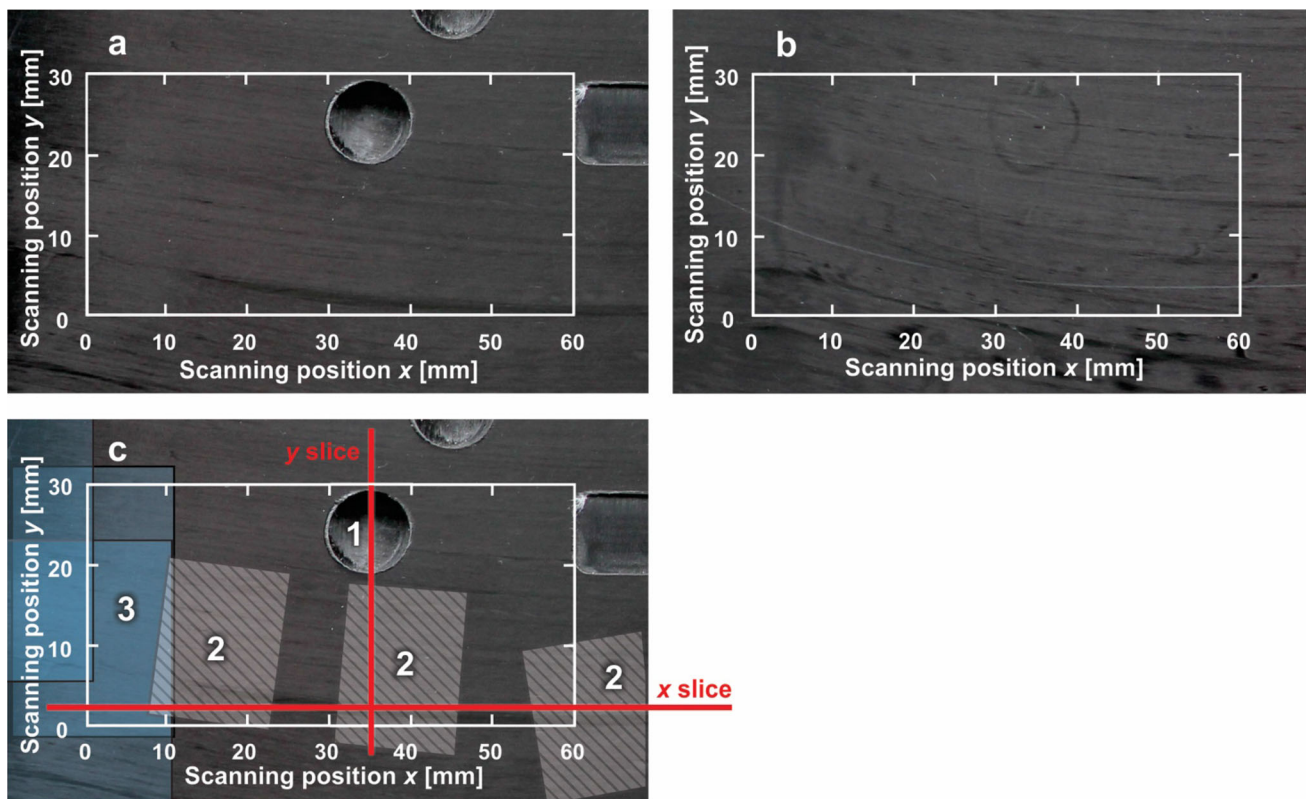


Fig. 1 The back (a) and the front (b) side of the specimen. In (c) the approximate locations of the flat-bottom hole (1), delaminations (2) and aluminum inclusions (3) are marked. The white rectangle with the coordinate system denotes the scan area

tric loudspeakers) transducers. For imaging of the defects, emitting sound at their local defect resonance, air-coupled transducers, microphone or laser vibrometers were used, depending on the frequency range of interest, which was mostly audible sound or near-US (several hundred kHz). Their experiments were supplemented by separate experiments using a piezoelectric patch to activate and a laser vibrometer to detect the local defect resonances [22, 23].

In using LURS, we are combining the local defect resonance approach with the classical US inspection. The local resonance behavior of the specimen can then also be analyzed in the US frequency range, where the information-carrying frequencies of more delicate features (inclusions, material changes) are situated.

2 Specimen Description

The specimen was a 30×30 cm CFRP (carbon fiber reinforced polymer) plate of 4.1 mm thickness [24]. The plate was made of 15 carbon fiber layers with a thickness of 0.27 mm (0° , 90° alternating orientation). Epoxy resin was used as a matrix. The scanned area of the specimen is marked with the white frame in Fig. 1. Red lines mark the cross-sectional locations in the x and y scanning directions in which detailed

LURS was performed in B-scans (Figs. 4 and 5) and S-scans (Figs. 6 and 7).

Three different features (simulated defects) were located in the inspected area of the specimen. The first was a flat-bottom hole (number 1) centered at (35 mm, 25 mm) (scanning position x , scanning position y). It had a diameter of 9.5 mm. The remaining thickness under the hole was approximately 0.29 mm. Due to the drilling process, the remaining layer was slightly bulged out of the surface, as seen in Fig. 1b).

The second feature type was a simulated delamination (number 2) created at three locations that lie (not fully) within the scan area. The each delamination was created by placing a pair of polytetrafluoroethylene (PTFE) films (0.1 mm thickness) between the carbon fiber layers during the manufacturing process of the plate. The PTFE film pair had dimensions of approximately $15 \text{ mm} \times 20 \text{ mm}$. Delaminations were located at depths between 1.5 and 2 mm from the front side of the specimen. By embedding the PTFE pair in the plate, we achieved the mechanical detachment of the matrix between two fiber layers. The simulated delaminations are not clearly visible by computer tomography (CT). We assume that PTFE films are what we were actually detecting by CT rather than the delamination itself.

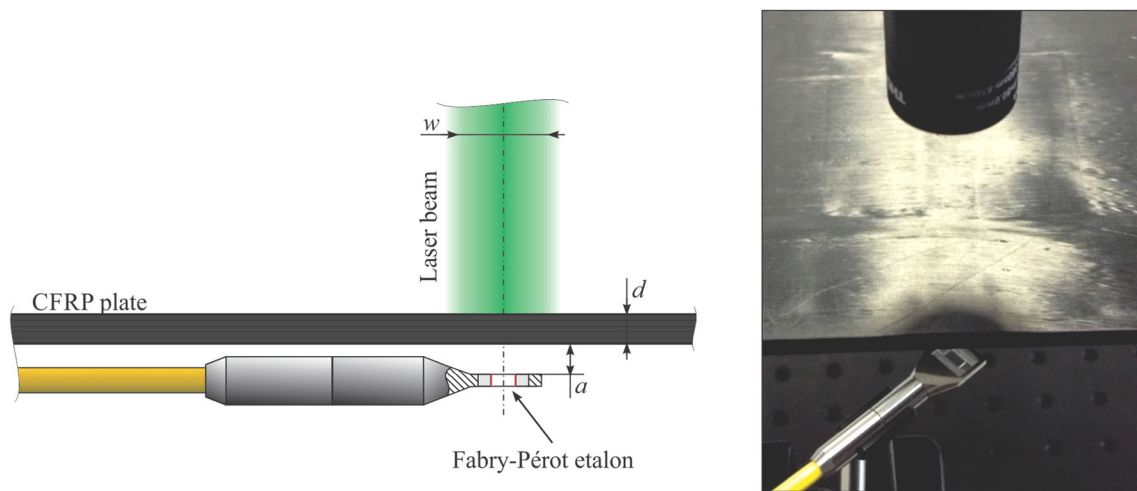


Fig. 2 Scheme and photo of the LURS experimental setup: US is excited by the pulse laser on the front side of the plate. The optical microphone is located on the other side of the plate

The third feature was located below 15 mm scanning position x (number 3). In this area individual fiber layers were replaced by the three pieces of aluminum foil having approximately the same thickness. At least one carbon fiber layer lay between individual aluminum films. Consequently, the matrix came in contact with both sides of the film and the aluminum was adhesively connected to the CFRP, thus simulating the inclusion defect.

Due to the challenging (plate) geometry of the CT scan, the locations of the aluminum foils were determined at a limited precision. Their approximate location is marked with the blue overlapping squares in the area marked as (number 3) in Fig. 1. The foils were shifted with respect to one another in the in-plane direction. As a result, we had areas in the specimen in which either one, two, or three aluminum layers were above each other across the thickness of the plate. The number of aluminum layers can be identified in Fig. 1 by the blue color intensity.

3 Description of LURS Setup

Laser-induced US appears to be the only method capable of inducing high-intensity US over a frequency range broad enough to effectively perform LURS on CFRP plates several mm thick. We used a Nd-YAG frequency-doubled, q-switched pulse laser with a wavelength of 532 nm to generate the blast US waves in the specimen. The laser source was part of US excitation system provided by Xarion Laser Acoustics. The maximal laser pulse repetition rate was 20 Hz. Over the output optic, the laser light was collimated on 8 mm diameter w (95% intensity level). The laser pulse peak intensity was low enough not to exceed the ablation threshold; the US was induced in the thermoelastic regime.

In LURS, a broadband US source needs to be combined with a broadband US detector. We used an Eta450 Ultra optical microphone made by Xarion Laser Acoustics. The optical microphone does not have any moving parts, as is normally the case for conventional US receivers (piezoelectric material or membrane). It measures the US directly in the air by measuring the change of the refractive index as acoustic waves travel through the Fabry-Pérot etalon [18, 25–27]. However, the housing of the microphone itself (or the etalon mirrors) can have a certain natural behavior which could affect the signal. The optical microphone has a frequency range from near-DC to approximately 3 MHz. The sensitivity is 100 mV/Pa, and the self-noise at the full bandwidth (as specified by the manufacturer) is 10 mPa.

The US source and the detector were arranged in a through-transmission setup (Fig. 2) with the laser illuminating the front side of the plate as defined in Fig. 2. The optical microphone was placed in the middle of the laser beam axis on the other side of the plate. US was induced directly in the specimen by the laser pulse. On the receiver side, US was transmitted through an air gap of approximately 4 mm between the specimen and the sensitive part (Fabry-Pérot etalon) of the optical microphone. For LURS, it is advantageous to have the specimen mechanically released at the measurement location (ACU) in order to ensure free local mechanical oscillations. Since we are only considering local oscillations, the clamping of the whole specimen does not have a significant influence on the LURS results.

All of the results of the LURS analysis described in this work were obtained from a single scan 38 min long. The laser beam was used simultaneously with the optical microphone driven over the 60×30 mm area of the CFRP plate while inducing the US at 301×151 grid points (0.2 mm increment length). At each scanning location, the optical

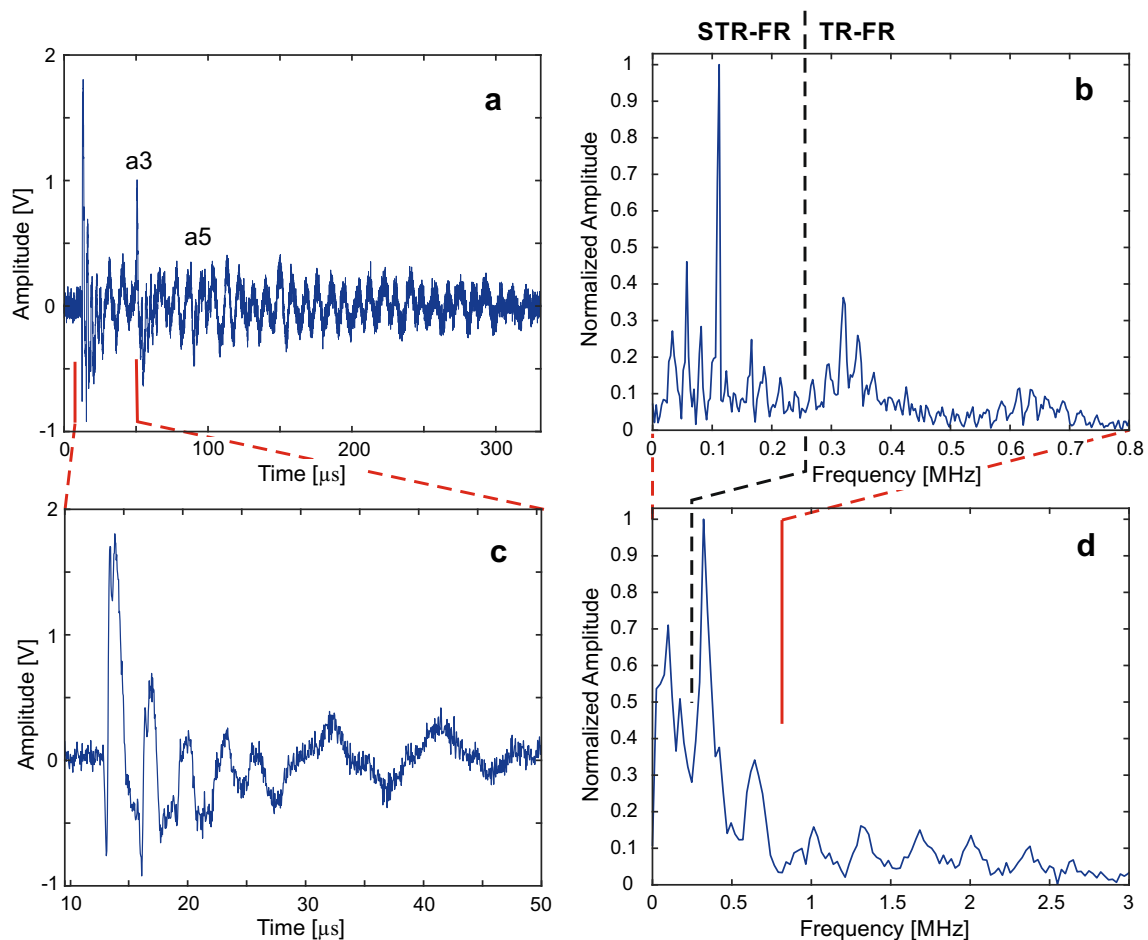


Fig. 3 The typical signal from optical microphone at the undamaged location with its frequency spectrum: in full length (*long time interval*) (a) and zoomed to the *short time interval* (c). b is the frequency spectrum of the *long time interval* signal and d is the frequency spectrum of the *short time interval*

microphone captured the US while being externally triggered by the control unit. No averaging was applied. The signal was digitalized (14-bit values) at a 25 MHz sampling frequency. The sufficient spatial resolution was achieved by small-sized sensitive area of the optical microphone: approximately 0.4 mm^2 , as specified by the manufacturer. For additional details about the experimental setup, please refer to [28].

4 Results of LURS Scan and Discussion

4.1 Typical Signal at Undamaged Location

Since the present research is studying the mechanical behavior of plates over a broadband frequency range, it is advantageous to define two ranges of interest in the frequency domain. We refer to them as the sub-thickness resonance frequency range (STR-FR) and the thickness resonance frequency range (TR-FR). In the STR-FR, local defect reso-

nances, the lower-mode asymmetric plate oscillations (lamb waves), and mechanical oscillation of the full body predominate. The TR-FR was comprised of the TR (first symmetric plate oscillation—lamb wave) and its high-order resonances. The dividing frequency was defined as the TR frequency reduced by a certain factor (e.g., 0.8). As a result, we ensured that all of the observed phenomena of the TR lay in the TR-FR. The dividing frequency was dependent on the US pressure wave velocity (perpendicular to the fiber orientation) and the plate thickness. For our specimen, this amounted to $0.8 \times 330 \text{ kHz} = 264 \text{ kHz}$ since the TR frequency of the specimen was approximately 330 kHz. We require a longer time window for the signal in the STR-FR signal analysis. In contrast, a shorter time window is sufficient for the TR-FR. We are defining a *short time window* as the interval confined between the signal's first brake moment and the first in-air reflection of US between the optical microphone and the specimen (marked as a3 in Fig. 3). *Long time window* is the time interval of the full wave train. This separation is necessary because the low frequency oscillation lasts longer

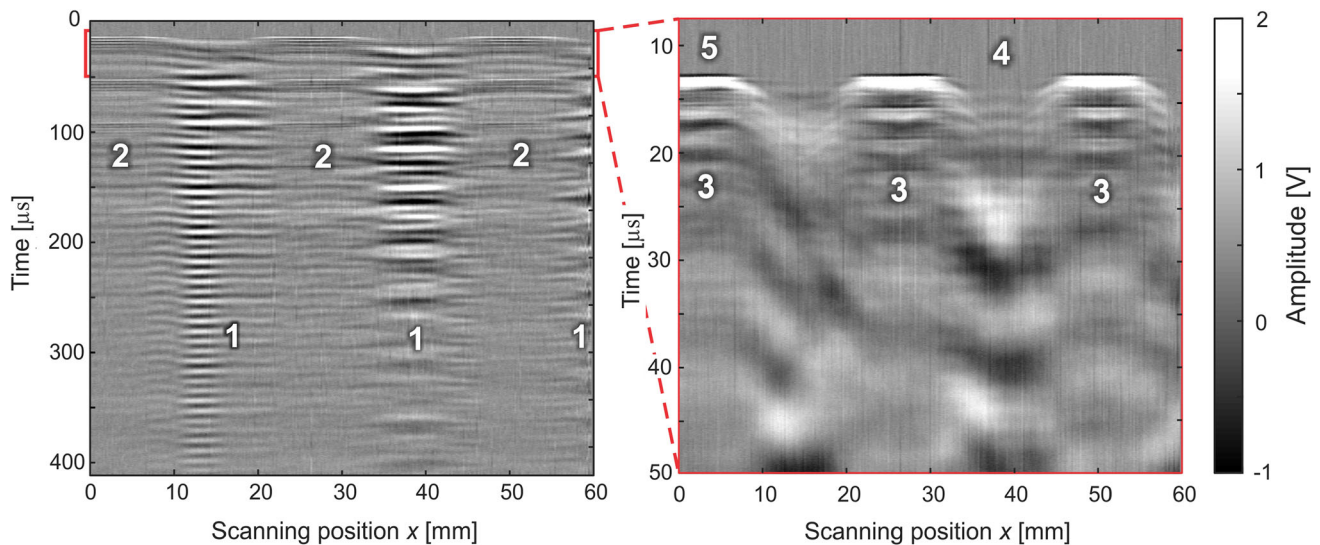


Fig. 4 B-scan at $y = 3$ mm scanning position. The cross-sectional cut goes over three delaminations (located at number 1) and inclusion (located at number 5)

than the time between the in-air US reflection between the optical microphone and the specimen. In another respect, these reflections disturbed the high-frequency analysis of the signal. The following analysis provides a separate indication of which frequency range was used.

Figure 3a shows the full length of the signal (*long time interval*) along with its frequency spectrum Fig. 3b. The red lines mark the *short time interval*, an exploded view of which is shown in Fig. 3c. Figure 3d shows a frequency spectrum of a *short time interval* signal. The signal shown refers to the scanning position at which the laser illuminates the undamaged part of the specimen. The amplitudes of the frequency spectrum are normalized to its maximum value.

In Fig. 3a, one can observe at least two in-air reflections of US between the specimen and the optical microphone (a3 and a5). They can be distinguished as higher-frequency signal oscillations superimposing the lower-frequency signal oscillations, which result from the bending-mode oscillations of the specimen plate or the LDR oscillations. The latter can be detected also at the damage-free area, since they have higher amplitude and are less attenuated in air than the higher frequency US components (e.g. TR). This effect can also be observed in the Fig. 6.

In zooming in to the *short time interval*, we can observe in-plate wave reflections at a period of approximately $3.0 \mu\text{s}$. Given this value and the plate thickness, we can calculate the approximate (and averaged over the plate thickness) pressure wave US velocity in CFRP perpendicular to fiber direction: $2 \times 4.1 \text{ mm} / 3.0 \mu\text{s} = 2700 \text{ m/s}$. The same velocity can also be obtained by the TR of the plate: 330 kHz. This is in agreement with the value expected for CFRP.

The shape of the frequency spectrum changes by reducing the length of the signal. Numerical frequency resolution decreases—being inverse value of the time window. Lower frequencies become less pronounced. Their amplitudes decrease while the frequency peaks in the high-frequency range have a more defined shape (comparing Fig. 3b–d). The TR and seven higher-order resonances of TR are visible.

4.2 B-scans

In the following, the data obtained by a single LURS scan are presented in B-scans, C-scans, F-scans and newly defined S-scan (B-scans in frequency domain). Figure 4 shows a characteristic cross-sectional image at $y = 3$ mm scanning position. The abscissa is scanning position x , and the ordinate is time. The signal amplitude is shown in grayscale, as captured by optical microphone in a B-scan.

The cross-sectional cut is performed over all three delaminations and the inclusion area (aluminum foils) (refer to Fig. 1c). The B-scan is shown in the *long* and *short time window*.

In Fig. 4 (above and below number 1), we can observe low-frequency, long-lasting natural oscillations of the delaminations, which have a relatively high amplitude. The recorded oscillation is a consequence of a complex mechanic behavior of a delamination. However, the shape of the signal for the compression and the extension phase of the delamination is the same, having the inverted sign—no amplitude hysteresis can be observed. Thus the presence of the non-linear mechanic oscillation of the delamination cannot be deduced from the recorded signal [29].

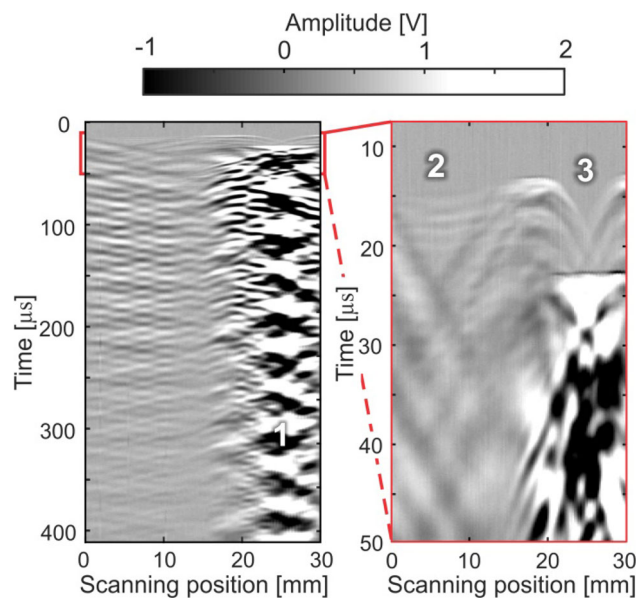


Fig. 5 B-scan at $x = 35$ mm scanning position. The cross-sectional cut goes over a delamination (located at number 2) and flat-bottom hole (located at number 3)

We can see at least two in-air reflections of the US between optical microphone and specimen plate (Fig. 4: thin high frequency lines above number 2). If we zoom into the *small time window* (before in-air reflections), we can distinguish in-plate US reflections (Fig. 4: white lines above number 3). These reflections are present only in the non-delaminated areas of the specimen. Therefore, they are a good indicator of the delamination in which the US of this frequency is strongly dissipated. The oscillations with a frequency approximately double of the TR are present at the delaminated area, which are due to the reflections of US on the delaminations and characteristically arrive before the back-side plate echo (first in-plane reflection). They have comparatively small amplitude and are thus hardly seen in Fig. 4 below number 4. The reflections from the inclusion defects cannot be significantly distinguished below number 5 in Fig. 4.

Figure 5 shows a B-scan at $x = 35$ mm scanning position. The cross-sectional cut is performed over the delamination and the flat-bottom hole (refer to Fig. 1c).

The remaining layer of the flat-bottom hole is strongly excited in its natural oscillations by the laser pulse. This can be observed in periodical changes of black and white color below and above number 1, where the pattern of the natural oscillation can be observed. Below the number 2, we can observe the lack of high-frequency in-plate reflections that is caused by the delamination. The arrival of the first high-frequency wave train is delayed at the flat-bottom-hole location because the US needs to travel the longer distance through air there (below number 3), comparing to the rest of the scanning area.

4.3 S-scans (B-scans in Frequency Domain)

Additional information can be obtained from the signal via a spectral analysis thereof. We thus applied the Fourier transform to a time signal for all of the scanning positions. As a result, we obtained a second 3-dimensional data matrix with the following axes: scan direction x , scan direction y , and frequency. Each matrix element is a relative amplitude value (referring to the maximal of the whole matrix) of certain frequency and at certain scanning location.

Figure 6 shows a cross-sectional image of scan data matrix in the frequency domain at $y = 3$ mm scanning position. Figure 6 is Fig. 4 converted to the frequency domain. Again, we analyzed the signal in two frequency ranges: TR-FR (Fig. 4 left) and STR-FR (Fig. 4 right). For the TR-FR analysis of the signal, we used the *small time window*, and the *long time window* for the STR-FR analysis. Therefore, the zoomed S-scan (Fig. 4 right) has a better frequency resolution than the full range (Fig. 4 left). To make higher-order resonances of the TR more apparent, the amplitude shown in grayscale at the left of Fig. 4 left was expressed relatively to the maximum value of TR-FR and not to the maximal value of the full frequency range. The data presentation is therefore more transparent than when using logarithmic grayscale values.

The LDR of the delaminations are clearly visible (frequency peaks above number 1 in Fig. 6) at 33 kHz, 58 kHz, 83 kHz, and 110 kHz. Different delaminations respond with different characteristic natural frequencies. The frequency spectrum can therefore be seen as the delamination's footprint. Further analysis of the delamination's LDR is performed in Fig. 8.

The TR is clearly visible at the delamination-free area (frequency peak at approximately 330 kHz above number 2 and 3 in Fig. 6). We can also observe higher-order resonances of TR (above and below number 2 and 3 in Fig. 6). The US velocity in aluminum is higher than in CFRP (parallel to fiber orientation). Therefore, the in-plate reflections in the area of the specimen with inclusions have slightly shorter periods than reflections in the full-CFRP portion of the specimen. The increase of TR frequency in the inclusion area is hardly distinguishable (frequency peak at approximately 360 kHz above number 3 in Fig. 6), however, it is significant enough to make the inclusions visible in an F-scan (Fig. 10a).

Figure 7 shows a cross-sectional image of the scan data matrix in frequency domain at $x = 35$ mm scanning position. Figure 7 is Fig. 5 converted to the frequency domain.

The flat-bottom hole in the specimen plate has a natural frequency at 25 kHz (Fig. 7, number 1). The higher intensity of the US is transmitted through the remaining thickness of the flat-bottom hole as compared to the full-thickness plate.

The LDR of the delamination has lower amplitude comparing to the LDR of the flat-bottom hole. They are located at number 2, but not visible in the grayscale range of Fig. 7.

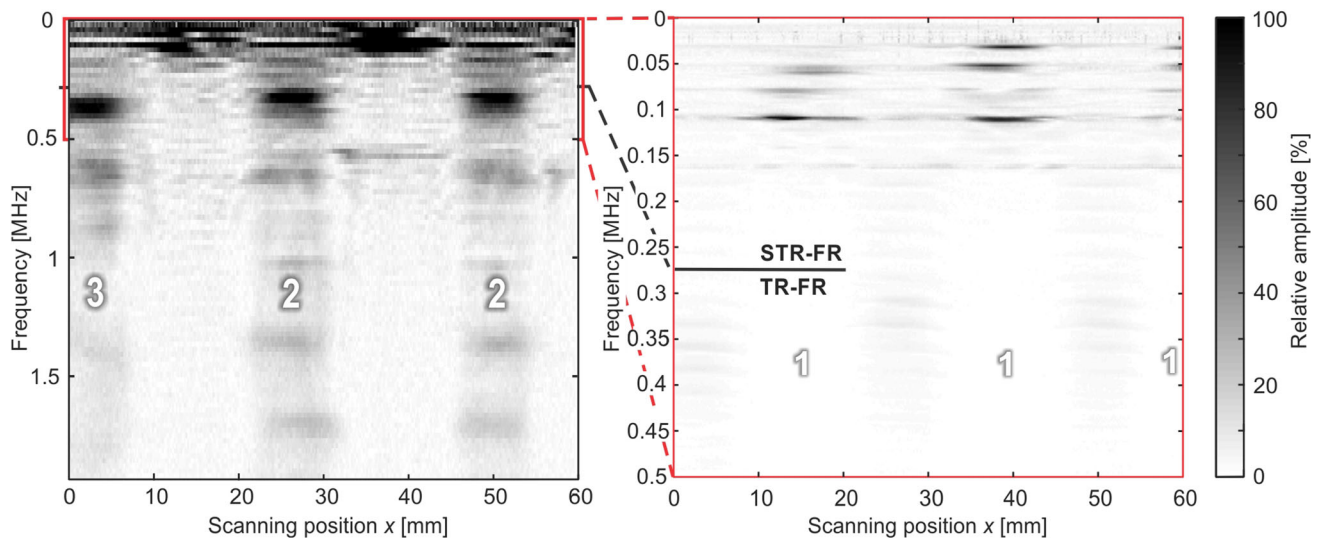


Fig. 6 S-scan (B-scan in frequency domain) at $y = 3$ mm scanning position. The cross-sectional cut goes over three delaminations (located at number 1) and inclusion (located at number 3)

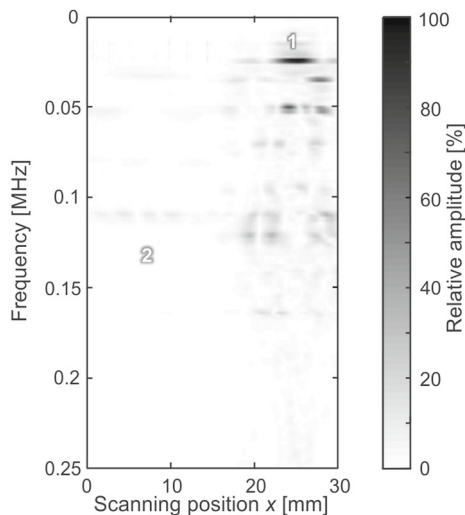


Fig. 7 S-scan (B-scan in frequency domain) at $x = 35$ mm scanning position. The cross-sectional cut goes over a delamination (located at number 2) and flat-bottom hole (located at number 1)

4.4 C-scans

We first analyzed the STR-FR which was of interest for the local resonance analysis of the features. Regarding C-scans, it must be specified how the amplitude value was obtained. Commonly, mean amplitude (or maximal amplitude) within the specified frequency interval or time window is coded in grayscale. If the frequency (or time) interval is comparatively small (e.g. below 5% of its mean value), specifying the mean value suffices.

Figure 8 shows C-scans obtained from the frequency domain. In this case, the 3-dimensional scan data matrix in

frequency domain is cut in the *scanning position*—*scanning position* plane (the remaining two orthogonal slice directions are S-scans in Figs. 6 and 7). For each C-scan, the frequency at which the cross-sectional image was obtained is explicitly labeled. Note that the amplitude value represents the average over the frequency discretization interval. The frequencies were chosen to fit the LDR frequency peaks of the flat-bottom hole and delaminations (frequency peaks above number 1 in Fig. 6 and below number 1 in Fig. 7). For all the scanning locations, the amplitude value is expressed relative to the maximal amplitude value of each respective C-scan.

At 25 kHz, we can observe the flat-bottom hole oscillating at its (0, 1) eigenmode (Fig. 8, number 1). The vibration of the delamination is a complex mechanical problem. It was researched on a numerical model in [29–31]. Some typical eigenmode shapes of the delamination are observable at their LDR frequencies in the Fig. 8. The two delaminations appear to oscillate at their (1, 1) eigenmode at different natural frequencies—33 kHz and 46 kHz (Fig. 8, number 2). The frequencies at which the delaminations oscillate at higher modes are similar for both delaminations. At 58 kHz, the amplitude shape of LDR reminds on (1, 2) (number 3), at 83 kHz on (1, 3) (number 4) and at 110 kHz on (1, 4) eigenmode (number 5).

We estimated the order of magnitude of the LDR frequencies of the delaminations and the flat-bottom hole. In the first approximation, the oscillations of the flat-bottom hole and delaminations can be modeled by the analytical solution for circular and rectangular plate, respectively [20, 32]. The following assumptions were made for this simplified model: the deformability of the damage is much higher than that of the undamaged plate—the clamped edge is used

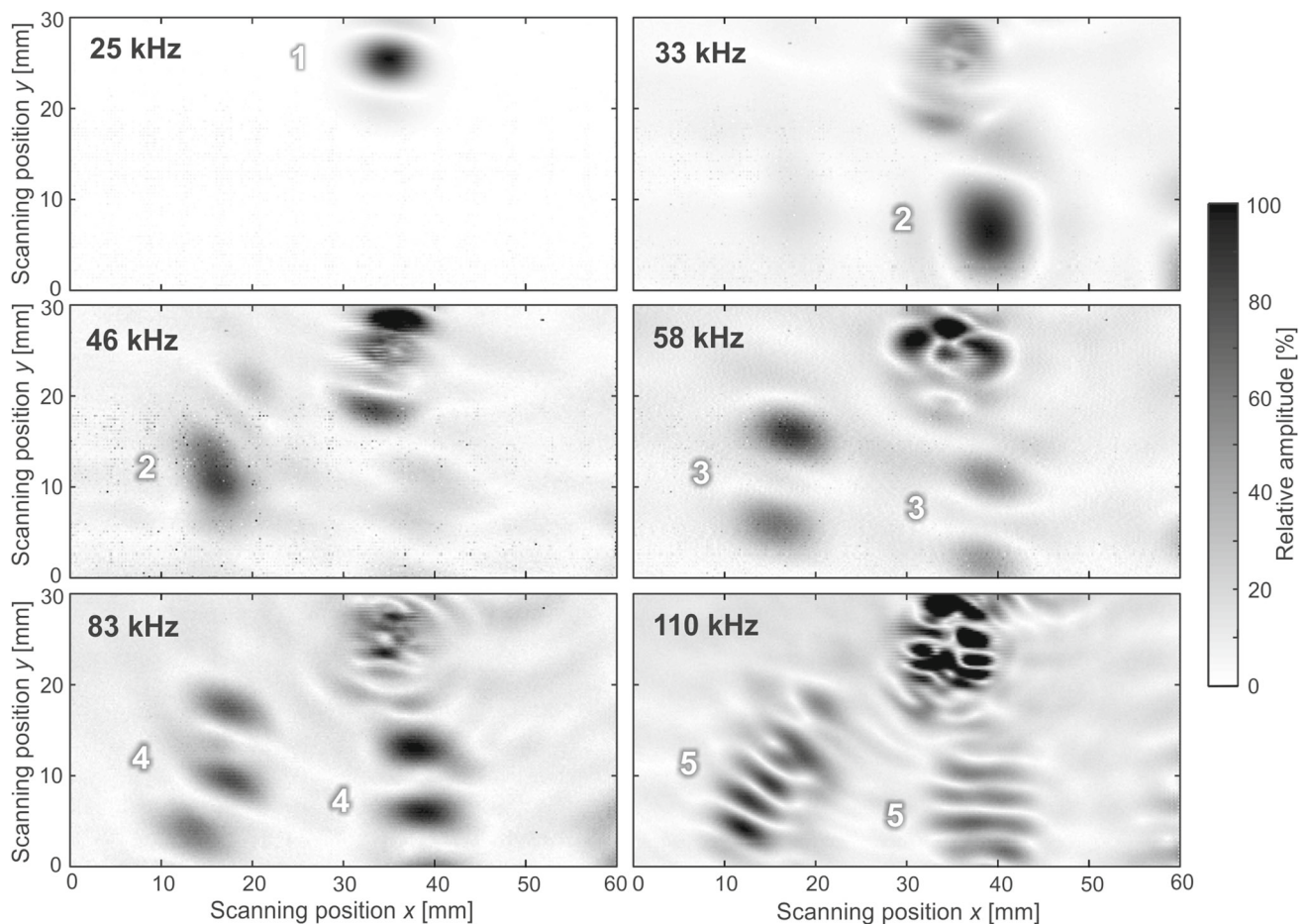


Fig. 8 C-scan at selected frequencies labeled in upper-left corner. Shapes that reminds on eigenmodes of flat-bottom hole (number 1) and delaminations (number 2–5) are visible

as the boundary condition; the composite material is homogeneous and isotropic with a Young's modulus of 68 GPa (mean value), Poisson's ratio of 0.3, and mass density of 1600 kg/m³ (values for the material used: T700/MTM57); for the delaminations, the interface of the disbanded laminates is mechanically decoupled and located in the middle of the plate thickness. Assuming these simplifications, the LDR frequencies can be calculated from the equations described in [32]. The first LDR frequency results in approximately 10 kHz for the flat-bottom hole and approximately 80 kHz for the delaminations.

The seventh C-scan is shown in Fig. 9, where the mean amplitude value of the US frequencies in TR-FR (between 264 kHz and 3 MHz) is coded in the grayscale. The upper frequency limit (3 MHz) was defined according to the optical microphone's sensitivity range. The US amplitude is expressed relative to the maximal value of all the scanning position, excluding the flat-bottom hole. The US amplitude in TR-FR is significantly higher there, because of the small thickness of the remaining layer under the hole (number 1 in

Fig. 9). This can be observed also in S-scan in Fig. 7 below number 1.

The TR-FR is highly sensitive with respect to delaminations. The TR amplitude peak, with its higher-order resonances, is strongly attenuated due to the detached fiber layers. Almost no US of this frequency range is transmitted through the delaminations (number 2 in Fig. 9). Furthermore, flat-bottom hole is clearly visible (number 1 in Fig. 9). Aluminum inclusions are not distinguishable.

4.5 F-scans

While the US amplitude in TR-FR is carrying the information about the attenuation level of US in specimen, it is the most suitable for the detection of features which deliver additional material-air interfaces (cracks, delaminations, kissing bonds, porosity, voids). In contrast, if the feature does not cause comprehensive impedance changes (i.e. order of magnitude), almost the same US intensity is transmitted through the feature as through the feature-free material. As a result, changes in mechanical properties of the material or inclusions

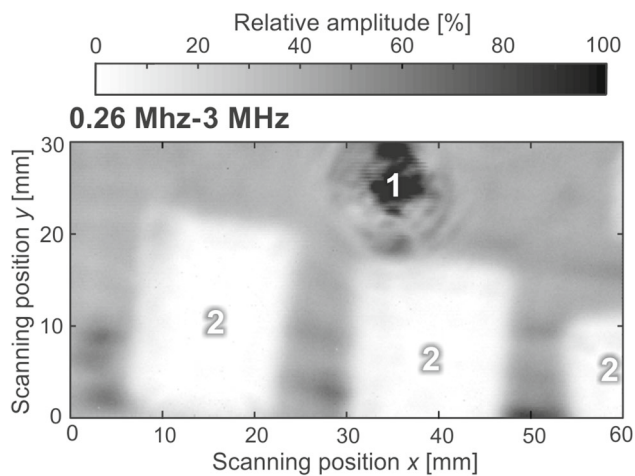


Fig. 9 C-scan with the mean amplitude value in the frequency interval 0.26–4 MHz coded in grayscale. Flat-bottom hole (number 1) and delaminations (number 2) are clearly visible. Aluminum inclusions are not distinguishable

of foreign material (impurities) cannot be detected. However, they have a significant influence on the local resonance of the specimen—on the TR and its higher-order resonances in the case of plates. On the other hand, we can also interpret it according to the wave theory: depending on the local mechanical properties of the plate, the US velocity locally changes, which can be seen in the change of the period of the in-plate reflections.

The US velocity (longitudinal waves) in aluminum is approximately 6300 m/s, which is a factor 2.3 larger than the specimen plate used in this experiment (approximately 2700 m/s perpendicularly to fiber orientation). For each of the CFRP layers (out of 15) which were exchanged by aluminum foil, the TR frequency increases by approximately 8.7% (1.3/15) from the initial TR frequency—i.e. 28.6 kHz for our specimen.

In the F-scan shown in Fig. 10, the frequency peak value of the local TR of the specimen plate is coded in grayscale for all the scanning positions. To visualize the aluminum inclusions, the first TR (a) and fourth higher harmonic (b) turned out to be the most suitable. This choice depends on the nature of this feature and on the experimental setup itself (the optical microphone's frequency range and its frequency dependent sensitivity). The frequency peak of the first TR is determined in the range of 310–370 kHz, and the fourth higher harmonic in the range of 1.32–1.44 MHz. Grayscale is expressed absolutely in separate bars.

In contrast to the C-scan, the F-scans reveal also the aluminum inclusion (number 1). It is possible to determine the area where at least one inclusion is located, but not the exact number of overlapping foils. The first TR exhibits a significant decrease in frequency at scanning positions y higher than 23 mm, where aluminum inclusions are located (num-

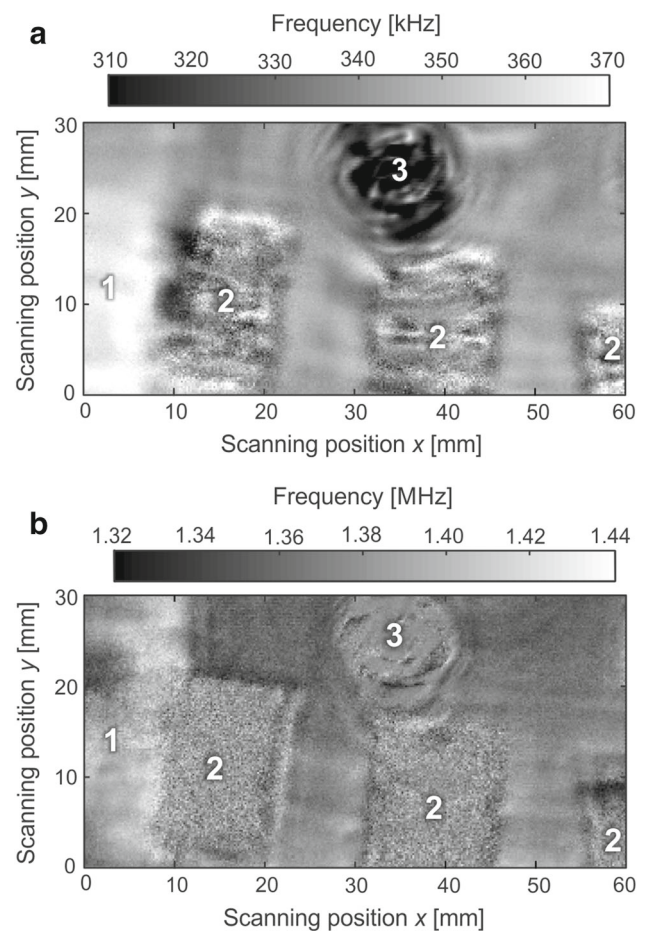


Fig. 10 F-scan of 0.31–0.37 MHz (a) and 1.32–1.44 MHz (b) frequency range. The frequency of first thickness resonance (a) and its fourth higher harmonic (b) is coded in grayscale

ber 1 in Fig. 10a). The frequency transition correlates with the horizontal borderline of one inclusion. The second (vertical) borderline cannot be clearly detected from the first TR frequency. The surface, where at least one inclusion is located, can be more easily determined from fourth higher harmonic of TR (Fig. 10b). The borderline is clear at the area with no delamination. In contrast, the intrusions cannot be detected, if they overlap with the delamination, because almost no US of TR-RF is transmitted through the specimen there. Therefore, the delaminations can be detected as the surfaces with higher noise level in Fig. 10 (number 2). Their boundaries can be determined comparatively well. Flat-bottom hole, which transmits high intensity of US in TR-FR range, is located at number 3.

5 Conclusions

We introduced a new US inspection and signal interpretation approach, which was given the name of LURS. It was initi-

ated by a novel experimental setup which is capable of the effective generation and detection of US ranging from several kHz to several MHz. We considered the full frequency range integrally by way of observing the local resonance in US spectrum.

The LURS can be described as consisting of the following steps:

- broadband local excitation and acquisition of the US for all the scanning positions,
- organizing the data in 3-dimensional data matrix and its conversion to frequency domain,
- investigation of data matrix by observing B- and S-scans and identification of the characteristic frequencies, which carry the information about the features of the specimen. Characteristic frequencies can either be a local resonance of the features/defects (STR-FR for plates) or local resonance of the specimen itself (TR-FR for plates). A parameter for visualizing the features can also be an amount of high frequency US components—this is complementary to classical ultrasonic inspection.
- visualization of the features, by plotting amplitude or frequency shift of characteristic frequencies in C- and F-scans,
- classification of the features according to its form and local resonance frequency.

In this work, we demonstrated LURS on a CFRP plate that included a flat-bottom hole, simulated delaminations and aluminum inclusions. It is possible to visualize all of these features through LURS. We determined the LDR of the flat-bottom hole and of simulated delaminations. We visualized the delaminations via the absence of high frequency components of US. We showed that aluminum inclusions effect TR and its fourth higher harmonic. This was visualized through the F-scans.

The advantages of LURS are the following. It makes the observation of local resonant behavior and ultrasonic wave propagation possible by performing a single measurement. The type and form of the feature can be classified. Since it is based on US, LURS is more highly sensitive to delaminations and other features that have a strong effect on mechanical properties of the specimen in comparison to radiography methods. Compared to classical US methods, LURS can be ad hoc more sensitive to certain features since it detects changes of local resonance behavior of the specimen which are strongly dependent on the local mechanical (geometrical, material etc.) properties. It is contact-free and allows relatively fast performance of a scan.

The disadvantages are that LURS—at this stage of development—requires manual analysis of the spectrum in order to determine characteristic information-carrying frequencies. Certain knowledge of the nature of single feature is required

for this purpose. LURS necessitates handling with higher data quantities (scan data matrix). Since LURS is US-based, it is less sensitive to aluminum inclusions than radiology methods. However, this can be seen also as an advantage, since it allows selective detection of features that affect the mechanical properties of the specimen (e.g., adhesive dis-bonds between aluminum and CFRP). The disadvantages are further associated with laser safety.

The goal of our future work is to develop a computer-based tool which will be able to resolve the local specimen's properties from the US spectrum obtained by means of LURS. In terms of reverse engineering, geometrical, material and quality condition properties of the specimen are to be obtained automatically. The characteristic information-carrying frequencies of the US spectrum can also be obtained by means of machine learning algorithms.

Acknowledgements Open Access funding provided by Projekt DEAL. The authors acknowledge Dr.-Ing. Otto and Karla Likar foundation for the financial support, and XARION Laser Acoustics for providing the experimental equipment.

Open Access This article is licensed under a Creative Commons Attribution 4.0 International License, which permits use, sharing, adaptation, distribution and reproduction in any medium or format, as long as you give appropriate credit to the original author(s) and the source, provide a link to the Creative Commons licence, and indicate if changes were made. The images or other third party material in this article are included in the article's Creative Commons licence, unless indicated otherwise in a credit line to the material. If material is not included in the article's Creative Commons licence and your intended use is not permitted by statutory regulation or exceeds the permitted use, you will need to obtain permission directly from the copyright holder. To view a copy of this licence, visit <http://creativecommons.org/licenses/by/4.0/>.

References

1. Migliori, A., Sarrao, J.L.: Resonant Ultrasound Spectroscopy : Applications to physics, Materials Measurements, and Nondestructive Evaluation. Wiley, New York (1997)
2. Zadler, B.J., Le Rousseau, J.H.L., Scales, J.A., Smith, M.L.: Resonant Ultrasound Spectroscopy: theory and application. *Geophys. J. Int.* **156**(1), 154–169 (2004). <https://doi.org/10.1111/j.1365-246X.2004.02093.x>
3. Maynard, J.: Resonant ultrasound spectroscopy. *Phys. Today* **49**(1), 26–31 (1996). <https://doi.org/10.1063/1.881483>
4. Jüngert, A., Grosse, C., Krüger, M.: Local acoustic resonance spectroscopy (LARS) for glass fiber-reinforced polymer applications. *J Nondestruct Eval* **33**(1), 23–33 (2014). <https://doi.org/10.1007/s10921-013-0199-3>
5. Jatzlau, P., Müller, M., Grosse, C.U.: Identification of flawed CFRP samples using local acoustic resonance spectroscopy (LARS). In: WCNDT, 19th World Conference on Non-destructive Testing, 2016
6. Jatzlau, P., Grosse, C.U.: Local acoustic resonance spectroscopy: an escalation approach for fast non-destructive testing. In: 10th International Symposium on NDT in Aerospace (2018)
7. Grosse, C.U., Jüngert, A., Jatzlau, P.: Local Acoustic Resonance Spectroscopy, pp. 1–24. Handbook of Advanced Non-Destructive Evaluation. Springer, Berlin (2018)

8. EN ISO 5577:2017. Non-destructive testing—Ultrasonic testing—Vocabulary
9. Brown, A.F.: Materials testing by ultrasonic spectroscopy. *Ultrasonics* **11**(5), 202–210 (1973). [https://doi.org/10.1016/0041-624X\(73\)90231-X](https://doi.org/10.1016/0041-624X(73)90231-X)
10. Cousins, R.R., Markham, M.F.: The use of ultrasonic spectroscopy in the location of delaminations in fibre-reinforced polymers. *Composites* **8**(3), 145–152 (1977). [https://doi.org/10.1016/0010-4361\(77\)90008-8](https://doi.org/10.1016/0010-4361(77)90008-8)
11. Fitting, D.W., Adler, L.: Applications of ultrasonic spectroscopy to materials evaluation. In: Fitting, D.W., Adler, L. (eds.) *Ultrasonic Spectral Analysis for Nondestructive Evaluation*, pp. 93–137. Springer, Boston (1981)
12. Wright, W.M.D., Hutchins, D.A.: Air-coupled ultrasonic testing of metals using broadband pulses in through-transmission. *Ultrasonics* **37**(1), 19–22 (1999). [https://doi.org/10.1016/S0041-624X\(98\)00034-1](https://doi.org/10.1016/S0041-624X(98)00034-1)
13. Schindel, D.W., Hutchins, D.A.: Through-thickness characterization of solids by wideband air-coupled ultrasound. *Ultrasonics* **33**(1), 11–17 (1995). [https://doi.org/10.1016/0041-624X\(95\)00011-Q](https://doi.org/10.1016/0041-624X(95)00011-Q)
14. Scruby, C.B., Drain, L.E.: *Laser Ultrasonics: Techniques and Applications*. A. Hilger, Philadelphia (1990)
15. Podymova, N.B., Karabutov, A.A.: Broadband laser-ultrasonic spectroscopy for quantitative characterization of porosity effect on acoustic attenuation and phase velocity in CFRP laminates. *J. Nondestruct. Eval.* **33**(1), 141–151 (2014). <https://doi.org/10.1007/s10921-013-0210-z>
16. Wright, W.M.D., Hutchins, D.A., Gachagan, A., Hayward, G.: Polymer composite material characterisation using a laser/air-transducer system. *Ultrasonics* **34**(8), 825–833 (1996). [https://doi.org/10.1016/S0041-624X\(96\)00083-2](https://doi.org/10.1016/S0041-624X(96)00083-2)
17. Diot, G., Koudri-David, A., Walaszek, H., Guégan, S., Flifla, J.: Non-destructive testing of porosity in laser welded aluminium alloy plates: laser ultrasound and frequency-bandwidth analysis. *J. Nondestruct. Eval.* **32**(4), 354–361 (2013). <https://doi.org/10.1007/s10921-013-0189-5>
18. Fischer, B., Sarasini, F., Tirillò, J., Touchard, F., Chocinski-Arnault, L., Mellier, D., Panzer, N., Sommerhuber, R., Russo, P., Papa, I., Lopresto, V., Ecault, R.: Impact damage assessment in bio-composites by micro-CT and innovative air-coupled detection of laser-generated ultrasound. *Compos. Struct.* **210**, 922–931 (2019). <https://doi.org/10.1016/j.compstruct.2018.12.013>
19. Solodov, I., Dillenz, A., Kreutzbruck, M.: A new mode of acoustic NDT via resonant air-coupled emission. *J. Appl. Phys.* **121**(24), 245101 (2017). <https://doi.org/10.1063/1.4985286>
20. Solodov, I., Bai, J., Busse, G.: Resonant ultrasound spectroscopy of defects: case study of flat-bottomed holes. *J. Appl. Phys.* **113**(22), 223512 (2013). <https://doi.org/10.1063/1.4810926>
21. Solodov, I., Rahammer, M., Gulnizkij, N., Kreutzbruck, M.: Non-contact sonic NDE and defect imaging via local defect resonance. *J. Nondestruct. Eval.* **35**(3), 48 (2016). <https://doi.org/10.1007/s10921-016-0364-6>
22. Segers, J., Kersemans, M., Hedayatrasa, S., Calderon, J., Van Paepegem, W.: Towards in-plane local defect resonance for non-destructive testing of polymers and composites. *NDT E. Int.* **98**, 130–133 (2018). <https://doi.org/10.1016/j.ndteint.2018.05.007>
23. Hettler, J., Tabatabaeipour, M., Delrue, S., Van Den Abeele, K.: Detection and characterization of local defect resonances arising from delaminations and flat bottom holes. *J. Nondestruct. Eval.* **36**(1), 2 (2016). <https://doi.org/10.1007/s10921-016-0380-6>
24. Perterer, M.: Schadensidentifikation und -bewertung von CFK-Bauteilen mittels phasenmodulierter Thermographie. Dissertation, Technical University of Munich (2012)
25. Fischer, B.: Optical microphone hears ultrasound. *Nat Photonics* **10**, 356–358 (2016). <https://doi.org/10.1038/nphoton.2016.95>
26. Preisser, S., Rohringer, W., Liu, M., Kollmann, C., Zotter, S., Fischer, B., Drexler, W.: All-optical highly sensitive akinetic sensor for ultrasound detection and photoacoustic imaging. *Biomed. Opt. Express* **7**(10), 4171–4186 (2016). <https://doi.org/10.1364/BOE.7.004171>
27. Preisser, S., Fischer, B., Panzer, N.: Listening to ultrasound with a laser. *Opt. Photon.* **12**(5), 22–25 (2017). <https://doi.org/10.1002/opph.201700031>
28. Rus, J., Fischer, B., Grosse, C.U.: Photoacoustic inspection of CFRP using an optical microphone. *Proc. SPIE Opt. Meas. Syst. Ind. Inspect.* **XI**, 1105622 (2019). <https://doi.org/10.1117/12.2525021>
29. Solodov, I., Döring, D., Busse, G.: New opportunities for NDT using non-linear interaction of elastic waves with defects. *J. Mech. Eng.* (2011). <https://doi.org/10.1016/10.5545/sv-jme.2010.168>
30. Della, C.N., Shu, D.: Vibration of delaminated composite laminates: a review. *Appl. Mech. Rev.* **60**(1), 1–20 (2007). <https://doi.org/10.1016/10.1115/1.2375141>
31. Sarens, B., Verstraeten, B., Glorieux, C., Kalogiannakis, G., Hemelrijck, D.V.: Investigation of contact acoustic nonlinearity in delaminations by shearographic imaging, laser Doppler vibrometric scanning and finite difference modeling. *IEEE Trans. Ultrason. Ferroelectr. Freq. Control* **57**(6), 1383–1395 (2010). <https://doi.org/10.1109/TUFFC.2010.1557>
32. Blevins, R.D.: *Formulas for Natural Frequency and Mode Shape*. Van Nostrand Reinhold Company, New York (1979)

Publisher's Note Springer Nature remains neutral with regard to jurisdictional claims in published maps and institutional affiliations.

Article #2: Qualitative Comparison of Non-Destructive Methods for Inspection of Carbon Fiber-Reinforced Polymer Laminates

Authors: Janez Rus, Alex Gustschin, Hubert Mooshofer, Jan-Carl Grager, Klaas Bente, Mate Gaal, Franz Pfeiffer, Christian U. Grosse

Title: Qualitative comparison of non-destructive methods for inspection of carbon fiber-reinforced polymer laminates

Journal: Journal of Composite Materials

Publisher: SAGE Journals

First submission to the publisher: 11 February 2020

Accepted: 8 May 2020

Available online: 18 June 2020

Issue date: November 2020

Volume: 57

Issue: 27

Pages: 4325-4337

DOI: 10.1177/0021998320931162

Reprint Permissions

Open Access. This article is distributed under the terms of the Creative Commons Attribution 4.0 License, which permits any use, reproduction and distribution of the work without further permission provided the original work is attributed as specified on the SAGE and Open Access pages.


Qualitative comparison of non-destructive methods for inspection of carbon fiber-reinforced polymer laminates

Journal of Composite Materials
2020, Vol. 54(27) 4325–4337
© The Author(s) 2020



Article reuse guidelines:
sagepub.com/journals-permissions
DOI: 10.1177/0021998320931162
journals.sagepub.com/home/jcm



Janez Rus¹ , Alex Gustschin², Hubert Mooshofer³,
Jan-Carl Grager¹, Klaas Bente⁴, Mate Gaal⁴, Franz Pfeiffer^{2,5}
and Christian U. Grosse¹

Abstract

In the rapidly expanding composite industry, novel inspection methods have been developed in recent years. Particularly promising for air-coupled testing are cellular polypropylene transducers which offer better impedance matching to air than piezoelectric transducers. Furthermore, broadband transmitters (laser-induced ultrasound and thermoacoustic emitters) and receivers (optical microphones) have opened a completely new chapter for advanced contact-free ultrasound inspection. X-ray dark-field radiography offers a different approach to detect porosity and microcracks, employing small angle X-ray scattering. These innovative ultrasonic and radiographic alternatives were evaluated in comparison with well-established inspection techniques. We applied thirteen different non-destructive methods to inspect the same specimen (a carbon fiber-reinforced polymer laminate with induced impact damage): air-coupled ultrasound testing (using piezoelectric transducers, broadband optical microphones, cellular polypropylene transducers, and a thermoacoustic emitter), laser-induced ultrasound testing, ultrasonic immersion testing, phased array ultrasonic testing, optically excited lock-in thermography, and X-ray radiography (projectional absorption and dark-field, tomosynthesis, and micro-computed tomography). The inspection methods were qualitatively characterized by comparing the scan results. The conclusions are advantageous for a decision on the optimal method for certain testing constraints.

Keywords

Carbon fiber-reinforced polymer, air-coupled ultrasound, optically excited lock-in thermography, X-ray micro-computed tomography, X-ray dark-field radiography

Introduction

Generally, reconstructed images obtained by inspection methods deliver only a more or less accurate approximation of the reality. Each non-destructive testing method has its own characteristic footprint, which alters information about the observed feature – it acts as a filter function. By comparing results of different methods, it is possible to distinguish between filter effects and the true conditions of the material and defects. In this paper, we aim to isolate both in order to investigate which of the imaged features are only imaging artifacts and which deliver beneficial information for evaluation. More appropriate conclusions about the inspected object can thus be made. Furthermore, we emphasize that the combination of

¹Chair of Non-Destructive Testing, Centre for Building Materials, Technical University of Munich, Germany

²Chair of Biomedical Physics, Munich School of Bioengineering, Technical University of Munich, Germany

³Siemens AG, Corporate Technology, Germany

⁴8.4 Acoustic and Electromagnetic Methods, Federal Institute for Materials Research and Testing (Bundesanstalt für Materialforschung und -prüfung BAM), Germany

⁵Department of Diagnostic and Interventional Radiology, School of Medicine (Klinikum rechts der Isar), Technical University of Munich, Germany

Corresponding author:

Janez Rus, Technical University of Munich, Centre for Building Materials, Chair of Non-Destructive Testing, Franz-Langinger-Strasse 10, 81245 Munich, Germany.

Email: janez.rus@tum.de

different imaging methods deliver additional information about the specimen that cannot be obtained by a single method.

There are few recent publications dealing with a similar comparison. Grosse et al.¹ include results from air-coupled ultrasound (ACU), immersion testing and optically excited lock-in thermography (OLT) as applied to impact damage and flat-bottom holes. Ultrasound (US) immersion testing and X-ray micro-computed tomography (μ CT) were applied and compared to inspect impact damages in carbon fiber-reinforced polymer (CFRP) in Ehrlich et al.² The damaged area determined by the μ CT was significantly larger than the one obtained by US testing. Maierhofer et al.³ compared the images obtained by different arrangements of passive (immediate after the impact) and active thermography with the C-scans of contact phased array ultrasonic testing (PAUT) and ACU. The specimen was an impacted CFRP plate. Abou-Khousa et al.⁴ compared X-ray computed tomography, near field millimeter wave, shearography and immersion testing US methods on honeycomb composite specimens. Their results show an advantage of X-ray computed tomography in lateral resolution compared to other methods. Wang et al.⁵ compared X-ray computed tomography, terahertz imaging and immersion US testing on glass fiber-reinforced polymer composites with delaminations. They demonstrated that for the specimen tested, terahertz imaging has higher contrast than X-ray computed tomography and higher lateral and axial resolution than immersion US testing. Schumacher et al.⁶ applied US, thermography, eddy current, and X-ray methods (radiography, laminography and μ CT) to CFRP laminate samples. They conclude that each of the methods can contribute different information to overall evaluation of the specimen. Hakim et al.⁷ compared different variations of thermography testing methods on CFRP samples. Papa et al.⁸ compared the results of electronic speckle pattern interferometry and PAUT on basalt composite laminates with induced low-velocity impact damages. Grager et al.⁹ used various ACU testing setups to inspect CFRP samples with flat-bottom holes, foam core CFRP sandwich and an impact specimen that is used in the present study. We therefore included their results in this work to make a side-by-side comparison to other non-destructive testing (NDT) methods. Their results show the advantage of the broadband optical microphone as an alternative to the piezoelectric US receivers in its good spatial scan resolution. However, in contrary to our results, which were also achieved with a newer and more sensitive version of the optical microphone, they described the problems with lower sensitivity and scan artifacts at the damage boundary.

Further description of this effect is given in Results of the comparison and discussion section.

X-ray dark-field radiography is a relatively new method that uses spatial intensity modulation on the micron scale to generate a contrast based on small angle X-ray scattering.¹⁰ It is sensitive to electron density modulations on the micron scale and is suitable for detection of porosity, microcracks¹¹ and fiber orientation.¹² Recently, some progress was reported in terms of field of view and scanning speed¹³ making this method of interest for an evaluation and comparison with other approaches.

In this work, we compare a broader spectrum of inspection methods than in the previous research being described in the literature. Furthermore, we include recently developed, more efficient, non-contact techniques using broadband US excitation and detection. By setting them side-by-side with the conventional and established methods,^{14,15} their potentials can be evaluated. Additionally, we compare various radiographic methods on the same example.

Piezoelectric and cellular polypropylene (cPP) transmitter, thermoacoustic emitter (TAE), and laser pulse were used as contact-free US sources. Piezoelectric and cPP receiver and different versions of broadband optical microphones were used for US detection in air in through-transmission setups. Other methods that are suitable for impact damage inspection in monolithic CFRP materials are also used in this study, namely, PAUT, immersion testing, OLT, and X-ray radiography methods (projectional absorption and dark-field, tomosynthesis and μ CT). The purpose of our study is to get a broader overview of this extended group of test methods for CFRP plate inspection. Evaluating the results delivered by various methods deepens our understanding of their shortcomings and advantages. Hence better decisions can be made for a specific inspection task between the different alternatives.

Specimen description

The measurements, made on the same specimen, allowed us to perform a relevant comparison. It was a monolithic CFRP laminate with dimensions of 150 mm \times 100 mm and 2.1-mm thickness. The scan area is indicated by the white frame in Figure 1. The material was composed of carbon fibers, glass fibers (2% of total fiber volume) and an epoxy resin matrix. The fabrication method was resin transfer molding and the orientation of the fiber layers was $+45^\circ/-45^\circ/0^\circ/-45^\circ/+45^\circ$.

The specimen was damaged by a 15-J-impactor according to ISO 18352^{1,16} in a drop-weight test. The impacted side will be labeled as the front side throughout this publication. The impact location was centered at the coordinates (30 mm, 30 mm) according to the

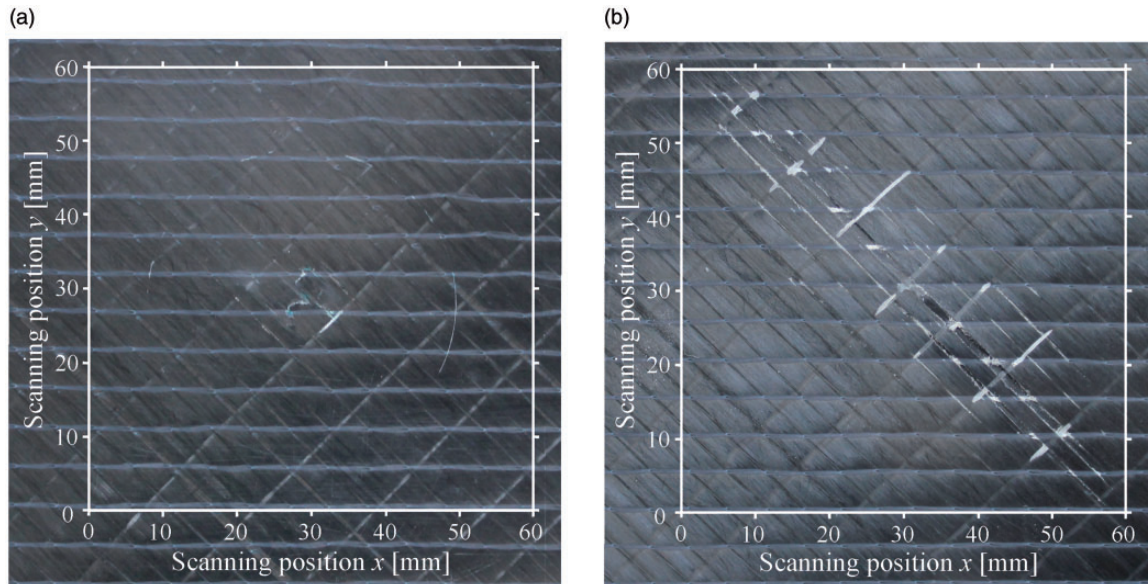


Figure 1. Front (a) and back (b) side of the specimen plate. The white frame indicates the scanned area.

scan coordinate system depicted in Figure 1. The diameter of the hemispherical impactor was 15.75 mm.

Impact damage is a feature that is frequently inspected in CFRP – a common material used in aerospace and lightweight engineering. Due to its high practical relevance and its complex defect shape, it is an optimal feature to compare different NDT methods. It can be described as consisting of chaotically distributed median and lateral cracks and overlaying delaminations of different sizes and shapes.

We chose impact damage to compare the inspection methods for two reasons. Firstly, it is practically relevant: impact is one of the most common causes of damage which can emerge either during production (drop/impact of the tools) or during the utilization of the investigated object. Secondly, it has a complex defect shape, which can be described as consisting of chaotically distributed median and lateral (closed and open) cracks and overlaying delaminations of different sizes and shapes. Capability of the inspection methods to detect the specific details of the defect shape can thus be evaluated. CFRP is a common material used in aerospace and lightweight engineering, where meeting the adequate quality standards is of high importance. Impact damage significantly alters the macroscopic material properties of the CFRP structures, which need to be regularly inspected when used for safety-sensitive applications.

Methods description

In the following subchapters, a brief description is given of the test methods selected for comparison.

Experimental equipment is identified together with the scan parameters. Separately, we explain how each of the C-scans was obtained. All of the ACU testing methods were conducted in classical through-transmission configuration with the US emitter placed on the front side of the specimen. The US excitation voltage was in a unipolar square shape. The number of pulses is labeled separately for each of the ACU method. Unless otherwise stated, no data averaging was applied.

Air coupled ultrasound: Piezoelectric transducers and optical microphones

Four scans were made using different piezoelectric transmitter and receiver (piezoelectric, optical microphone) combinations (Figure 2(a) to (e)).^{9,17–20} Individual experimental setups are described in separate subsections.

The Eta100, Eta250 and Eta450 are versions of optical microphones produced by Xarion Laser Acoustics. Their sensitivity (0.35 mV/Pa, 10 mV/Pa and 100 mV/Pa at 1 kHz) increases and their self-noise (1.5 mPa, 50 μ Pa at 1 kHz, and 5 μ Pa at 500 kHz) decreases (measured at bandwidth of 1 Hz) with a higher version number, as specified by the manufacturer. Optical microphones are able to detect sound waves without any moving parts.^{21,22} They therefore have a significantly broader frequency range (from less than kHz to several MHz) compared to conventional air-coupled US sensors. Detection via Fabry-Pérot interferometer (etalon) eliminates one air-solid interface in the measurement configuration. The diameter of the

laser beam is approximately 0.2 mm and the length of the etalon 2 mm. This results in the small aperture of the optical microphones, which enables a higher spatial resolution compared to conventional piezoelectric receivers.

Emitter: Piezoelectric transducer 200 kHz – receiver: Piezoelectric transducer 200 kHz. A pair of focused piezoelectric transducers AirTech 200 from Hillger NDT with 200 kHz nominal frequency and bandwidth of 21 kHz (-6 dB) was used.^{9,20} The diameters of their oscillators were 11.1 mm, their near-field length 18 mm, and the diameter of their soundfield in focus 3 mm (-6 dB). Sensitivity (transfer ratio in air) of the transducer pair was -33 dB. 10 pulses with amplitude of 142 V were excited by the USPC AirTech 4000 (Hillger NDT) electronics. Gain at reception was 48 dB. Scanning spatial resolution was set to 0.1 mm. Signals were filtered using an IIR-band-pass filter (190 kHz–210 kHz, of 8th order). C-scans were obtained by plotting the maximum amplitude value within the time window of the burst signal length (Figure 2(a)).

Emitter: Piezoelectric transducer 200 kHz – receiver: Eta100 optical microphone. The same AirTech 200 transducer as described previously was used as the US source.¹⁹ On the receiver side, the first version of the optical microphone: Eta100 prototype was used to capture the US. 8 pulses with amplitude of 200 V were excited by the USPC AirTech 4000 (Hillger NDT) electronics. Digital gain at reception was 20 dB. The receiver was located 2 cm away from the back side of the specimen. C-scans were obtained by plotting the maximum amplitude value of the captured burst signal (Figure 2(b)).

Emitter: Piezoelectric transducer 200 kHz – receiver: Eta250 optical microphone. The same AirTech 200 transducer was used as US source.^{9,20} On the receiver side, an Eta250 optical microphone was used to capture the US with 8-mm air gap to the specimen. The scanning spatial resolution was set to 0.1 mm. Signals at each scan position were filtered with an IIR-band-pass filter (190 kHz–210 kHz, of 8th order). 10 pulses with amplitude of 200 V were excited by the USPC AirTech 4000 (Hillger NDT) electronics. Digital gain at reception was 5.7 dB. The typical burst signal length was 100 μ s. C-scans were obtained by plotting the maximum amplitude value within the 20 μ s (Figure 2(c)) and 60 μ s (Figure 2(d)) time window, starting with the first break of the signal.

Emitter: Piezoelectric transducer 400 kHz – receiver: Eta450 optical microphone prototype. Focused piezoelectric transducer Sonoair CF 400 from Sonotec with nominal frequency of 400 kHz and bandwidth of 25 kHz (-6 dB, as

measured by Eta450 optical microphone) was used as a US source.¹⁸ The diameter of its oscillator was 20 mm, its near-field length 5 cm, and the diameter of its soundfield in focus 4 mm (-6 dB). Sensitivity (transfer ratio in air) of the transducer pair was -31 dB, as measured by the manufacturer. 8 pulses with amplitude of 400 V were excited by the Sonotec electronics. Gain at reception was 20 dB. On the receiver side, a prototype of the Eta450 was used. Specimen to microphone distance was set to 12 mm and the scanning grid size to 0.25 mm. The signal was filtered with a band-pass filter (Butterworth 350 kHz–450 kHz). To obtain the C-scans, the peak amplitude value (at nominal frequency of the US source) was plotted in greyscale (Figure 2 (e)).

Air coupled ultrasound: Cellular polypropylene transducers (cPP) and Eta250 optical microphone

cPP has significantly lower acoustic impedance than conventional piezoelectric ceramics.^{9,23} The impedance match to air is improved by flat voids constructed within the cPP. Consequently, cPP transducers are more efficient at US generation and reception in air. That was the motivation for choosing it for the construction of air-coupled transducers for non-destructive testing.²³ Transmission of some wooden samples has shown that the signal-to-noise ratio of ferroelectret cPP transducers is about 6 dB higher than of commercially available transducers.²⁴ Sensitivity of the in-house cPP receivers has not yet been measured, but can be calculated approximately as shown in Gaal et al.²³ It amounts around 2.5 mV/Pa for transducers at 250 kHz and 3.9 mV/Pa for transducers around 80 kHz. We have measured sound pressure level of 146 dB (rel. to 20 μ Pa) in the focus of a similar transmitter (250 kHz middle frequency, 19 mm aperture and 50 mm focusing radius) as used in our experiment.

Another focused cPP transmitter with a peak frequency of 247 kHz, near-field length 6.5 cm and aperture size of 19 mm was used as a US source. A focused cPP receiver with near-field length 2.5 cm, aperture size of 11 mm and a peak frequency of 280 kHz was located at the opposite side of the specimen plate. Both transducers had a bandwidth of 20% (-6 dB) and the diameter of their soundfield in focus 2.5 mm (-6 dB).²⁵ The corresponding C-scan results are shown in Figure 2(f).

For a second cPP-experiment, the emitter was replaced with one having a lower peak frequency of 127 kHz and a bandwidth of about 16%. It was unfocused and had a soundfield diameter (-6 dB) of approximately 6 mm. The reason for this was that at the original testing frequency (247 kHz), the received US pressure level was too low to be detected by the Eta250 optical microphone. The Eta250 signal was

band-pass filtered (105 kHz–145 kHz; of 8. order IIR). The C-scan results are shown in Figure 2(g). The electronic device used for both cPP transmitters was USPC AirTech 4000 (Hillger NDT). Additionally, the transmitters included an electrical matching network transforming the incoming 140 V to 1.8 kV to generate a double pulse for 247 kHz cPP transmitter and 5 pulses for 127 kHz cPP transmitter. The maximum amplitude within the time window of the burst signal is coded in greyscale for both experiments with cPP.

Air coupled ultrasound: Thermoacoustic emitter (TAE) and Eta450 optical microphone

A TAE generates US directly in air by an increase in the air's internal energy through heat.²⁶ In comparison to conventional resonant transducers, TAEs induce significantly shorter pulses – typically around 1 μ s. Consequently, TAEs have a broader frequency range, which potentially allows for a broadband spectral analysis of the testing specimen. Typically, US is excited by a short-time (μ s) electrical discharge over a thin conductive film, applied on a carrier substrate.

For the CFRP impact specimen, a TAE with a spherically curved glass substrate with a 200 nm indium tin oxide film was used.²⁷ The glass was curved with a radius of 92.5 mm to achieve acoustic focusing. A concentric electrode design caused a radial current flow. The thermoacoustically active indium tin oxide area had an inner radius of 10 mm and an outer radius of 26 mm. The excitation electronics consisted of the USPC 4000 Airtech (Hillger NDT), a voltage divider, an Agilent 33500B (Keysight Technologies) arbitrary waveform generator (AWG) and an in-house power amplifier.

The spatial scan resolution was 0.15 mm, the TAE excitation voltage 375 V, the peak power was 18 kW and the width of a single pulse was 2 μ s. The short pulse emitted by TAE was comparatively broadband: 742 kHz (-6 dB) with the center frequency at 410 kHz. At this frequency the sound pressure level was approximately 115 dB (ref. to 20 μ Pa). An Eta450 optical microphone was used as a receiver on the opposite side of the specimen. The signal was averaged 3 times. The difference between maximum and minimum amplitude value in the time window of the pulse width was plotted to generate the C-scan (Figure 2(h)).

Laser induced ultrasound in combination with the Eta450 optical microphone

Nd-YAG frequency-doubled, q-switched pulse laser with a wavelength of 532 nm (green light) was used to generate the US waves on the front side of the specimen.²⁸ The laser beam diameter was 8 mm (95%

intensity level). The shock wave was induced in the thermoelastic regime (no ablation). The laser source was part of the US excitation system provided by Xarion Laser Acoustics. The US was captured on the back side of the specimen plate using the Eta450. When scanning, the optical microphone was located approx. 4 mm away from the specimen. The setup was the same as used for the local ultrasonic resonance spectroscopy experiment described in Rus and Grosse.²⁹

The increment length of the scan was 0.2 mm and the scanning speed 4 mm/s. To obtain the C-scan, the mean amplitude of the captured signal in a frequency domain between 500 kHz and 4 MHz was coded in greyscale (Figure 2(i)).

Immersion ultrasonic testing

For immersion tests, the US testing system USPC 3040S DAC from Hillger NDT was used with a H10MP15 focused probe from GE Sensing & Inspection Technologies GmbH.¹⁶ It has a relative bandwidth of more than 80%, a nominal frequency of 10 MHz and a focal length of 15 mm in water. The transducer diameter was 5.0 mm. The scanning spatial resolution was 0.48 mm. The specimen was not degassed before being immersed in water.

C-scans were obtained by plotting the maximum amplitude value in a specific time window. For Figure 2(j), this window was set on the US echo from the back side of the specimen; for Figure 2(k), this window was set on the US echo from the reflector located on the opposite side of the specimen in the water, according to the US source (double through transmission technique).

Phased array ultrasonic testing (PAUT)

An Olympus OmniScan MX2 with 5L64-A2 phased array contact sensor was used in experiment.³⁰ It is a 5 MHz linear array comprising 64 piezoelectric elements with total aperture length of 38 mm. A C-scan was generated while sweeping the sensor head perpendicularly to the array orientation with the maximum speed of 15.5 mm/s. The sensor head location was specified by a wheel displacement encoder. The sensor head was directly in contact with the front side of the specimen. Water was used as a couplant. The scan resolution was 0.17 mm in sweep direction and 0.6 mm in array element direction. The amplitude of the backwall echo is shown in Figure 2(l).

Optically excited lock-in thermography (OLT)

The infrared camera used in this setup was IRCAM Equus 327k SM PRO.¹⁶ It has a spectral range between 1.5 μ m and 5 μ m wavelengths with the resolution of 640

Pixel \times 512 Pixel. A wide-angle lens with a focal length of 28 mm was used for the tests. For external optical excitation, a PAR-64 Profi Floorspot halogen lamp emitter with the maximum power of 1,000 W was used together with a ESG 570 F signal generator from Edevis GmbH. The camera and the lamp were located on the same side of the specimen. The lock-in frequency was set to 0.05 Hz. In Figure 3, the phase shift between the incident and reflected wave is coded in greyscale. The phase range was chosen in a range in which the damage is most visible.

X-ray radiography methods

Projectional absorption radiography and tomosynthesis. A tomosynthesis scan was performed using a GE Phoenix v|tome|x S system operating the microfocus transmission X-ray tube at an acceleration voltage of 30 kV and a current of 500 μ A. The sample was mounted exactly between the source and detector (1,000 \times 1,000 pixel) resulting in a magnification factor of two, an effective pixel size of 100 μ m and a field of view of 10 cm \times 10 cm. 100 projections were captured in the $\pm 20^\circ$ range with 2 s exposure time each. A projection perpendicular to the plate surface is shown (inverted, normalized transmission) in Figure 4 (a). The tomosynthesis was reconstructed by a standard filtered back-projection using the same software as described below for μ CT. The greyscale was windowed respective to the full range of the filtered back-projection to make the damage as visible as possible and comparable to the absorption image. It is most visible in the planes corresponding to the back-most layer of the plate (Figure 4(b)).

Projectional X-ray dark-field radiography. The X-ray dark-field radiographs were acquired with a lab-based Talbot-Lau grating interferometer operated at 50 kVp and 50 W tube power (X-RAY WorX SE 160, tungsten reflection target). The detector was an XRD 4343CT (Varex Imaging) with a pixel size of 150 μ m. The system is arranged in a symmetric geometry employing two absorption gratings and one phase grating, all with a period of 10 μ m and an inter-grating distance of 0.85 m, achieving a mean visibility of about 33%. Every dark-field frame was acquired by a phase stepping with 11 steps and an exposure time of 2 s each. Since the field-of-view in the sensitive configuration (sample 5 cm in front of the phase grating, 75 μ m effective pixel size) is limited to about 3 cm \times 2 cm, the sample was imaged in 12 exposures and stitched together after processing. The shown radiograph (Figure 4(c)) displays the negative natural logarithm of the relative visibility drop (V/V_0) close to the maximum dynamic range in the acquired data.

Micro-computed tomography (μ CT). The μ CT scans were performed using the same X-ray system and geometry as for the tomosynthesis. The acceleration voltage was increased to 50 kVp (200 μ A) for a better penetration at increased transmitted thicknesses. Two μ CT scans were performed with a 360 $^\circ$ rotation of the specimen. The first had the same geometry as the tomosynthesis and was conducted with 1,601 angular projections at an exposure time of 20 s each. The second was performed at 4 \times magnification (5-cm \times 5-cm field of view, 50- μ m effective pixel size) with 1,001 angular projections at 15 s exposure time. The volumetric images were reconstructed from the projections by the X-AID FDK Reconstruction Suite Version 2019.11.4 by Mitos GmbH. Selected slices from the 3D data are shown in Figure 4(d) and (e), where the greyscale values up to a constant factor represent the effective X-ray attenuation coefficient. For both measurements, the range of greyscale values was adapted similarly for a clear visualization of the damage.

Results of the comparison and discussion

In Figure 2, we collected the C-scans of each of the US methods described in the previous chapter. OLT and radiography results are shown separately in Figures 3 and 4, respectively. On the right side above each C-scan, its contrast-to-noise ratio (CNR) is labeled. It is defined as

$$\text{CNR} = \frac{S_F - S_D}{\sigma_N},$$

where S_F is the mean value of the C-scan amplitudes in the damage-free region, S_D the mean value of the C-scan amplitudes in the region of the impact damage, and σ_N standard deviation of the C-scan amplitudes in the damage-free region. Please note that for Figure 2(i) to (l) the noise levels in the damage-free region are overestimated, because the structures in the laminate (e.g. fiber bundles in different directions) are visible there. The lower CNR does not signify the lower quality of these C-scans, marked with the symbol (*).

In the previous chapter, a description is given for each US method, and how the amplitude scalar values were extracted from the A-scans for each scanning position. They are coded in greyscale to avoid subjectivity and are expressed in a relative range according to the minimum and maximum amplitude value of each scan (linear scale). It is possible to qualitatively compare the shape of the damaged area obtained by different methods and compare the signal-to-noise ratio of the scan image. We can examine which details of the impact damage are visible by a

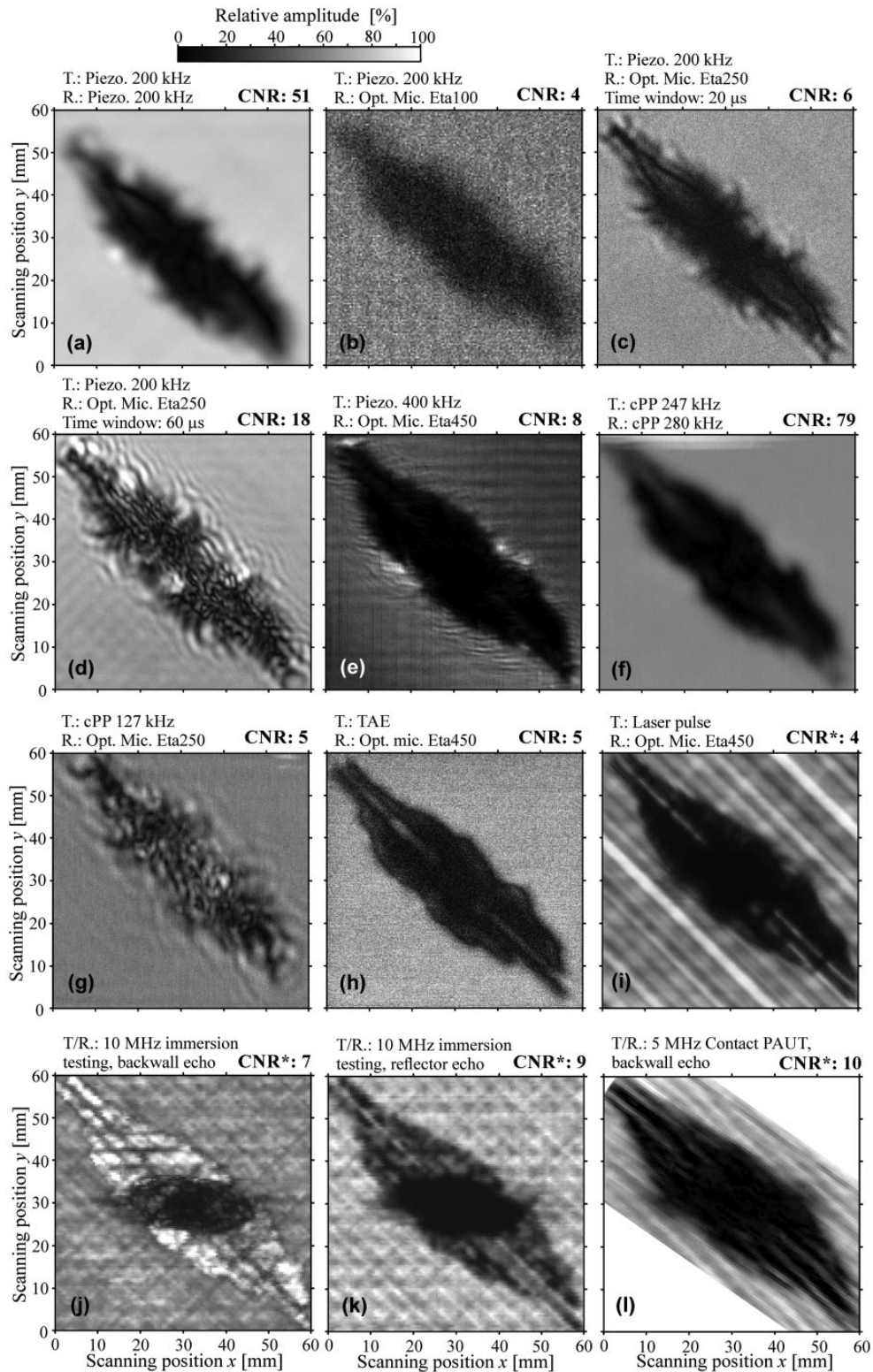


Figure 2. C-scans of the impact damage, obtained by various US methods: a piezoelectric transmitter in combination with a piezoelectric receiver (a) and various versions of optical microphones (b-e), a cPP transducer with a second cPP transducer (f) and an Eta250 optical microphone (g), a TAE with an Eta450 optical microphone (h), laser-induced US with an Eta450 optical microphone (i), immersion testing utilizing a backwall echo (j) and reflector echo (k), and contact PAUT (l). The corresponding transmitters (T) and receivers (R) are indicated on the left side above the scans and the contrast-to-noise ratios (CNR) on the right side above the scans. CNR marked with the symbol (*) are not reliable due to the exposed laminate structures.

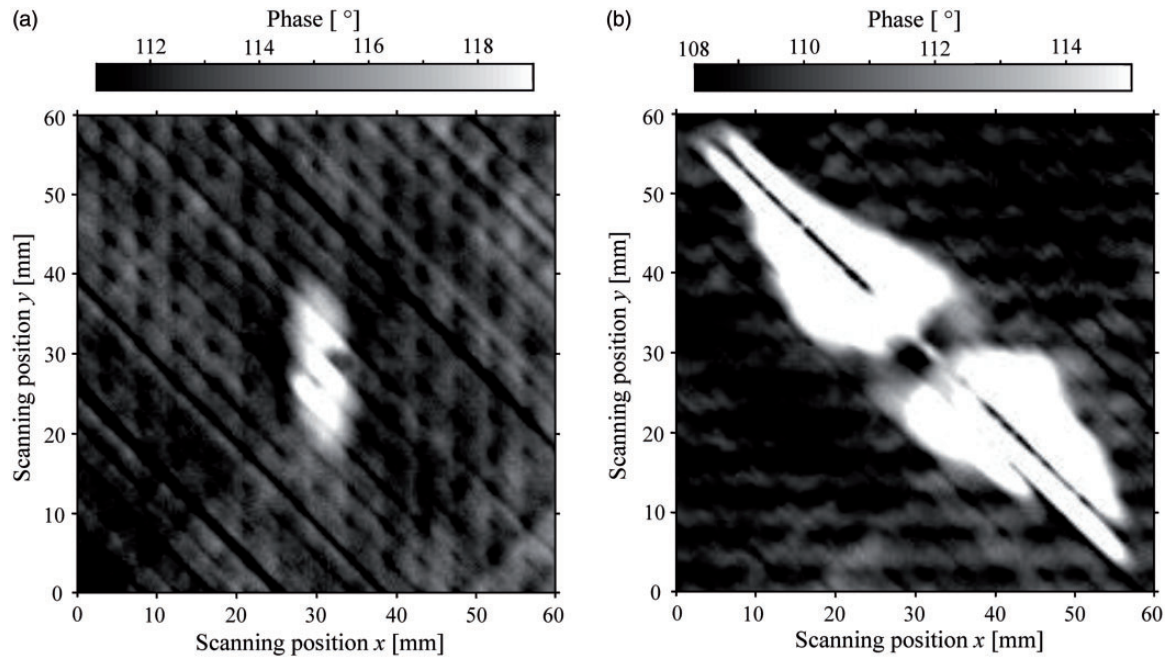


Figure 3. OLT phase images of the front (a) and back (b) side of the specimen.

single method. By observing the boundary of the defected area, we can observe the level of spatial averaging of the specific method caused by the transducer's aperture. The detected damage surface can also be compared.

ACU inspection with the piezoelectric transmitter and receiver yields good contrast (Figure 2(a)) between the damaged and damage-free area. The results are spatially blurred due to the 3-mm diameter of the transducers' soundfield in the focus. Detectability of the damage and resolution of the inspection process could be improved by using transducers of higher nominal frequency, which is however limited by attenuation level of US in the tested material.

The first model of the optical microphone (Eta100 prototype) had low sensitivity in this measurement configuration, which leads to a lower signal-to-noise ratio (Figure 2(b)). With each newer model of the optical microphone, the sensitivity was increased, which can be seen by the improvement in the quality of the scan image (Figure 2(b) to (e)). Spatial resolution is improved when the piezoelectric receiver is replaced by the optical microphone because of the small sensor's acoustic aperture. This is however negated by the image artifacts that blur the boundary and the interior of the damage (Figure 2(c), (d), and (g)). They are caused by mechanical interference, thickness resonances, and delamination clapping, while the US wave train travels through the chaotically cracked and delaminated area. These local defect resonances have

their characteristic frequencies typically in the range above several 10 kHz, but mostly below the plate thickness resonance frequency.^{29,31} These effects are more pronounced, when the US is detected over a wide frequency range e.g. by optical microphones. The effect of the measurement time gate width on these artifacts, in which the maximum amplitude is extracted to create a C-scan, can be observed by comparing Figure 2(c) with (d). These resonance artifacts are only present if the time window length is extended, which shows that the resonance effects occur after the first break of the US wave. No artifacts are present in Figure 2(h) when using the TAE and Eta450 optical microphone because the evaluated time gate width is reduced to the length of the US pulse (2 μ s). The increase of the US amplitude transmitted through the plate at the left-side and right-side of the damage boundary at scanning position $y=30$ can be explained similarly for Figure 2(e).

When applying a higher US frequency (400 kHz instead of 200 kHz), the shape of the damaged area is more pronounced and the artifacts at the damage boundary reduced (Figure 2(e)). This higher testing frequency allows for a more accurate determination of the damage surface, since higher US frequencies are dissipated more in the damaged area. Consequently, boundaries of the damage are clearer and the contrast between damaged and undamaged area is higher. A similar improvement could also be achieved by

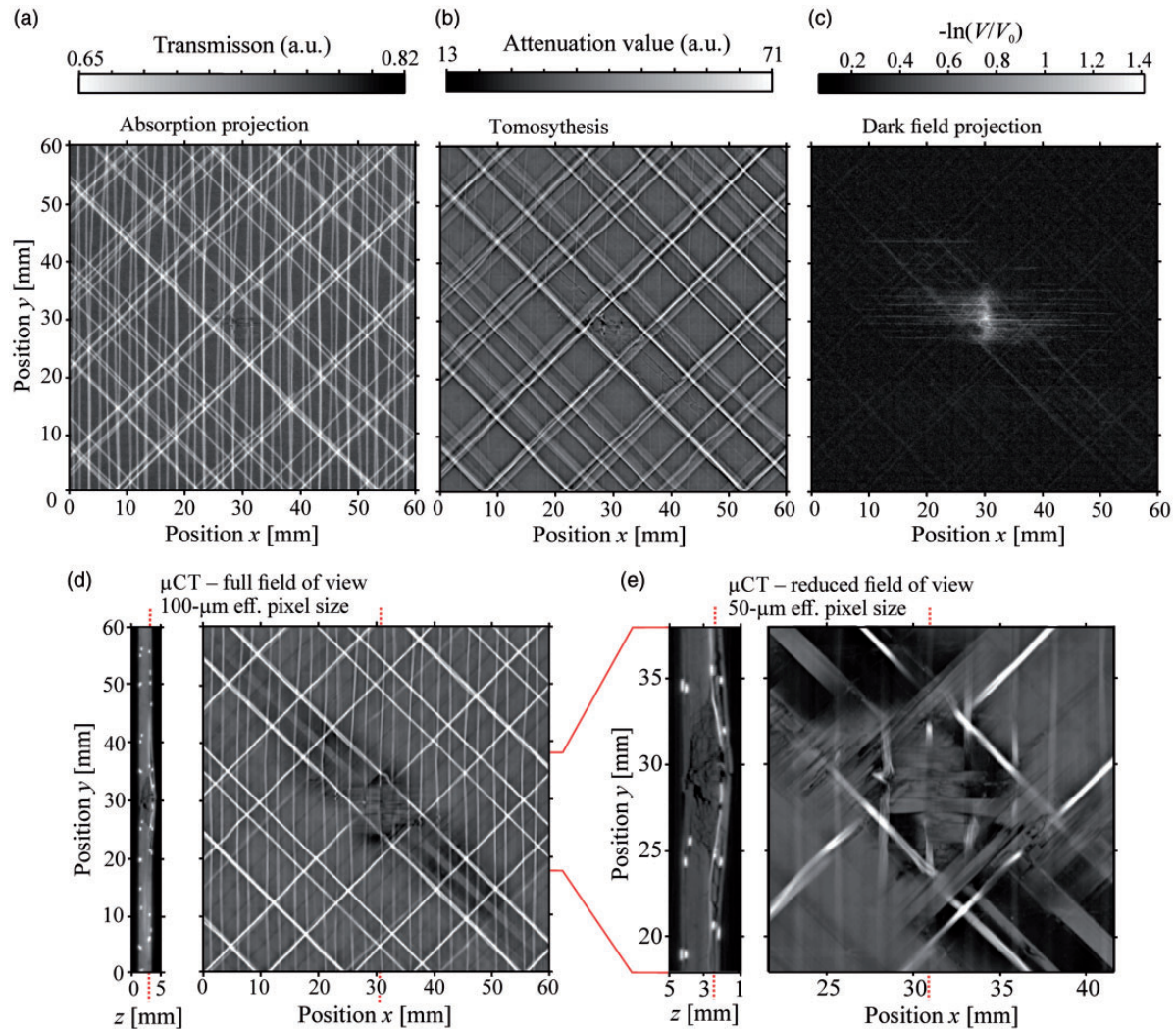


Figure 4. X-ray radiographs: absorption projection (a), tomosynthesis (b), dark-field projection (c), and selected μ CT slices of full field of view (d) and reduced field of view (e). Positions of cross-sectional images are marked with dotted lines in the background.

increasing the testing frequency of the conventional setup using a pair of piezoelectric transducers.

CPP transducers (Figure 2(f)) provide contrast improvement over conventional piezoelectric transducers (Figure 2(a)). Spatial blurring appears to be slightly reduced. Please note, that the testing frequency was lowered for the Figure 2(g), since the cPP transmitter had been used in the combination with an Eta250 optical microphone. Apart from this, the ACU inspection with piezoelectric transducers of increased frequency (400 kHz) was applicable, since a more sensitive Eta450 optical microphone was available for this measurement. We expect an improvement of cPP inspection results while using Eta450 instead of Eta250 optical microphone.

TAE generate short (μ s) US pulses matching the broadband frequency characteristics of the optical

microphone. This and the laser-excited US inspection are the only couplant-free methods described in this paper that allows MHz-range US inspection. The contour of the damage surface is well visible due to high-frequency US, which was focused on the small specimen surface. However, it is challenging to induce high-energy short-lasting US pulses. The signal-to-noise ratio is therefore lower in Figure 2(h). We want to emphasize that TAE is still in the development process and the full performance potential has not been tested yet (e.g. maximum pulse energy).

Laser US is able to generate short-lasting, high-energy US shock waves in higher frequency range (MHz) with repeatability suitable to be used for C-scan generation. Almost no US in the frequency range from 500 kHz to 4 MHz is transmitted through the plate in the delaminated area. This provides a good

contrast between damaged and damage-free plate area (Figure 2(i)). The damage area determined qualitatively by the laser US is comparable to the one determined by immersion testing (Figure 2(j) and (k)), which is often referred to as the most accurate method to evaluate the size of damage.

As it is the case for all the ACU methods in our experiment, no reliable conclusions about the interior of the damage (overlying delaminations, cracks and porosity) can be made.

Comparing all the ACU methods (including the laser US method) with the radiography methods (Figure 4), we can conclude that none of these deliver reliable information about the interior of the damaged area (also when the amplitude is expressed in logarithmic scale). At the first additional solid-to-air transition caused by an internal delamination or crack, almost all of the transmitted US is dissipated. Overlying delaminations, cracks and porosity cannot be reliably distinguish by ACU methods used in our experiments.

This is not the case for immersion testing (Figure 2(j) and (k)). Defect and material structure are clearly visible. The approximate true size of the defect can be easily determined by examining the C-scan obtained by the reflector echo (located behind the specimen plate), since the US in this case travels twice through the damaged area (Figure 2(k)). Since US are being reflected from the back side of the specimen, we can distinguish additional details about the damage, for example the area with a higher density of cracks lies directly under the impact location (Figure 2(j)). The adjacent brighter regions of the impact damage are caused by resonances due to the delamination of the last ply. This is the dominant damage pattern in this region, which can also be seen in the following μ CT evaluation.

PAUT inspection results are presented in Figure 2(l). The data are shown only within the trace, which was covered by the linear movement of the probe. The result shows a good contrast. The material structure is visible, however less clear than in the case of the more sensitive immersion inspection. The object shape differs from the one obtained by the immersion testing or by the laser US method. As with every contact inspection method, its applicability depends on the surface quality and its smoothness.

The orientation of several fiber layers can be determined by immersion testing method (Figure 2(j) and (k)). With the measurement setup, where US was excited by the laser pulse and detected by optical microphone Figure 2(i), we can distinguish the orientation of the surface fiber layer on the receiver side.

In Figure 3, results of the OLT applied to both sides of the plate are shown.

In the case of OLT, the inspection can be performed single-sided. However, it was found that the results

strongly depend on the side from which the inspection is performed. As shown in Figure 3(a) the inspection from the front side shows only a small fraction of the damaged area, while the inspection from the back side provides a result that corresponds well with the US inspection methods (Figure 3(b)). The delamination that is located near to the opposite surface of the plate is difficult to be detected by one-sided OLT, and the damage size is strongly underestimated. In non-defective areas of the sample, the induced heat wave is reflected on the back of the sample. In areas where only the last layer is delaminated, the reflection occurs only a few tenths of a millimeter earlier. These small differences are very challenging for OLT to detect.

In Figure 4, radiography results are shown: absorption projection (a), tomosynthesis (b), dark-field projection (c) and μ CT (d, e). The volumetric μ CT data of the full field of view (100- μ m effective pixel size) (Figure 4(d)) and reduced field of view (50- μ m effective pixel size) (Figure 4(e)) are shown in selected cross-sectional images. Their positions are marked with dotted lines in the background, respectively.

Absorption-based techniques (Figure 4(a), (b), (d), and (e)) deliver a significant contrast between the glass and the carbon fibers due to a strong difference in X-ray attenuation of silicon and carbon in the used energy range. The central part of the damage is only slightly visible in a single X-ray absorption projection. The lateral cracks are not distinguishable. The medial cracks are more pronounced in the tomosynthesis and defects between fiber bundles are recognizable. However, glass fibers below and above the examined layer are blurred, which is a typical feature of tomosynthesis. In the dark-field projection image, the central part of the damage delivers a high contrast compared to the remaining outer area and the glass fibers are almost invisible. As evident from the μ CT data, this bright area features a high density of microcracks. Therefore, projectional dark-field might be an efficient technique to detect such a kind of morphology without the need for high resolution and object rotation, as is the case with tomosynthesis and μ CT.

In Figure 4(d), the cross-sectional frame, on which the delaminated surface appears the largest (0.6 mm from the back surface) is shown. However, the damage boundaries are not well pronounced since the closed cracks do not deliver a significant contrast in X-ray attenuation and partial volume artifacts limit the sensitivity to very narrow delaminations. The surface of the damaged area obtained by μ CT is therefore smaller and less accurate than compared to the US inspection methods. In Figure 4(e), a detailed structure can be seen in the central region of the damaged area.

The high resolution scan reveals the voids between the displaced fiber bundles and the microscopic cracks.

Conclusion

The comparison of different methods is a basis for decision making regarding an inspection task with certain framework conditions. In the conclusion, we suggest optimal inspection methods for specific applications.

If the inspection process is to be automated and performed quickly, ACU is the most elegant solution for the specimens with suitable geometry (plates), especially if they are sensitive to liquid couplants. For larger impact damages and delaminations, where sub-millimeter resolution is not required, the transmission with cPP transducers or classical piezoelectric transducers delivers the highest contrast and is the most cost-effective. On the other hand, if the precise damage surface is of additional value or if the damage size is too small to be conventionally detected, we suggest using a 400 kHz piezoelectric transducer in combination with an Eta450 optical microphone.

Furthermore, if even higher sensitivity for damage detection and increased spatial resolution is required, we recommend laser-induced US or immersion testing. These two methods are capable to detect the delamination with the smallest opening of all of the methods described in this paper; μ CT at this point is limited by resolution and hardly detects any delaminations with openings below the voxel size. Laser-induced US is advantageous if the specimens cannot be immersed in water (e.g. big-sized, corrosive, fragile or hot specimens) or if the laser safety standards are easier to be realized for a specific application than the handling of the specimen in water. While it is possible with immersion testing to analyze the inner structure of the damage (worse than with μ CT), the laser-induced US is strongly dissipated over the entire area of the damage on the other hand. This shows that laser-induced US is a good indicator for the presence of the damage in the frequency range considered in this work.

PAUT is an elemental and accurate method and is a good alternative for thicker and larger parts that have a testing surface smooth enough to assure good coupling. It is especially advantageous for parts that require single-sided inspection. However, contact US inspection is more challenging to be automated.

OLT is a suitable solution for near-surface damage inspection of materials that are not thermally sensitive. Larger areas can be investigated integrally without an extensive scanning arrangement.

TAE offer a potential to increase the time resolution of a scan due to the short pulses that they are capable of emitting. Next to the laser-induced ultrasound, these

offer a possibility for single-sided ACU inspection and better depth resolution.

If the detailed three-dimensional structure of the defect is to be studied, μ CT still does not have a persuasive alternative. It is suitable for detection of density changes, inclusions, voids, open cracks and for the determination of the fiber orientation. However, a compromise between resolution and scanned range should be made while being subjected to the following limitations. First, the scanned volume in μ CT has to be rotated in the field of view of the imaging device, which makes large, but thin objects difficult to inspect. Furthermore, scan time is a limiting factor and makes high-volume quality control of even small parts quite challenging. The data handling as well as the reconstruction and automated evaluation requires specialized hardware and software solutions and increases the efforts immensely. Therefore, μ CT is most effective in research and development or process control, where a detailed understanding of the material structure and properties is required. However, μ CT data might help for model building, simulation and validation of results and for conclusions drawn from other methods. μ CT can be of high value, especially when microscopic properties have to be correlated to macroscopic material performance or physical interactions at the micron-scale are studied, which are exploited in other inspection methods.

For flat, large objects, X-ray CT variants such as tomosynthesis/laminography can be considered if only the meridian cracks are to be detected. Thus, the scan time can be significantly reduced compared to μ CT.

The porosity and presence of microcracks can be detected specifically by X-ray dark-field radiography without object rotation, much lower system resolution and higher speed. It might have advantages over US when impact damages in more complex sample geometries have to be inspected. Additionally, dark-field projections from different orientations can deliver additional information about the orientation of the microcracks and the fiber structure.¹²

In contrast to μ CT, US inspection methods are able to directly detect the mechanical properties of the damaged area, since they significantly affect the mechanical wave propagation (US damping, reflection, scattering, etc.). It is therefore possible to selectively detect features that are crucial for the specimens' macroscopic mechanical properties (delaminations, closed and open cracks, etc.).

For further improvement of the inspection process, there is a potential advantage in combining different test methods. For example, the μ CT data can be fused with US inspection data. Additional information

could consequently be obtained, which is not achievable if both methods are considered separately.

For example, exact in-depth location and size of the closed cracks can only be obtained by comparing Figure 4(d) with Figure 2(i), (j) or (k). μ CT data suggest that the detached layers at 0.6-mm depth from the back side of the plate extends over the entire damage surface, the value of which can more precisely be determined by US inspection. Complementary use of these two methods is advantageous for plate inspection, since medial cracks can be better detected by X-ray radiography and lateral cracks by US methods. Furthermore, the approximate location of the damaged area can be more efficiently determined by US for larger testing objects. The detailed structure of the damage can be subsequently analyzed by the focused application of more rigorous X-ray radiography methods.

Declaration of Conflicting Interests

The author(s) declared no potential conflicts of interest with respect to the research, authorship, and/or publication of this article.

Funding

The author(s) disclosed receipt of the following financial support for the research, authorship, and/or publication of this article: The authors acknowledge the German Federal Ministry of Education and Research for financial support.

ORCID iD

Janez Rus  <https://orcid.org/0000-0002-2287-1531>

References

- Grosse CU, Goldammer M, Grager JC, et al. Comparison of NDT techniques to evaluate CFRC – results obtained in a MAIzfp round robin test. In: *Tagungsband WCNDT*, Munich, Germany, 2016.
- Ehrlich I, Dinnebieer H and Jost C. Comparison of impact delaminations in CFRP using different test methods. *J Achieve Mater Manuf Eng* 2015; 73: 128–138.
- Maierhofer C, Krankenhagen R, Röllig M, et al. Quantification of impact damages in CFRP and GFRP structures with thermography and ultrasonics. *Proc QIRT* 2018; 933–940.
- Abou-Khousa MA, Ryley A, Kharkovsky S, et al. Comparison of X-ray, millimeter wave, shearography and through-transmission ultrasonic methods for inspection of honeycomb composites. *AIP Conf Proc* 2007; 894: 999–1006.
- Wang J, Zhang J, Chang T, et al. A comparative study of non-destructive evaluation of glass fiber reinforced polymer composites using terahertz, X-ray, and ultrasound imaging. *Int J Precis Eng Manuf* 2019; 20: 963–972.
- Schumacher D, Meyendorf N, Hakim I, et al. Defect recognition in CFRP components using various NDT methods within a smart manufacturing process. *AIP Conf Proc* 2018; 1949: 020024.
- Hakim I, May D, Abo Ras M, et al. Quantifying voids effecting delamination in carbon/epoxy composites: static and fatigue fracture behavior. *Proc SPIE 9806, Smart Materials and Nondestructive Evaluation for Energy Systems* 2016; 98060H. DOI: 10.1117/12.2222032.
- Papa I, Ricciardi MR, Antonucci V, et al. Comparison between different non-destructive techniques methods to detect and characterize impact damage on composite laminates. *J Compos Mater* 2020; 54: 617–631.
- Grager JC, Kotschate D, Gamper J, et al. Advances in air-coupled ultrasonic testing combining an optical microphone with novel transmitter concepts. In: *12th ECNDT*, Gothenburg, Sweden, 2018.
- Pfeiffer F, Bech M, Bunk O, et al. Hard-X-ray dark-field imaging using a grating interferometer. *Nat Mater* 2008; 7: 134–137.
- Senck S, Scheerer M, Revol V, et al. Microcrack characterization in loaded CFRP laminates using quantitative two- and three-dimensional X-ray dark-field imaging. *Compos A Appl Sci Manuf* 2018; 115: 206–214.
- Prade F, Schaff F, Senck S, et al. Nondestructive characterization of fiber orientation in short fiber reinforced polymer composites with X-ray vector radiography. *NDT & E Int* 2017; 86: 65–72.
- Kageyama M, Okajima K, Maesawa M, et al. X-ray phase-imaging scanner with tiled bent gratings for large-field-of-view nondestructive testing. *NDT & E Int* 2019; 105: 19–24.
- Meyendorf N, Nagy PB and Rokhlin S. *Nondestructive materials characterization with applications to aerospace materials*. Berlin, Heidelberg: Springer-Verlag, 2004, p.67.
- Ida N and Meyendorf N. *Handbook of advanced nondestructive evaluation*. Cham: Springer, 2019.
- Grager JC. *Quantitative impact- und Porositätscharakterisierung an CFK-Werkstoffen mittels zerstörungsfreier Prüfmethoden*. Master's Thesis, Chair of Non-Destructive Testing, Technical University of Munich, Germany, 2014.
- Rus J, Kulla D, Grager JC, et al. Air-coupled ultrasonic inspection of fiber-reinforced plates using an optical microphone. In: *DAGA Deutsche Jahrestagung für Akustik (2019)*, Rostock, Germany, 2019, pp.763–766. Deutsche Gesellschaft für Akustik.
- López Baos A. Laser-based air-coupled ultrasonic testing of CFRP plates. Master's thesis, Chair of Non-Destructive Testing, Technical University of Munich, Germany, 2018.
- Guruschkin E. *Berührungslose Prüfung von Faserverbundwerkstoffen mit Luftultraschall*. Master's Thesis, Chair of Non-Destructive Testing, Technical University of Munich, Germany, 2015.
- Gamper J. *Entwicklung eines neuen Messkonzepts zur luftgekoppelten Ultraschallprüfung von Faserverbundwerkstoffen*. Master's Thesis, Chair of Non-Destructive Testing, Technical University of Munich, Germany, 2017.

21. Fischer B. Optical microphone hears ultrasound. *Nature Photon* 2016; 10: 356–358.
22. Preisser S, Rohringer W, Liu M, et al. All-optical highly sensitive akinetic sensor for ultrasound detection and photoacoustic imaging. *Biomed Opt Express* 2016; 7: 4171–4186.
23. Gaal M, Caldeira R, Bartusch J, et al. Air-coupled ultrasonic ferroelectret receiver with additional bias voltage. *IEEE Trans Ultrason Ferroelectr Freq Control* 2019; 66: 1600–1605.
24. Vössing KJ, Gaal M and Niederleithinger E. Air-coupled ferroelectret ultrasonic transducers for nondestructive testing of wood-based materials. *Wood Sci Technol* 2018; 52: 1527–1538.
25. Gaal M, Bartusch J, Dohse E, et al. Focusing of ferroelectret air-coupled ultrasound transducers. *AIP Conf Proc* 2016; 1706: 080001.
26. Lange PD and John WS. On thermophones. *Proc R Soc A: Math Phys Eng Sci* 1915; 91: 239–241.
27. Daschewski M, Boehm R, Prager J, et al. Physics of thermo-acoustic sound generation. *J Appl Phys* 2013; 114: 114903.
28. Rus J, Fischer B and Grosse CU. Photoacoustic inspection of CFRP using an optical microphone. *Proc SPIE, Optical Measurement Systems for Industrial Inspection XI* 2019: 1105622. DOI: 10.1117/12.2525021.
29. Rus J and Grosse CU. Local ultrasonic resonance spectroscopy: a demonstration on plate inspection. *J Nondestruct Eval* 2020; 39: 31.
30. Setz R. *Experimentelle Impakt-, Ondulations- und Porositätscharakterisierung an CFK-Probekörpern mittels zerstörungsfreier Prüfmethoden*. Master's Thesis, Chair of Non-Destructive Testing, Technical University of Munich, Germany, 2015.
31. Hettler J, Tabatabaiepour M, Delrue S, et al. Detection and characterization of local defect resonances arising from delaminations and flat bottom holes. *J Nondestruct Eval* 2017; 36: 2.

Article #3: Thickness Measurement via Local Ultrasonic Resonance Spectroscopy

Authors: Janez Rus, Christian U. Grosse

Title: Thickness Measurement via Local Ultrasonic Resonance Spectroscopy

Journal: Ultrasonics

Publisher: Elsevier

Received by the publisher: 19 February 2020

Received by the publisher in the revised form: 29 August 2020

Accepted: 18 September 2020

Available online: 23 September 2020

Issue month: January 2021

Volume: 109

Reference number: 106261

DOI: 10.1016/j.ultras.2020.106261

Reprint Permissions

The publisher Elsevier B.V. has the exclusive right to publish and reproduce Article #3, which thus cannot be included in Appendix. It can be accessed using the bibliography data listed above.